THE FLORIDA STATE UNIVERSITY

COLLEGE OF ARTS AND SCIENCES

A PRECISION MEASUREMENT OF THE W $\rightarrow \mu\nu$ CHARGE ASYMMETRY AT A CENTER OF MASS ENERGY OF 1.96 TEV USING THE DØ DETECTOR

By

SINJINI SENGUPTA

A Dissertation submitted to the
Department of Physics
in partial fulfillment of the
requirements for the degree of
Doctor of Philosophy

Degree Awarded:
Summer Semester, 2006

The members of the Committee approve the Dissertation of Sinjini Sengupta defended on May 23, 2006.

Susan K. Blessing
Professor Directing Dissertation

William Landing
Outside Committee Member

Horst Wahl
Committee Member

Harrison Prosper
Committee Member

Joseph Owens III
Committee Member

Simon Capstick
Committee Member

The Office of Graduate Studies has verified and approved the above named committee members.

ACKNOWLEDGEMENTS

There are several people who have influenced this thesis. Some of them were directly involved with the analysis and others were a part of my life. I'd like to take a moment to acknowledge them.

Thanks are due to the members of the DØ collaboration for tirelessly collecting all the data without which no analysis is possible. I have to thank my advisor Susan Blessing for helping me to get this analysis in good shape, for all the discussions that made me think things through and for the numerous times she patiently edited my writeups. I'd like to thank my HEP professors at FSU for always taking the time to discuss any aspect of the analysis with me. I'd particularly like to thank Harrison Prosper for discussions about statistical uncertainties and Horst Wahl for all the discussions about the detector. I have enjoyed all of our discussions and debates and always learned a lot from it. Todd Adams, Yuri Gerstein and Vasken and Sharon Hagopian were also always available when I needed help. Thanks are also due to Professor Jeff Owens for all his help with the theoretical aspects pertaining to this analysis.

I'd like to thank Boris Tuchming, Gavin Hasketh and Jon Hays for contributing to this analysis by providing invaluable input and my electroweak convenor Dmitri Denisov for helping me get the analysis through. I'd like to thank Paul Telford and Frederic Deliot for providing the Monte Carlo samples for this analysis and Kyle Stevenson for helping me get started on it at the very begining. I'd also like to thank the members of my editorial board for scrutinizing all the technical aspects of this analysis and the members of my committe for taking the time to read it and for their suggestions to make it better.

I'd like to thank the members of the STT group for many experiences (some good and some distinctly unpleasant) but primarily for the opportunity to work with the DØ detector and in the end for getting it all working.

I'd also like to thank the rest of the FSU HEP people. Kathy, for the countless forms she

took care of for me. Brian, for helping me find a bike my first summer at the lab. Bill, for helping us all get started while being being patient with us. Craig, Jose, Yuri and Atilla, who all gave me rides when I didnt have a car. Daekwang, for always lending me his ear when I needed to rant and for the n number of times he took me to and from the airport. Haryo, for being our living source of reference though he frequently annoyed us all with his singing. Andrew, for always having time to discuss small technical details as well as the larger physics issues. Norm, for inspiring with his work ethic and Dan, for his sunny disposition.

I'd like to thank the late Kay Caudill for welcoming me to the physics department with a hug and making me feel less lonely that first day. I'd like to thank Pramod and Mukundan who helped me even before I arrived there. My first year buddies Jorge, Daniel, Eddy, Dave and Mohammad who have all helped me in one way or another. Shifeng, for all the delicious Chinese food. Jelena, for her friendship and hospitality and Anuvrat, also for his friendship.

There are many people I've met and associated with at Fermilab. Some of them deserve special mention. Manasda who introduced me to the Indian community here and Nirmalyada and Amitabha for tea and lots of information. Ammina, Burair and Cigdem with whom I have spent good times together. The many friends I've made including Meta, Ulla, Tulika, Supriya, Jyothsna and Alison who have shared conversations and meals with me. Kristian and Katrin for their company and for always making me welcome. And also Greg, Satish and Robert for all the laughs at lunch.

I would also like to mention my childhood friend Richa Bhatnagar, who still remains someone that I can talk to about anything. I would also like to mention my 'little' sister Tushi, who has always believed in me, looked up to me and given me her love.

I have to thank my mother and my father for allowing me to go far, far away to pursue a dream even though it has been difficult for them. Without them, this work would not have come to fruition. I'd like to thank them for everything that they have done for me and I thank them for their endless love, caring and support.

Lastly, I'd like to thank Rainer Fries for all his love and and for all the wonderful moments that we have shared. I'd like to thank him for always being there for me, encouraging me, putting up with me even when I have been difficult and for helping me to believe in myself.

TABLE OF CONTENTS

List of Tables vii

List of Figures viii

Abstract xiv

1. Introduction 1

2. Theory 3
2.1 The Standard Model 3
2.2 Parton Distribution Functions 6
2.3 Electroweak Interactions 11
2.4 **W** Boson Production and Decay 13
2.5 The **W** Boson Charge Asymmetry 17
2.6 Why measure the **W** Charge Asymmetry? 20

3. The Experimental Apparatus 23
3.1 The Tevatron 23
3.2 The DØ Detector 25
3.3 The DØ coordinate system 26
3.4 The Central Tracker 27
3.5 Calorimeter 34
3.6 The Intercryostat Detector 37
3.7 The Muon Detector 37
3.8 Triggers 41

4. Event Reconstruction 48
4.1 Central Tracks 48
4.2 Muons 52
4.3 Calorimeter Clusters 57
4.4 Jet Energy Scale Corrections 60

5. Event Selection 62
5.1 Pre-Selection 62
5.2 Triggers 63
5.3 Event Selection 63

6. Checking for Biases in Data 67
6.1 Charge Misidentification 67
6.2 Efficiencies 77
6.3 Other Biases 93

7. Backgrounds 96
7.1 Monte Carlo Simulation using PMCS 96
7.2 Background Estimate 100
7.3 Combining of triggers 106

8. Results and Conclusions 118

A. Efficiency Error Calculation 125

REFERENCES 131

BIOGRAPHICAL SKETCH 135

LIST OF TABLES

2.1 The fundamental particles of the standard model known as fermions which consist of three generations of leptons and quarks. Next to each fermion is its mass M (in GeV) and electric charge q (in multiples of elementary charge e). Fermions have spin-$\frac{1}{2}$ [6]. 4

2.2 The gauge bosons of the standard model. These are the carriers of the four fundamental forces. Gravitons have not yet been found. The Higgs boson is the only scalar particle and does not fit into the usual scheme [6]. 5

3.1 Parameters of the Muon Drift Tubes. 39

7.1 Summary of parameters used to smear p_T. 97

7.2 Summary of parameters used to smear $\not\!\!E_T$. 98

7.3 Summary of the QCD background estimation where f_{QCD} gives the fraction of QCD contamination in the $W \rightarrow \mu\nu$ data sample. 105

7.4 Summary of all estimated backgrounds in the W sample 106

8.1 Total uncertainties on the folded asymmetry in bins of rapidity. 119

8.2 Data and background for negative muons in bins of rapidity. The errors on each background in each bin are statistical in nature. 121

8.3 Data and background for positive muons in bins of rapidity. The errors on each background in each bin are statistical in nature. 122

8.4 Statistical and systematic uncertainties on the asymmetry in bins of rapidity. 123

8.5 Breakdown of the systematic uncertainties by bins of rapidity. 124

LIST OF FIGURES

2.1 The range in x and Q^2 probed by various DIS experiments. ZEUS and HERMES were particle detectors at the electron-proton collider HERA at the DESY laboratory in Hamburg, Germany. E665 was a muon-proton collider experiment and CCFR was a fixed target experiment at Fermilab. BCDMS and NMC were muon scattering experiments at CERN, Switzerland. SLAC is the linear accelerator at Stanford, California. 9

2.2 Overview of the CTEQ6M PDFs at $Q = 2$ GeV(left plot) and at $Q = 100$ GeV (right plot). $xf(x)$ is the probability density of the momentum fraction x. 10

2.3 The leading order theoretical prediction for the $W^{\pm}$ production cross sections as a function of rapidity y, at the Tevatron. 15

2.4 The process of $u\bar{d} \rightarrow \mu^{+}\nu_{\mu}$ in the W boson rest frame. The arrows on the lines represent the momenta of the particles while the double arrows indicate their helicity. 16

2.5 The leading order theoretical prediction for the cross sections of $l^{\pm}$ from the $W^{\pm}$ decay, as a function of rapidity at the Tevatron. 17

2.6 The dominant process for W^{-} production at the Tevatron 18

2.7 Comparison of the W production charge asymmetry (in blue)and the decay lepton charge asymmetry (in red) over all momenta. 19

2.8 The Run I W charge asymmetry results from CDF [26]. 21

2.9 The Run II W charge asymmetry results in the electron channel from CDF [27]. 22

3.1 The Fermilab Tevatron accelerator. 24

3.2 The RunII DØ detector. 26

3.3 A cross section of the DØ Run II central tracking system. 28

3.4 The Silicon Microstrip Tracker. 29

3.5 Cross section of an SMT barrel in the $x - y$ plane. 30

3.6 A typical SMT ladder. 31

3.7 Cross Section of the CFT detector. 32

3.8 The central and forward pre-shower detectors. 34

3.9 The DØ calorimeter. 35

3.10 A schematic view showing the transverse and longitudinal segmentation pattern of a section of the DØ calorimeter. The lines and numbers indicate pseudorapidity intervals from the center of the detector. 36

3.11 A cut away three dimensional view of the muon detector. 38

3.12 An exploded view of the muon wire chambers. 40

3.13 An exploded view of the muon scintillation counters. 41

3.14 Level 1 and 2 Trigger Architecture. The information flow is indicated by the horizontal arrows. 42

3.15 A schematic diagram of an STT crate. 46

4.1 Tracking hypothesis based on fitting 3 hits to start a track. The points in blue represent hits in the detector layers. 50

4.2 Segment reconstruction in the drift plane. 53

5.1 The resultant distributions of W transverse mass, the p_T of the muon and the $\not\!\!E_T$ after all selection cuts have been applied to data. 65

6.1 The dimuon invariant mass. 68

6.2 The upper plot shows the charge misidentification distribution as a function of η when the events are selected without any track quality requirements whatsoever. The lower plot shows the p_T distribution of the like-sign muon in this sample. 69

6.3 The upper plot shows the charge misidentification distribution as a function of η when the events are selected without any track quality requirements whatsoever. The lower plot shows the p_T distribution of the like-sign muon in this sample. 70

6.4 The charge misidentification distribution as a function of η when isolation requirements as well as SMT and CFT hits requirement are applied. 71

6.5 The charge misidentification distribution as a function of η when isolation requirements, SMT and CFT hits requirement as well as dca requirements are applied. 71

6.6 The charge misidentification distribution as a function of η when isolation requirements, SMT and CFT hits requirement as well as χ^2 (but no dca) requirements are applied. 72

6.7 p_T distribution of muons in W events in blue solid and in Z events in red dashed (the p_T distribution of Z events was scaled to the number of events in the W sample). 72

6.8 η distribution of same sign tracks in grey and the η distribution of all tracks in white for the dimuon sample. 74

6.9 The dimuon invariant mass in a sample of events which fires one of the dimuon triggers. 74

6.10 The charge misidentification distribution in Monte Carlo as a function of η. . 75

6.11 p_T significance of all muon tracks in the W sample 76

6.12 Curvature significance of all muon tracks in the sample. 77

6.13 Tag and probe method for L2 trigger and offline muon reconstruction efficiencies 78

6.14 The offline medium muon reconstruction efficiency as a function of a) p_T and b) charge. 79

6.15 The upper plot shows the offline medium muon reconstruction efficiency as a function of η with the positive and negative charges are separated. The lower plot shows the ratio of positive and negative efficiencies as a function of η. . 81

6.16 The L2 muon efficiency as a function of p_T (top) and charge (bottom). . . . 82

6.17 The L2 muon trigger efficiencies as a function of η, when separated into positive and negative charged muons in the top plot and the ratio of these efficiencies in η at the bottom. 83

6.18 Tag and probe method for L3 trigger and track reconstruction efficiencies . . 84

6.19 The upper plot shows the tracking efficiency as a function of p_T while the lower plot shows the tracking efficiency as a function of charge. 85

6.20 The upper plot shows the tracking efficiency as a function of η with the positive and negative charges separated out while the lower plot shows the ratio of these efficiencies as a function of η. 86

6.21 The upper plot shows the L3 track efficiency as a function of p_T and the lower plot shows the L3 track efficiency as a function of charge. 87

6.22 The upper plot shows the L3 track efficiency as a function of η with the positive and negative muons separated out while the lower plot shows the ratio of positive and negative efficiencies for L3 track trigger efficiencies as a function of η. 88

6.23 Combined efficiency distributions by charge as a function of η on the top and the plot of the ratio of these efficiencies as a function of η fitted to a straight line at the bottom. 90

6.24 The isolation efficiency plotted as a function of a) p_T, b) charge and c) as a function of η with the positive and negative charges separated out. 92

6.25 This shows the asymmetry distribution when the solenoid polarity is forward (blue circles) and when the solenoid polarity is reversed (orange triangles), independent of the toroid polarity. 94

6.26 This shows the asymmetry distribution when the toroid polarity is forward (blue circles) and when the toroid polarity is reversed (orange triangles), independent of the solenoid polarity. 94

6.27 This plot shows the CP folded asymmetry. The square black data points represent $A(y)$ while the red open-circle data points represent $-A(-y)$. . . . 95

7.1 χ^2 versus value of mip in data-PMCS comparison of $W \to \mu\nu$ data. 99

7.2 Probability for a single muon to pass the isolation cut as a function of p_T when $\not\!\!E_T > 20$ GeV ($M_T > 40$ GeV) and also when $\not\!\!E_T < 20$, 15 and 10 GeV (without any M_T cut). 103

7.3 Probability for a single muon to pass the isolation cut as a function of p_T when $\not\!\!E_T < 10$ GeV. 104

7.4 Probability for a single muon to pass the isolation cut as a function of rapidity when $\not\!\!E_T < 10$ GeV and $p_T > 20$ GeV with the charges separated out. 105

7.5 The W transverse mass (data and Monte Carlo) in linear scale (upper plot) and in log scale (lower plot) for the "wide" trigger. The $W \to \mu\nu$ MC line is the sum of $W \to \mu\nu$, $W \to \tau\nu$, $Z \to \mu\mu$, $Z \to \tau\tau$ and QCD. 108

7.6 The W transverse mass (data and Monte Carlo) in linear scale (upper plot) and in log scale (lower plot) for the "all" trigger. The $W \to \mu\nu$ MC line is the sum of $W \to \mu\nu$, $W \to \tau\nu$, $Z \to \mu\mu$, $Z \to \tau\tau$ and QCD. 109

7.7 The muon p_T distribution (data and Monte Carlo) in linear scale (upper plot) and in log scale (lower plot) for the "wide" trigger. The $W \to \mu\nu$ MC line is the sum of $W \to \mu\nu$, $W \to \tau\nu$, $Z \to \mu\mu$, $Z \to \tau\tau$ and QCD. 110

7.8 The muon p_T distribution (data and Monte Carlo) in linear scale (upper plot) and in log scale (lower plot) for the "all" trigger. The $W \to \mu\nu$ MC line is the sum of $W \to \mu\nu$, $W \to \tau\nu$, $Z \to \mu\mu$, $Z \to \tau\tau$ and QCD. 111

7.9 The $\not\!\!E_T$ distribution (data and Monte Carlo) in linear scale (upper plot) and in log scale (lower plot) for the "wide" trigger. The $W \to \mu\nu$ MC line is the sum of $W \to \mu\nu$, $W \to \tau\nu$, $Z \to \mu\mu$, $Z \to \tau\tau$ and QCD. 112

7.10 The $\not\!\!E_T$ distribution (data and Monte Carlo) in linear scale (upper plot) and in log scale (lower plot) for the "all" trigger. The $W \to \mu\nu$ MC line is the sum of $W \to \mu\nu$, $W \to \tau\nu$, $Z \to \mu\mu$, $Z \to \tau\tau$ and QCD. 113

7.11 The η distribution for negative muons (data and Monte Carlo) in linear scale (upper plot) and in log scale (lower plot) for the "wide" trigger. The $W \to \mu\nu$ MC line is the sum of $W \to \mu\nu$, $W \to \tau\nu$, $Z \to \mu\mu$, $Z \to \tau\tau$ and QCD. Even though the full η distribution for the "wide" trigger is shown, only the events for $|\eta| < 1.4$ are used to evaluate the asymmetry. The error bands shown on the $W \to \mu\nu$ line are the PMCS uncertainties due to the statistics for the Z sample. 114

7.12 The η distribution for negative muons (data and Monte Carlo) in linear scale (upper plot) and in log scale (lower plot) for the "all" trigger. The $W \to \mu\nu$ MC line is the sum of $W \to \mu\nu$, $W \to \tau\nu$, $Z \to \mu\mu$, $Z \to \tau\tau$ and QCD. Even though the full η distribution for the "all" trigger is shown, only the events for $|\eta| > 1.4$ are used to evaluate the asymmetry. The error bands shown on the total expected plot are the PMCS uncertainties due to the statistics for the Z sample. 115

7.13 The η distribution for positive muons (data and Monte Carlo) in linear scale (upper plot) and in log scale (lower plot) for the "wide" trigger. The $W \to \mu\nu$ MC line is the sum of $W \to \mu\nu$, $W \to \tau\nu$, $Z \to \mu\mu$, $Z \to \tau\tau$ and QCD. Even though the full η distribution for the "wide" trigger is shown, only the events for $|\eta| < 1.4$ are used to evaluate the asymmetry. The error bands shown on the total expected plot are the PMCS uncertainties due to the statistics for the Z sample. 116

7.14 The η distribution for positive muons (data and Monte Carlo) in linear scale (upper plot) and in log scale (lower plot) for the "all" trigger. The $W \to \mu\nu$ MC line is the sum of $W \to \mu\nu$, $W \to \tau\nu$, $Z \to \mu\mu$, $Z \to \tau\tau$ and QCD. Even though the full η distribution for the "all" trigger is shown, only the events for $|\eta| > 1.4$ are used to evaluate the asymmetry. The error bands shown on the total expected plot are the PMCS uncertainties due to the statistics for the Z sample. 117

8.1 The top plot shows the corrected muon charge asymmetry distribution with the statistical errors in black and the systematic errors in blue. The yellow band is the envelope determined using the 40 CTEQ PDF error sets; the red line is the central value. The lower plot shows the corrected folded asymmetry with combined statistical and systematic uncertainties. The yellow band is the envelope determined using the 40 CTEQ PDF error sets while the blue curve is the charge asymmetry using the MRST02 PDFs. 120

ABSTRACT

This dissertation describes a measurement of the muon charge asymmetry from W boson decays. The charge asymmetry provides useful information about the momentum distribution of u and d quarks inside the proton. The charge asymmetry was measured using ≈ 230 pb^{-1} of data collected between 2002 and 2004 using the DØ detector at the Tevatron collider at Fermi National Accelerator Laboratory. In the Tevatron, protons and antiprotons collide with a center of mass energy of 1.96 TeV. The signal consists of one high transverse momentum muon and missing transverse energy while the background which comes from other events also producing a high transverse momentum muon. As the charge asymmetry depends on the number of positive and negative muons from the W boson decay in each bin of pseudorapidity, the background are removed. The resultant distribution is compared with predictions from NLO calculations using the CTEQ6.1M and the MRST02 PDFs. This is the first approved result for the W charge asymmetry from DØ.

CHAPTER 1

Introduction

Particle physics is all about trying to understand the universe that we live in: what the fundamental constituents of matter are and how they interact with each other. The knowledge that atoms and molecules are the building blocks of matter has been with us for a very long time but the first concrete indication that atoms might be made up of more fundamental particles came with Thomson's discovery of the electron close to the end of the 19^{th} century. Atoms were then believed to be uniform spheres of positively charged matter in which electrons were embedded. Rutherford's scattering experiment in 1911 found that the atoms actually had a heavy, positively charged, small, hard center which was called the nucleus. Protons and neutrons, as constituents of atomic nuclei, were subsequently discovered in the first half of the 20^{th} century.

Neutrinos were postulated by Pauli in 1930 to explain the energy spectrum of electrons and the apparent lack of conservation of energy and angular momentum in beta decays. Since neutrinos are extremely difficult to detect, they were not observed until 1956. Muons were discovered in 1936 as constituents of cosmic rays. Since 1947, a whole slew of particles has been discovered, including pions and kaons, which are collectively called hadrons, as are protons and neutrons.

In 1961, Gell-Mann and Nishijima proposed the "eightfold way", a classification scheme of hadrons. This was later explained in terms of quarks. Quarks as the building blocks of hadrons, was also proposed independently by Zweig in 1964. What is today considered the first direct evidence for quarks, came from deep-inelastic scattering experiments at SLAC in 1969. Quantum chromodynamics (QCD) was put forth as the theory of the strong interaction between quarks by Gross, Wilzcek and Politzer in 1973 while Glashow, Salam and Weinberg developed the theory of the electroweak force in the late 1960s. These two theories make

up what is now called the standard model. The missing fundamental particles predicted by the standard model have been experimentally observed one by one. The charm quark was discovered through the observation of the J/ψ meson at Brookhaven and at SLAC in 1974, the tau lepton was discovered at SLAC in 1976, the bottom quark was observed at Fermilab in 1977 and the top quark was first seen in 1995, also at Fermilab. The W and Z bosons were first observed at CERN in 1983.

The latest results from cosmology indicate that all the known matter makes up only about 5% of the Universe. Almost 25% is made up of matter that has not yet been identified and is called dark matter. The bulk of the mass-energy of the Universe (about 70%) appears to be made of something even more mysterious and is termed dark energy. There are many theories that go beyond the standard model which attempt to explain these observations and predict the constituents of dark matter and dark energy. However, the standard model continues to provide the best description of the material world that surrounds us.

This dissertation describes a precision measurement directly pertaining to the standard model: attempting to improve our understanding of the momentum distribution of quarks inside protons by studying the charge asymmetry of muons from W boson decays. These momentum distributions are known as parton distribution functions (PDFs). Precise knowledge of PDFs is an important input in the search for new physics and crucial to all calculations pertaining to hadronic interactions. Chapter 2 begins with a description of the standard model, then PDFs and their experimental relevance are introduced. This is followed by a discussion of electroweak interactions, production and decay of W bosons, and the charge asymmetry and its importance. The experimental apparatus, the Tevatron accelerator and the DØ detector, are described in Chapter 3. In Chapter 4, the process of reconstructing individual particles, and hence the event itself, from the information collected by the detector, is described. The selection cuts applied to data in order to extract the sample on which the asymmetry measurement was performed are outlined in Chapter 5. In Chapter 6, issues relating to understanding the data, looking for biases and checking for the misidentification of the charge of the muon, are addressed. Chapter 7 is about the different sources of backgrounds in the data. In Chapter 8, the final result for the charge asymmetry is presented along with a discussion of its significance.

CHAPTER 2

Theory

There are four types of interactions known to us. These are the electromagnetic, the strong, the weak and the gravitational interactions. The standard model is the theory that describes the first three of these interactions. Within the standard model, quantum electrodynamics (QED) is the theory of electromagnetic interactions, quantum chromodynamics (QCD) describes the strong interaction between quarks [1, 2], and the Glashow-Salam-Weinberg theory describes the electroweak interaction [3, 4, 5] which is the unification of electromagnetic and weak forces. A satisfactory and consistent quantum theory of gravity remains elusive.

2.1 The Standard Model

The standard model is the best available theory that explains the current experimental data. The fundamental particles of the standard model are spin-$\frac{1}{2}$ fermions and spin-1 bosons. There are two kinds of fermions: quarks, which participate in all three kinds of interactions, and leptons, which participate in only the electromagnetic and weak interactions (Table 2.1). Fermions interact by exchanging bosons and hence bosons are called the force carriers (Table 2.1). The photon is the carrier of the electromagnetic force, the eight gluons are the carriers of the strong force (between quarks) and the $W^{\pm}$ and Z bosons are the carriers of the weak force. If there were a quantum theory of gravitational forces, the force carrier would be the graviton and it would have spin-2. The standard model also postulates the existence of another boson called the Higgs boson (the only particle with spin 0) which breaks the electroweak symmetry between the photon, $W^{\pm}$ and Z, giving mass to the $W^{\pm}$ and Z bosons, as well as to the other fundamental particles. The Higgs boson has not yet been experimentally observed.

There are three generations of fermions. The first generation consists of the u (up) and d

Table 2.1: The fundamental particles of the standard model known as fermions which consist of three generations of leptons and quarks. Next to each fermion is its mass M (in GeV) and electric charge q (in multiples of elementary charge e). Fermions have spin-$\frac{1}{2}$ [6].

Generation	1^{st} (M, q)	2^{nd} (M, q)	3^{rd} (M, q)
Leptons	ν_e $(< 1 \times 10^{-8},\ 0)$	ν_μ $(< 0.0002,\ 0)$	ν_τ $(< 0.02,\ 0)$
	e $(0.00051,\ -1)$	μ $(0.106,\ -1)$	τ $(1.777,\ -1)$
Quarks	u $(\approx 0.003,\ +\frac{2}{3})$	c $(1.3,\ +\frac{2}{3})$	t $(175,\ +\frac{2}{3})$
	d $(\approx 0.006,\ -\frac{1}{3})$	s $(0.1,\ -\frac{1}{3})$	b $(4.3,\ -\frac{1}{3})$

(down) quarks, the electron (e), and the electron neutrino (ν_e). The u and d quarks together form a weak isospin doublet whereby one quark can transmute into its partner by exchanging a W boson. The e and ν_e also form an isospin doublet. The u quark carries a charge of $+\frac{2}{3}$ while the d quark carries a charge of $-\frac{1}{3}$. The electron has a charge of -1 while the neutrino is charge neutral. Each particle has a corresponding anti-particle which has the same mass but the opposite electric charge.

The other two generations of fermions follow the same pattern. The second generation of isospin doublets consist of the c (charm) and the s (strange) quarks and the μ (muon) and the ν_μ (muon neutrino). The third generation is made up of the t (top) quark, the b (bottom) quark, the τ (tau), and the ν_τ (tau neutrino). With the observation of the tau neutrino by the DONUT experiment in 2001 [7], all the quarks and leptons of the standard model have been experimentally observed.

Interactions in the standard model are defined by the so-called gauge symmetries. The requirement that a theory be invariant under certain local symmetry transformations naturally leads to the existence of gauge bosons which mediate the forces. Electromagnetic interactions are invariant under local $U(1)$ transformations. The corresponding gauge boson is the photon, γ. It couples to all particles with electric charge.

Gauge bosons have to be massless in order to satisfy the gauge symmetry. However, the carriers of the weak force, the $W^\pm$ and Z bosons, are very heavy. This can be explained by a partial spontaneous breaking of the gauge symmetry. At high energies, weak and electromagnetic interactions can be treated consistently as one force. This electroweak

Table 2.2: The gauge bosons of the standard model. These are the carriers of the four fundamental forces. Gravitons have not yet been found. The Higgs boson is the only scalar particle and does not fit into the usual scheme [6].

Interaction	Rel. Strength	Symmetry Group	Gauge Boson
Electromagnetic	1	$U(1)$	Photon γ
Weak	0.001	$SU(2)$	$W^{\pm}$, Z^0
Strong	100	$SU(3)$	8 Gluons g
Gravitational	10^{-40}	P	(Graviton ?)
Higgs Boson			H

interaction has the larger symmetry group $SU(2) \times U(1)$. However, in the ground state this symmetry is broken by the Higgs mechanism. Through this symmetry breaking, the $W^{\pm}$ and Z bosons acquire mass, yeilding a short range force. The residual $U(1)$ symmetry is respected by the electromagnetic force. Both leptons and quarks participate in weak interactions.

The gauge symmetry group of the strong force is $SU(3)$. Unlike leptons, quarks participate in the strong interactions and they have an additional degree of freedom known as color. Quarks come in three colors, usually labeled red, blue and green. Interestingly, the gauge bosons of the strong interaction, the gluons, themselves have a color charge. A key prediction of QCD is confinement which stipulates that free color charge cannot exist for very long. Instead, quarks can only exist in color neutral bound states called hadrons. There are two types of hadrons known as mesons and baryons. Mesons are made up of a quark-antiquark pair, carrying a color charge and the corresponding anti-color charge, which makes mesons color neutral. Baryons are made up of three quarks with three different colors which together add up to a color neutral state as well. Because of confinement, the strong interactions are short-range forces, with a typical length scale of 1 fm ($= 10^{-15}$ m).

The most important baryons are protons and neutrons which are color neutral and have electric charges +1 and 0 respectively. Protons and neutrons are the constituents of atomic nuclei and together with electrons make up all the matter that surrounds us.

The gravitational force is a long range force and many orders of magnitude weaker than the other three. However, at very high energies (at the Planck scale $\approx 10^{19}$ GeV), it is expected to become as strong as the other forces.

2.2 Parton Distribution Functions

As discussed in the previous section, quarks, the strongly interacting constituents of matter, and gluons, the carriers of the strong force, can only exist in bound states known as hadrons. The principle of confinement dictates that hadrons have to be color neutral. Protons and neutrons are made up of the quarks *uud* and *udd* respectively. Each quark has a different color — red, blue or green — so that the proton or neutron is color neutral as a whole. These quarks are called valence quarks. (Antiprotons correspondingly have a valence structure made up of two anti-u quarks ($\bar{u}$) and one anti-d quark ($\bar{d}$).) Besides the valence quarks, there are quantum fluctuations of gluons (which bind quarks together) and quark-antiquark pairs inside each hadron. These quark-antiquark pairs are called sea quarks. Quarks and gluons are together referred to as partons.

Experiments conducted with hadrons at sufficiently high energies tell us that scatterings actually take place between the individual quarks and gluons inside hadrons. In $p + \bar{p}$ collisions at a center of mass energy $\sqrt{s}$, the cross section $\sigma_{p+\bar{p}\to A}(s)$ (where $A = W$ for the production of a W boson) is the cross section $\hat{\sigma}_{a+b\to A}(\hat{s})$ of two partons a and b colliding with a center of mass energy $\hat{s}$ multiplied by $a_p(x_a)$, the probability to find a parton a inside the proton p carrying a fraction x_a of the proton energy, and $b_{\bar{p}}(x_b)$, the probability to find a parton b inside the antiproton $\bar{p}$ with momentum fraction x_b, such that $\hat{s} = x_a x_b s$. a_p and $b_{\bar{p}}$ are called parton distribution functions (PDFs). On integrating over the possible momentum fractions x_a and x_b (which can have values from 0 to 1), and summing over all possible combination of partons a and b in the proton and antiproton, we get

$$\sigma_{p+\bar{p}\to A} = \sum_{a,b} \int_0^1 dx_a \int_0^1 dx_b \; a_p(x_a) \; b_{\bar{p}}(x_b) \; \hat{\sigma}_{a+b\to A} \left(\frac{s}{x_a x_b} \right). \tag{2.1}$$

The cross section $\hat{\sigma}_{a+b\to A}$ between quarks and gluons can be calculated using perturbation theory (an expansion in the strong coupling constant α_s). On the other hand, parton distributions contain information about the bound states of the partons and can not be calculated in perturbative QCD which is why they have to be measured experimentally. A more careful study reveals that parton distributions are not only functions of the momentum fraction x, but they also depend on a "resolution scale" Q which is the momentum transferred in the collision.

How is a parton distribution $a_p(x, Q^2)$ defined?

Consider a proton with very large momentum P (e.g. a proton in the Tevatron as seen by an observer in the detector/lab frame). The probability to find a u quark in this proton with a momentum between xP and $(x + dx)P$ at a resolution Q^2 is $u_p(x, Q^2)dx$. Correspondingly, parton distributions can be defined for the quarks $\bar{u}$, d, $\bar{d}$, s, $\bar{s}$ (and sometimes for charm and bottom quarks as well). Parton distributions can also be defined for gluons.

What do we already know about parton distributions?

$$\int_0^1 dx\, a_p(x, Q^2) \tag{2.2}$$

is the total number of partons a in a proton for a fixed value of Q. However, this number is not well-defined and might even be infinite because of the presence of quantum fluctuations. What is well-defined is the number of valence quarks. The number of valence u quarks must be the difference between the total number of u quarks and the number of sea u quarks, while the number of sea u quarks in turn has to be equal to the number of sea $\bar{u}$ quarks (because sea quarks only exist as quark-antiquark pairs).
Hence in the case of a proton (uud),

$$\int_0^1 dx \left[u_p(x, Q^2) - \bar{u}_p(x, Q^2)\right] = 2 \tag{2.3}$$

$$\int_0^1 dx \left[d_p(x, Q^2) - \bar{d}_p(x, Q^2)\right] = 1 \tag{2.4}$$

for all Q. In addition, as there are no strange valence quarks

$$\int_0^1 dx \left[s_p(x, Q^2) - \bar{s}_p(x, Q^2)\right] = 0 \tag{2.5}$$

(which is also true for charm and bottom quarks).

The average momentum carried by gluons in the proton is given by

$$\int_0^1 dx\, x g_p(x, Q^2) \tag{2.6}$$

and this leads to the sum rule

$$\sum_a \int_0^1 dx\, x a_p(x, Q^2) = 1, \tag{2.7}$$

i.e. the sum of the momenta of all partons equals the total momentum of the proton (which is 100%). We can use the symmetry between particles and antiparticles to infer the parton distributions for the antiproton. For example,

$$g_p = g_{\bar{p}} \tag{2.8}$$

$$u_p = \bar{u}_{\bar{p}} \tag{2.9}$$

$$\bar{u}_p = u_{\bar{p}}. \tag{2.10}$$

2.2.1 Deep Inelastic Scattering

The first direct evidence for the existence of quarks inside protons was obtained from deep inelastic scattering (DIS) experiments. DIS experiments involve an electron scattering off a proton $e^- + p \to e^- + X$ with the proton typically breaking up. At higher energies, the wavelength associated with the electron is much smaller than the size of a proton, which is why the electron can be used to probe the internal structure of the proton. Since the proton breaks up in the reaction, the scattering is inelastic. The first DIS experiments were the fixed target experiments conducted at SLAC in the 1960s [8]. The H1 and ZEUS experiments at HERA operated in the 1990s at higher energies [9].

The only observables in an inclusive DIS experiment are the deflection angle θ and the final energy E' of the electron. If the momentum of the incident proton is P and the momenta of the electron before and after the scattering are p and p', respectively, the virtual photon exchanged between the electron and the proton in the interaction then has momentum $k = p - p'$. Instead of the variables θ and E', the cross section is often written as a function of two other equivalent variables. These are $Q^2 = -k^2$, the negative virtuality of the photon,

$$\text{and} \quad x = \frac{Q^2}{2P \cdot k}. \tag{2.11}$$

It is convenient to use x and Q^2 because parton distributions are expressed as functions of these variables. x is the momentum fraction of the quark struck by the virtual photon inside the proton and Q^2 is the square of the momentum transferred in the process.

The cross section for deep inelastic scattering is usually parametrized in terms of the two structure functions[1] F_1 and F_2

$$\frac{d^2\sigma}{dx\ dQ^2} = \frac{4\pi\alpha}{xQ^4}\left[y^2 x F_1(x, Q^2) + (1 - y)F_2(x, Q^2)\right] \tag{2.12}$$

[1]Structure functions are functions of x and Q^2 which describe the structure of hadrons[10].

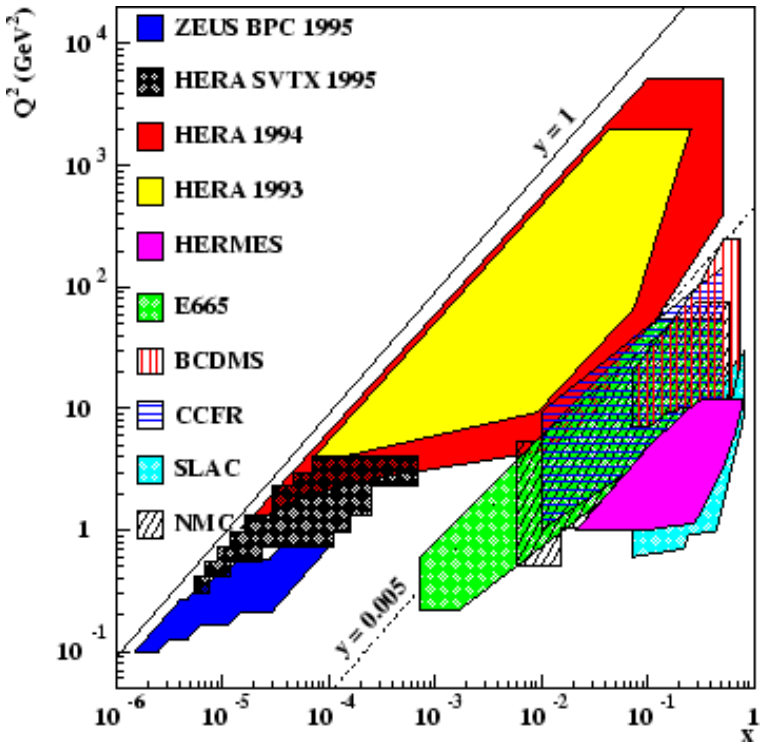

Figure 2.1: The range in x and Q^2 probed by various DIS experiments. ZEUS and HERMES were particle detectors at the electron-proton collider HERA at the DESY laboratory in Hamburg, Germany. E665 was a muon-proton collider experiment and CCFR was a fixed target experiment at Fermilab. BCDMS and NMC were muon scattering experiments at CERN, Switzerland. SLAC is the linear accelerator at Stanford, California.

where $y = (P \cdot k)/(P \cdot p) = Q^2/(xs)$ is the fraction of the energy of the incident electron carried by the photon.

Analogous to $p + \bar{p}$ collisions, the DIS cross section and the structure functions can be expressed as a convolution of the cross section for electron-quark scattering and a parton distribution that gives the probability to find the quark inside the proton with a given momentum fraction x. To lowest order in perturbation theory we simply have

$$F_2 = 2xF_1 = \sum_q e_q^2 \; x \; q_p(x, Q^2) \tag{2.13}$$

where e_q is the charge of the quark q. The sum runs over all quarks and antiquarks in the proton. Gluons are not relevant in leading order as they do not possess electric charge (hence the photon can not couple directly to the gluon). Higher orders in α_s introduce corrections

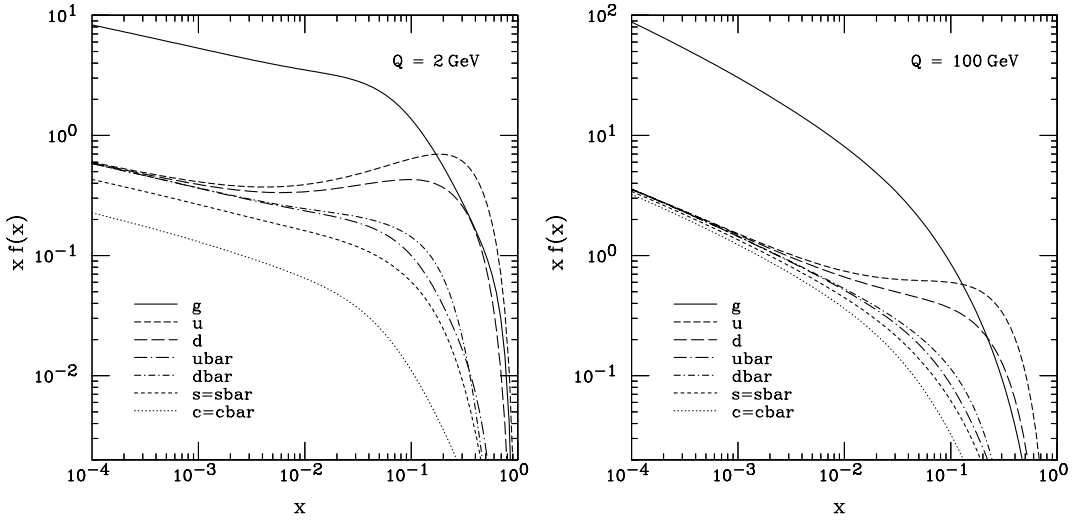

Figure 2.2: Overview of the CTEQ6M PDFs at $Q = 2$ GeV(left plot) and at $Q = 100$ GeV (right plot). $xf(x)$ is the probability density of the momentum fraction x.

to this equation, and in the next to leading order, it is possible to also probe the gluon content of the proton.

Figure 2.1 shows the kinematic region in x and Q^2 covered by various DIS experiments.

2.2.2 Current Status of Parton Distributions

The x-dependence of parton distributions cannot be predicted by means of perturbation theory. However, the Q^2-dependence can be evaluated using the DGLAP evolution equations [11]. DIS experiments measure structure functions at certain values of the pair of variables (x, Q^2). At a fixed low scale Q_0, an ansatz for the different parton distributions as a function of x is chosen where the ansatz contains a set of parameters. These PDFs are then evolved to higher values of Q^2 with the DGLAP equations and the structure functions are calculated. The parameters in the original ansatz are tuned by fitting the structure function data.

Besides deep-inelastic scattering via photon exchange, additional data is needed to unambiguously extract parton distributions for gluons and all quark flavors. DIS with W/Z exchange between the electron and the proton, DIS with positrons, and the Drell-Yan process (production of vector bosons in $p+p$ or $p+\bar{p}$) provide further information about the parton distributions. Another important contribution comes from the W charge asymmetry which

is measured in this analysis.

Several parameterizations of PDFs are available today. The most important of these are the CTEQ parton distributions [12], the MRST [13], and the GRV [14] parton distributions. Figure 2.2 shows the CTEQ parton distributions at two different values of Q^2 [15].

2.3 Electroweak Interactions

The force carriers of the weak interaction, $W^{\pm}$ and Z bosons, have mass. This is incompatible with the requirement of gauge symmetry. Glashow, Salam and Weinberg developed a beautiful theory in which the weak and electromagnetic interactions are unified into one electroweak force with symmetry group $SU(2) \times U(1)$ [3, 4, 5]. However, at low energies this gauge symmetry is spontaneously broken by the Higgs mechanism and the bosons acquire masses. This model has been experimentally verified over the last 25 years and is a centerpiece of the standard model.

In the electroweak theory, the symmetry $SU(2)$ refers to weak isospin I_w. It is represented by a triplet of vector bosons W_μ^i which couples only to the left handed weak isospin doublets. Left-handed means that only one of the two helicity states of these spin-$\frac{1}{2}$ fermions participates in the interaction. The right-handed versions are not affected. The left-handed and right-handed components of a fermion field ψ can be obtained by the projections

$$\psi_L = \frac{1-\gamma_5}{2}\psi \qquad \text{and} \qquad \psi_R = \frac{1+\gamma_5}{2}\psi. \tag{2.14}$$

where γ_5 is a Dirac matrix and can be represented as $\gamma_5 \equiv i\gamma^0\gamma^1\gamma^2\gamma^3$ [16]. Accordingly, the left-handed electron neutrino ν_e couples to the left-handed electron e, or the left-handed up quark couples to the left-handed down quark. [2] The electroweak interaction therefore violates parity which is the symmetry between left-handed and right-handed interactions.

The $SU(2)$ part of the electroweak Lagrangian is described by the term

$$\frac{g}{2}\,\bar{L}\,\gamma^\mu\,\sigma^i\,L\,W_\mu^i \tag{2.15}$$

where σ^i are the Pauli matrices [16], g is the $SU(2)$ coupling constant, and L is the left-handed weak ispospin doublet consisting of two left-handed fermion fields.

$$L = \begin{pmatrix} \psi_{1L} \\ \psi_{2L} \end{pmatrix} \tag{2.16}$$

[2] The right-handed neutrino does not participate in electroweak interactions.

This leads to the $\gamma^\mu - \gamma^\mu\gamma^5$ structure which is known as the vector−axial vector $(V-A)$ coupling of the fermion field ψ. $\bar{\psi}\gamma^\mu\psi$ is called the vector current while $\bar{\psi}\gamma^\mu\gamma^5\psi$ is the axial vector current.

The $U(1)$ part of the electroweak interaction couples to the so-called weak hypercharge Y [3] via a single vector boson B^μ and interacts with both right-handed and left-handed fermions with a coupling constant $g'/2$. The $U(1)$ part of the electroweak Lagrangian is described by the term $\frac{g'}{2}\,\bar{\psi}\,\gamma^\mu\,\psi\,B_\mu$.

Next we introduce a spin-0 boson H called the Higgs boson. It is an isospin doublet and couples both to the bosons W^i_μ and B_μ. If a certain form of self-interaction of the Higgs boson is assumed, a non-vanishing vacuum expectation value of one component of the Higgs isodoublet is permitted.

$$H = \begin{pmatrix} H^1 \\ H^0 \end{pmatrix} \rightarrow \begin{pmatrix} 0 \\ \eta + \sigma/\sqrt{2} \end{pmatrix} \tag{2.17}$$

Here η is the vacuum expectation value of the Higgs boson and σ is the remaining observable Higgs field which corresponds to oscillations around this expectation value.

The existence of the expectation value breaks the $SU(2) \times U(1)$ symmetry of the theory. In this state, the Lagrange density can be rewritten in terms of new boson degrees of freedom:

$$W^\pm = \sqrt{\frac{1}{2}}(W^1_\mu \mp iW^2_\mu), \tag{2.18}$$

$$Z^0_\mu = \frac{gW^3_\mu - g'B_\mu}{\sqrt{g^2+g'^2}} = -\sin\theta_W B_\mu + \cos\theta_W W^3_\mu, \tag{2.19}$$

$$A_\mu = \frac{g'W^3_\mu + gB_\mu}{\sqrt{g^2+g'^2}} = -\cos\theta_W B_\mu + \sin\theta_W W^3_\mu. \tag{2.20}$$

where θ_W is the Weinberg mixing angle, $\tan\theta_W = g'/g$. The $W^\pm$ and Z bosons have masses

$$M_W = \frac{g\eta}{\sqrt{2}} \qquad \text{and} \qquad M_Z = \frac{M_W}{\cos\theta_W} \tag{2.21}$$

while the boson A^μ is massless and can be identified with the photon. This is how the electromagnetic $U(1)$ theory is recovered. The coupling constant is the known electric charge $e = g\sin\theta_W$.

The $W^\pm$ bosons still only couple to left-handed isodoublets, (in reactions $u \rightarrow W^+ + d$), while the Z couples to both left- and right-handed fermions. An additional twist is added

[3] electric charge $Q = I_z + \frac{Y}{2}$, where I_z is the z component of the weak isospin I_w.

by mixing between the three generations of fermions. In some cases this would result in $u \to W^+ + s$ instead. The mixing amplitude between fermions a and b is described by the CKM matrix V_{ab} [10]. Recent measurements show that $M_W = 80.6$ GeV, $M_Z = 91.2$ GeV and $\sin\theta_W = 0.48$.

The parity violation in weak interactions and the $V - A$ (vector-axial vector) structure of the weak current can be experimentally demonstrated directly in electron-neutrino scattering. Measurements of the angular distributions of the $\nu_e e$ or the $\bar{\nu}_e e$ scattering show that the backward scattering of $\bar{\nu}_e e$ is prohibited by the conservation of angular momentum.

2.4 W Boson Production and Decay

After their experimental discovery at CERN more than 20 years ago [18], W and Z bosons are now routinely generated in collider experiments. Data samples of the W and Z bosons have become the testing ground for precision studies of the standard model. This section covers the hadronic production of the W boson, its leptonic decay and their relation to PDFs.

2.4.1 W Boson Production

W bosons are produced at hadron colliders in the reaction

$$A + B \to W^{\pm} + X. \tag{2.22}$$

where W bosons are produced primarily by quark-antiquark annihilation from the hadrons A and B. The cross section of a quark-antiquark subprocess to the lowest order in perturbation theory [10] can be written as

$$\hat{\sigma}(q\bar{q}' \to W^+) = 2\pi |V_{qq'}|^2 \frac{G_F}{\sqrt{2}} M_W^2 \delta(\hat{s} - M_W^2) \tag{2.23}$$

where q is a quark (or an antiquark) from hadron A, $\bar{q}'$ is an antiquark (or a quark) from hadron B, $V_{qq'}$ is the CKM matrix element, $\hat{s}$ is the quark-antiquark center of mass energy, M_W is the mass of the W boson and G_F is the Fermi coupling constant. The charged current coupling constant g is related to the Fermi coupling constant by the relation $g^2 = 4\sqrt{2} G_F M_W^2$.

The total cross section for the W^+ boson must then take into account the probability for finding q ($\bar{q}$) in A, the probability for finding $\bar{q}'$ (q') in B and a color factor 1/3. This can

be written as

$$\sigma(AB \to W^+X) = \frac{K}{3}\int_0^1 dx_a \int_0^1 dx_b \sum_q q(x_a, M_W^2)\bar{q}'(x_b, M_W^2)\hat{\sigma} \tag{2.24}$$

where x_a is the momentum fraction carried by q ($\bar{q}$) in A and x_b is the momentum fraction carried by $\bar{q}'$ (q') in B. The scale of the quark distributions is given by $Q^2 = \hat{s} = M_W^2$. To leading order, the value of K is one. The next to leading order (first order QCD corrections) approximation leads to a K-factor given by

$$K \approx 1 + \frac{8\pi}{9}\alpha_s(M_W^2) \tag{2.25}$$

Equation 2.24 can be rewritten as

$$\frac{d\sigma}{dy}(W^+) = K\frac{2\pi G_F}{3\sqrt{2}}\sum_{q,\bar{q}'}|V_{qq'}|^2 x_a x_b q(x_a, M_W^2)\bar{q}'(x_b, M_W^2), \tag{2.26}$$

if we transform to a different set of kinematic variables s and y using the relation

$$dx_a dx_b = \frac{d\hat{s}dy}{s}. \tag{2.27}$$

The rapidity y is defined as

$$y = \frac{1}{2}\left[\ln\left(\frac{E+P_z}{E-P_z}\right)\right], \tag{2.28}$$

and x_a and x_b can now be expressed as a function of y.

$$x_{a,b} = \frac{M_W}{\sqrt{s}}e^{\pm y}. \tag{2.29}$$

In the Cabibbo mixing approximation [10] and using the symmetry relations given by Eq. 2.8 - 2.10 , the W^+ differential cross section in $p\bar{p}$ collisions is

$$\frac{d\sigma}{dy}(p\bar{p} \to W^+ + X) = K\frac{2\pi G_F}{3\sqrt{2}}x_a x_b \left\{\cos^2\theta_C[u(x_a)d(x_b) + \bar{d}(x_a)\bar{u}(x_b)] + \sin^2\theta_C[u(x_a)s(x_b) + \bar{s}(x_a)\bar{u}(x_b)]\right\}. \tag{2.30}$$

where all the quark distributions are evaluated at $Q^2 = M_W^2$.

Further, assuming a flavor $SU(3)$ symmetric sea, the approximation $\bar{u} = \bar{d} = \bar{s}$ is used. Also, $\cos^2\theta_C = |V_{ud}|^2 = (0.97)^2 \approx 1$. As the interactions among valence partons dominate, the cross section is then

$$\frac{d\sigma}{dy}(p\bar{p} \to W^+ + X) = K\frac{2\pi G_F}{3\sqrt{2}}x_a x_b u(x_a)d(x_b). \tag{2.31}$$

The total cross section for W boson production is obtained by integrating over the full kinematic range of the W boson rapidity. Figure 2.3 shows the rapidity distributions of the $W^\pm$ cross sections as a function of the W rapidity, calculated using Eq. 2.31

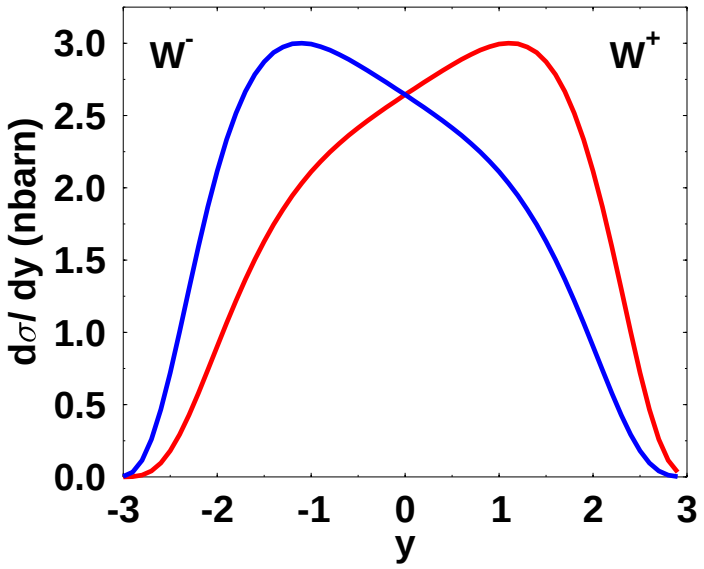

Figure 2.3: The leading order theoretical prediction for the $W^{\pm}$ production cross sections as a function of rapidity y, at the Tevatron.

2.4.2 W Boson Decay and Width

The W boson can be experimentally detected by its decay products. As described by the standard model, the W boson decays through the weak interaction to leptons or quarks. The W boson can decay into leptons $W \rightarrow l + \bar{\nu}_l$, where $l = e, \mu$ or τ and ν_l is the respective lepton neutrino, or the W boson can decay into hadrons via $W \rightarrow q + \bar{q}'$, where $q = u, c$ or t and $\bar{q}' = d, s$ or b quark. [4] The first observed decay of the W boson was in the electron channel. The partial decay width of the W boson in the case of leptonic decays is given by

$$\Gamma(W \rightarrow l\bar{\nu}_l) = \frac{G_F}{\sqrt{2}} \frac{M_W^3}{6\pi} \equiv \Gamma_W^0, \tag{2.32}$$

In the case of hadronic decays, there is an additional factor of 3 due to the quark colors. Taking into account that there are three quark generations, the total W boson width in leading order is calculated to be

$$\Gamma(W \rightarrow all) \approx 12\Gamma_W^0 \approx 2.51\,\text{GeV} \tag{2.33}$$

[4] Only a virtual W boson can decay into the heavier t or b quarks.

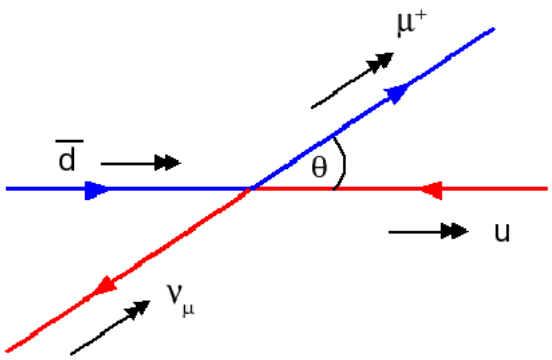

Figure 2.4: The process of $u\bar{d} \to \mu^+\nu_\mu$ in the W boson rest frame. The arrows on the lines represent the momenta of the particles while the double arrows indicate their helicity.

The measured value of the W boson width is 2.078 ± 0.087 GeV [17]. The partial width for W boson decay for electrons and muons is 0.229 GeV with a branching fraction of 9.14% [10].

2.4.3 W Boson Leptonic Decay

At hadron colliders, the W boson is primarily detected via the reconstruction of the electron and muon decay modes. Hadronic decay modes as well as the tau decay mode are all seen as jets and so are hard to distinguish from the large QCD backgrounds. Figure 2.4 shows the hadronic production and the leptonic decay of the W^+ boson in its rest frame. Due to helicity conservation in collinear scattering, the μ^+ is preferentially emitted along the direction of the $\bar{d}$.

From Eq. 2.24 the rapidity distribution of the W decay leptons in the laboratory rest frame can be written as

$$\frac{d\sigma}{dy}(AB \to lX) = \frac{1}{3}\sum_{q\bar{q}'}\int_0^1 dx_a \int_0^1 dx_b \; q(x_a)\; \bar{q}'(x_b)\left[\frac{d\hat{\sigma}}{d\cos\hat{\theta}}(q\bar{q}' \to l\nu)\;\sin^2\hat{\theta}\right], \qquad (2.34)$$

where the differential cross section for the process can be written as

$$\frac{d\hat{\sigma}}{d\cos\hat{\theta}} = \frac{|V_{ud}|^2}{8\pi}\left(\frac{G_F\; M_W^2}{\sqrt{2}}\right)^2 \frac{\hat{s}(1+\cos\hat{\theta})^2}{(\hat{s}-M_W^2)^2 + (\Gamma_W\; M_W)^2}. \qquad (2.35)$$

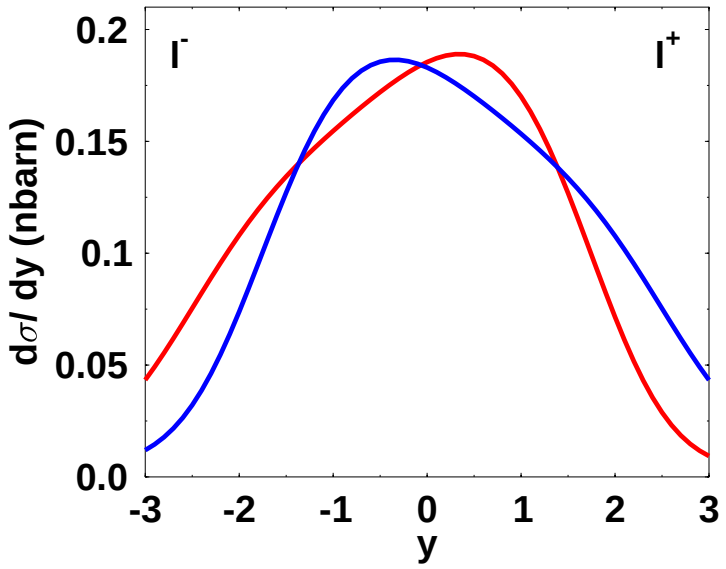

Figure 2.5: The leading order theoretical prediction for the cross sections of $l^{\pm}$ from the $W^{\pm}$ decay, as a function of rapidity at the Tevatron.

where $\hat{s}$ is again the squared center of mass energy of the two quarks, and $\hat{\theta}$ is the angle between $\bar{d}$ and μ^+. The cross section is evaluated at $\cos\hat{\theta} = \tanh\hat{y}$ where $\hat{y}$ is the rapidity of the lepton in the rest frame of the W and given by $\hat{y} = y - \frac{1}{2}\ln\frac{x_a}{x_b}$ in the lab frame. Figure 2.5 shows the rapidity distributions of charged leptons from the decay of the W in $p\bar{p}$ collisions at Tevatron energies.

2.5 The W Boson Charge Asymmetry

At the Tevatron, W bosons are mainly produced by quark-antiquark annihilations. A W^+ is produced primarily by the interaction of a u quark from a proton and a $\bar{d}$ quark from an antiproton and a W^- is produced primarily by the interaction of a d quark from a proton and a $\bar{u}$ quark from an antiproton (Fig.2.6). Contributions from valence-valence and valence-sea annihilations amount to about 85% of the cross section [19] with the rest coming from sea-sea quark-antiquark annihilations.

Because u valence quarks carry on average more of the proton's momentum than d valence quarks [20], the W^+ boson is boosted along the proton beam direction while the W^- boson

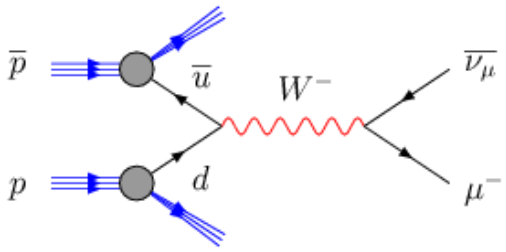

Figure 2.6: The dominant process for W^- production at the Tevatron

is boosted along the antiproton beam direction, giving rise to the W production charge asymmetry. This asymmetry therefore provides information on the relative momentum distributions of the u and d quarks in the proton.

The two most important processes for this analysis are:

$$u + \bar{d} \longrightarrow W^+ \longrightarrow \mu^+ + \nu_\mu$$
$$\bar{u} + d \longrightarrow W^- \longrightarrow \mu^- + \bar{\nu_\mu}$$

The W Production Charge asymmetry is defined as:

$$A(y_W) = \frac{\frac{d\sigma(W^+)}{dy} - \frac{d\sigma(W^-)}{dy}}{\frac{d\sigma(W^+)}{dy} + \frac{d\sigma(W^-)}{dy}}, \tag{2.36}$$

where $d\sigma(W^\pm)/dy$ is the cross section for the $W^\pm$ as a function of rapidity y and Using Eq. 2.31 in Eq. 2.36, we find that

$$A(y_W) = \frac{\frac{d(x_b)}{u(x_b)} - \frac{d(x_a)}{u(x_a)}}{\frac{d(x_b)}{u(x_b)} + \frac{d(x_a)}{u(x_a)}}. \tag{2.37}$$

In other words, the W charge asymmetry is sensitive to the ratio of the momenum fractions of the u and d quarks in the proton.

In a hadron collider, the longitudinal momentum of the neutrino from the W decay can not be measured because of energy lost down the beam pipe. The W boson therefore cannot be reconstructed without making certain assumptions.. Instead, we access the information by measuring the charge asymmetry of the W boson decay products [24]. In this analysis we use the muon decay channel. The muon asymmetry is a composition of the W production

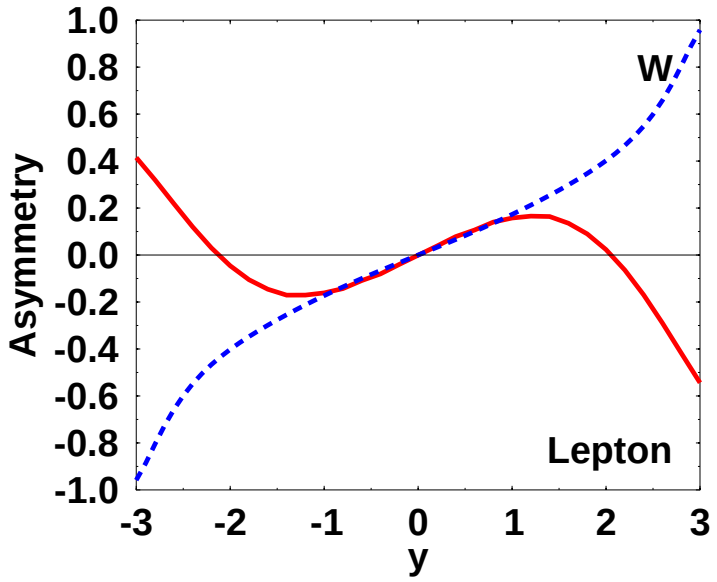

Figure 2.7: Comparison of the W production charge asymmetry (in blue)and the decay lepton charge asymmetry (in red) over all momenta.

charge asymmetry and the asymmetry from the $(V-A)$ decay. Since the $(V-A)$ asymmetry is well understood, the muon asymmetry can be used almost as effectively to probe the parton distributions. The muon charge asymmetry is defined as

$$A(y_\mu) = \frac{\frac{d\sigma(\mu^+)}{dy} - \frac{d\sigma(\mu^-)}{dy}}{\frac{d\sigma(\mu^+)}{dy} + \frac{d\sigma(\mu^-)}{dy}}, \tag{2.38}$$

where $d\sigma(\mu^\pm)/dy$ is the cross section for the $W^\pm$ decay muons as a function of muon rapidity. This cross section is measured as

$$\frac{d\sigma(\mu^\pm)}{dy} = \frac{N_{\mu^\pm}(y)}{\mathcal{L}\mathcal{A}\varepsilon_\pm(y)}, \tag{2.39}$$

where $\varepsilon_+(y)[\varepsilon_-(y)]$ is the muon identification efficiency for positive [negative] muons in the rapidity bin y, $\mathcal{L}$ is the integrated luminosity, $\mathcal{A}$ is the acceptance and $N_{\mu^+}(y)[N_{\mu^-}(y)]$ is the number of positive [negative] muons in that rapidity bin. Taking the luminosity and acceptance to be charge independent, and the efficiencies for the positive and negative muons to be the same, the muon charge asymmetry can be simplified to:

$$A(y_\mu) = \frac{N_{\mu^+}(y) - N_{\mu^-}(y)}{N_{\mu^+}(y) + N_{\mu^-}(y)} \ .$$

In this analysis, the muon charge asymmetry is measured as a function of the pseudo-rapidity η, which is defined as $\eta = -\ln[\tan(\theta/2)]$ where θ is the polar angle. In the relativistic limit, rapidity y is the same as pseudo-rapidity η.

In $p\bar{p}$ collisions at the Tevatron, the resonant production of the W boson constrains Q^2 to $\approx M_W^2$, where M_W is the mass of the W boson. Hence the region in phase space in x that this measurement can probe depends on the range of the rapidity of the W boson, y_W, that can be measured and is given by

$$x_{a,b} = \frac{M_W}{\sqrt{s}} e^{\pm y_W}, \tag{2.40}$$

where $\sqrt{s}$ is the center of mass energy and $x_{a,b}$ is the momentum fraction carried by the $u(d)$ quark. At $\sqrt{s} = 1.98$ TeV and for W rapidities between $-2 < \eta < +2$, this measurement probes the region in x that lies between 0.005 and 0.3.

Figure 2.7 shows the predicted asymmetries for the W boson production and the decay leptons over all lepton momenta. While the W charge asymmetry is not a function of the lepton kinematic cuts, the lepton charge asymmetry is sensitive to such cuts. At larger momenta, the $V - A$ contribution decreases and the lepton charge asymmetry is larger. At higher rapidities, the $V - A$ contribution is larger and the asymmetry is smaller.

2.6 Why measure the W Charge Asymmetry?

Parton distribution functions are one of the most important quantities that enters all theoretical calculations for hadron colliders. At some level, every hadron collider cross section prediction is sensitive to the uncertainties in these phenomenological quantities. In order to compare certain experimental results to theory, PDFs must accurately model the internal structure of the nucleon. As discussed earlier, PDFs are typically evaluated from deep inelastic scattering experiments at low x and evolved to higher values of Q^2. The W charge asymmetry measured at the Tevatron provides complementary information that is not directly obtained from DIS experiments. Since the value of Q^2 is much higher, this measurement will be free of potential theoretical uncertainties associated with the Q^2 evolution.

A more accurate knowledge of PDFs help reduce the systematic uncertainties in the measured mass of the W boson and the top quark as these measurements make use of models that depend on the PDFs. These measurements in turn help constrain the possible

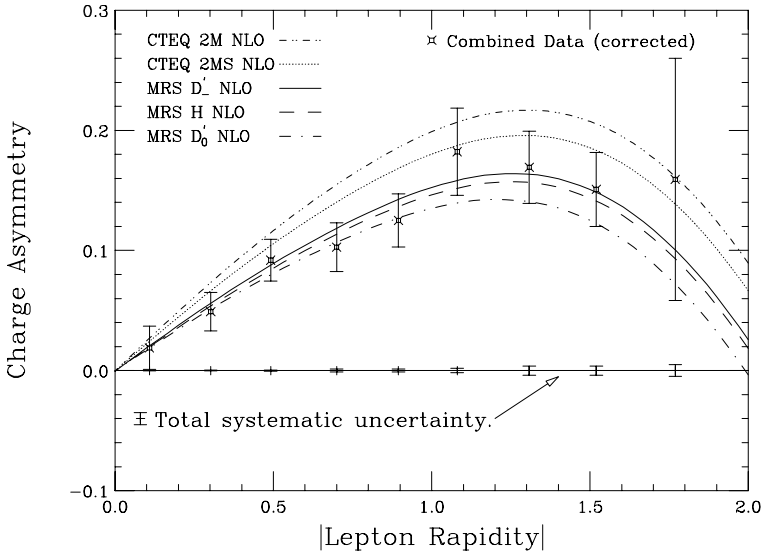

Figure 2.8: The Run I W charge asymmetry results from CDF [26].

mass of the Higgs boson. Besides being important experimental tests of the standard model, any deviations in these measurements from current theoretical predictions could point to new physics. As of yet, the Tevatron is the only place in the world where the W charge asymmetry can be measured.

The W charge asymmetry was measured by the CDF collaboration in Run I [24, 25, 26]. Figure 2.8 shows the published final Run I results from CDF. These results were used as inputs in the most recent PDF parameterizations. The W charge asymmetry was also measured by CDF in the electron channel in Run II [27]. Figure 2.9 shows these results. There was a DØ Run I thesis of the W charge asymmetry in the muon channel [28] but the results were not published. More recently, there has been a DØ Run II thesis in the electron channel [29] but the results have not yet been shown outside the collaboration. With the addition of the central magnetic field to the DØ detector to aid charge discrimination, the DØ collaboration is much better equipped in Run II to perform this analysis and the large data sample collected provides a competitive measurement of the W charge asymmetry.

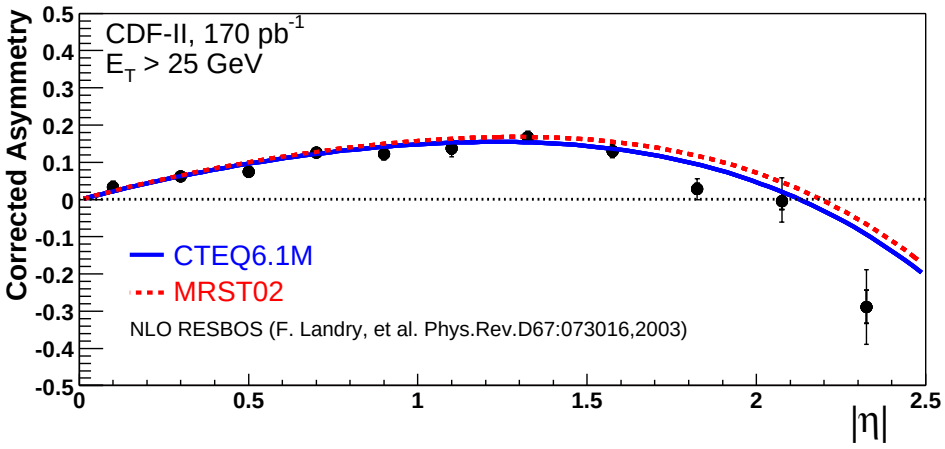

Figure 2.9: The Run II W charge asymmetry results in the electron channel from CDF [27].

CHAPTER 3

The Experimental Apparatus

The Fermi National Accelerator Laboratory (Fermilab), located about 40 miles west of Chicago, Illinois, is home to the Tevatron, currently the highest energy particle accelerator in the world. Protons and anti-protons are boosted to high energies as they are passed through a chain of accelerators. They are then made to collide within the Tevatron with a centre of mass energy of 1.96 TeV. The two collider detectors, DØ and CDF, built at two of the possible six collision points around the Tevatron, record the end results of these collisions.

3.1 The Tevatron

A bottle of hydrogen is the starting point in the production of protons and antiprotons used in the Tevatron collisions. The Tevatron collider is the final stage in a series of seven accelerators: a Cockroft-Walton pre-accelerator, a linear accelerator (Linac), a synchrotron (Booster), an anti-proton Debuncher, an anti-proton Source and the Main Ring synchrotron. Fig 3.1 shows the schematic diagram of the accelerator complex. A detailed description of the individual components can be found in Ref. [31].

Negative hydrogen ions are produced at 18 keV in a magnetron surface plasma source and accelerated to 750 keV in the Cockcroft-Walton accelerator which is a voltage multiplier circuit that generates a high voltage by charging capacitors in parallel and discharging them in series. The hydrogen ions are then accelerated to 400 MeV in a 150 m long linear accelerator called the Linac [32]. The Linac consists of 12 radio-frequency (RF) cavities which increase in length along the direction of acceleration to provide constant particle acceleration. The hydrogen ions are then passed through a carbon foil to strip away the electrons. The protons that emerge are then injected into the Booster.

The Booster is an 8 GeV fast cycling proton synchrotron with a diameter of 151 m,

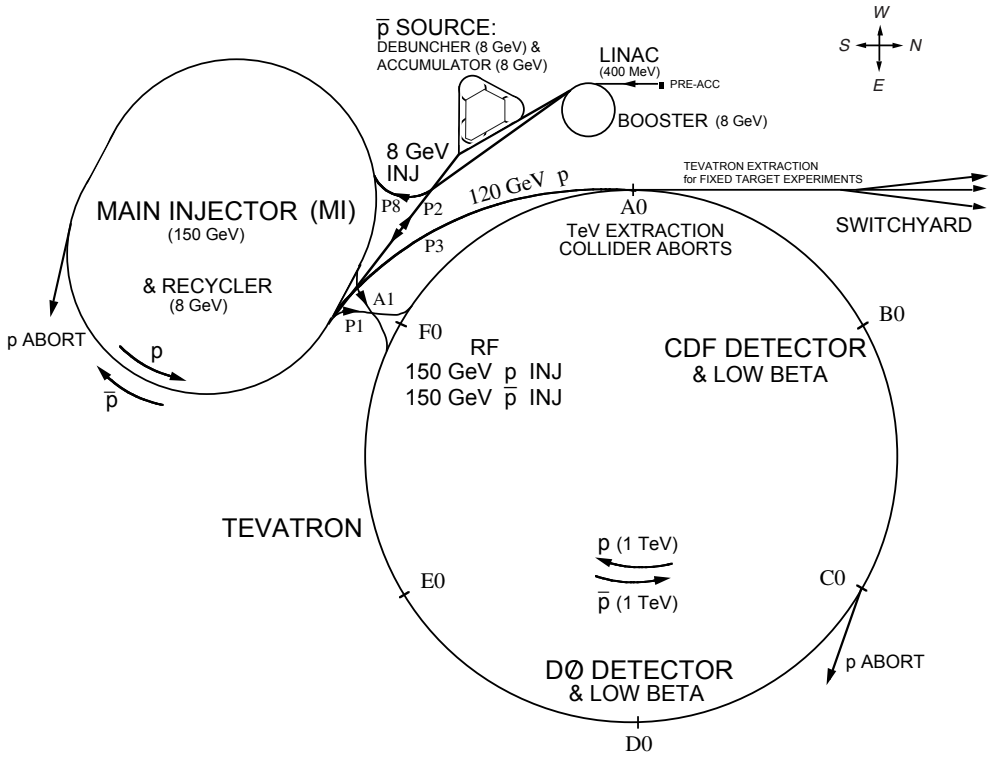

Figure 3.1: The Fermilab Tevatron accelerator.

which serves as a step up for the Main Injector [33]. The Booster consists of 17 dual gap cavity resonators for acceleration and a set of 96 dipole/quadrupole magnets to steer and focus the beam. The Main Injector is a 150 GeV proton synchrotron with a circumference of 3 km [32]. The Main Injector serves two purposes, accelerating protons to 150 GeV for transfer to the Tevatron or accelerating protons to 120 GeV for transfer to the $\bar{p}$-source to generate anti-protons [34].

In the $\bar{p}$-source, 120 GeV protons are collided against a nickel target resulting in the production of many secondary particles. The rate of production of anti-protons are approximately one out of every 10^5 collisions. A lithium lens is used to focus the particles and a pulsed dipole magnet directs 8 GeV negatively charged particles to the Debuncher. The Debuncher narrows the momentum spread and reduces the transverse profile of the anti-proton beam which is then transferred to the Accumulator. The Accumulator works by stochastic cooling which samples the particle momenta and decelerates them to move

the particles into a smaller orbit within the machine. In this orbit, called the Stack Core, the momentum spread of the particles is controlled. The anti-protons are stored in the Accumulator for hours or days until enough have been collected ($\approx 2 \times 10^{12}$) to fill the Tevatron.

The Tevatron receives 150 GeV protons and anti-protons from the Main Injector and accelerates them to an energy of 0.98 TeV [32]. The Tevatron has a radius of 1 km and uses 774 dipole magnets and 216 quadrapole magnets with a strength of 4.2 Tesla to steer and focus the beams. Protons are accelerated clockwise, anti-protons counter clockwise. The Tevatron uses 36 bunches of protons and 36 bunches of anti-protons which collide every 396 ns. Each proton bunch has approximately 3×10^{11} protons and each anti-proton bunch has approximately 5×10^{10} anti-protons. There are currently two interaction regions around the Tevatron and the DØ detector is situated at one of them.

3.2 The DØ Detector

The DØ detector is a multi-purpose particle detector built to study the end results of $p\bar{p}$ collisions at the Tevatron. It is 17 m long, 11 m wide, 13 m tall and it weighs 5500 tons. Figure 3.2 shows an overview of the DØ detector. The physics aims of the experiment are to conduct studies of the W and Z bosons and the top quark and search for new phenomena and the Higgs Boson among other things. This requires that the detector be able to identify leptons accurately, measure energy precisely, and have the ability to identify the decay products of primary particles produced in the $p\bar{p}$ collisions. For this purpose, the detector was designed for the study of large mass states and high p_T phenomenon.

The DØ detector has an almost 4π coverage excluding the region around the beam pipe. The detector consists of a central tracking system in it's innermost region which is composed of the Silicon Microstrip Tracker (SMT) and the Central Fiber Tracker (CFT) contained within a 2 Tesla superconducting solenoid magnet. Almost all particles leave tracks when passing through the central tracker while the magnetic field causes charged particles to bend. The tracker is surrounded by a sampling liquid-argon/uranium calorimeter which measures the energy deposited by electrons, photons and jets. Preshower detectors, located between the solenoid and calorimeters aide in electron identification. All particles other than muons and neutrinos deposit all their energy in the calorimeter. Whereas the neutrinos pass through the detector without interacting with it, muons leave a trail in the detector. The outermost

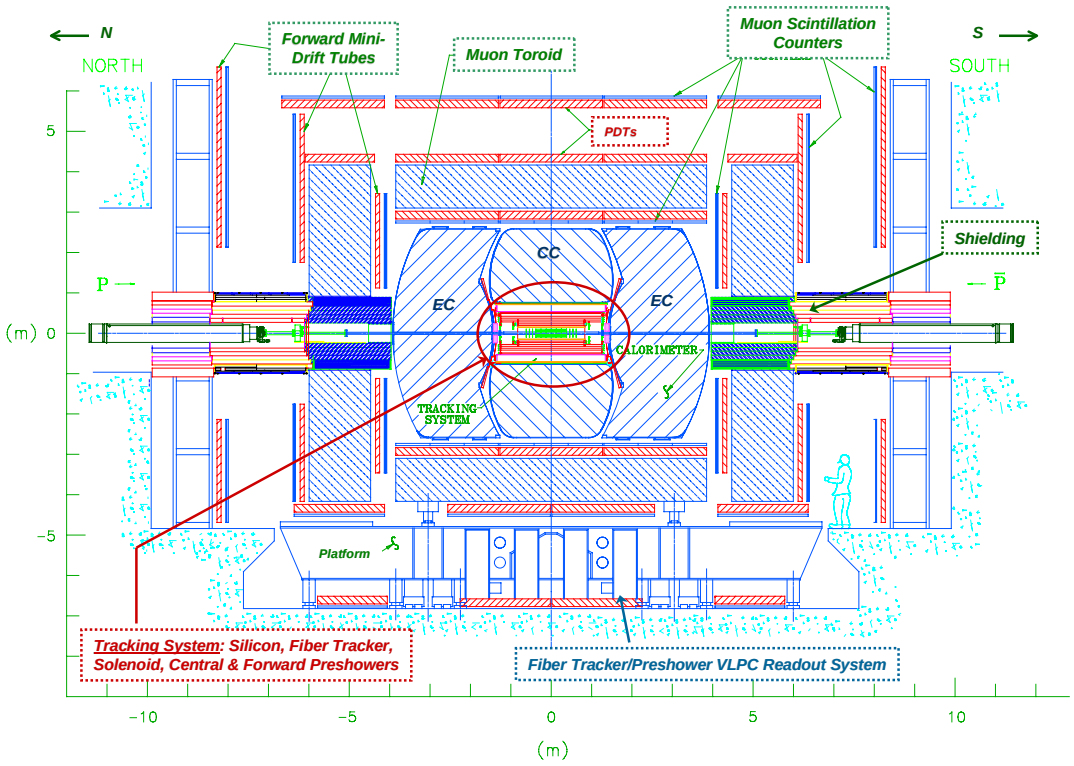

Figure 3.2: The RunII DØ detector.

detector is therefore the muon detector and is used to identify muons. The muon detector consists of three layers of scintillators and drift tubes with a 2 Tesla toroid magnet beyond the first layer of the muon detector. The individual components of the DØ detector are described in great detail in Ref [35] and most of the text in this chapter borrows heavily from that document.

3.3 The DØ coordinate system

DØ uses a standard right-handed coordinate system with the positive z axis defined as the proton direction and the negative z axis defined as the anti-proton direction. At DØ, protons travel south within the beam pipe that passes through the center of the detector. The y-axis points vertically upward while the x-axis points horizontally towards the center of the ring. DØ uses azimuthal angle ϕ in the $x-y$ plane and polar angle θ in the $y-z$ plane to determine the position of objects in the detector. $\theta = 0$ lies along the beam pipe.

The events of greatest interest in $p\bar{p}$ collisions are usually hard-scattering interactions between constituent partons within the hadrons. The new particles resulting from these interactions are often created with large transverse momenta. The center of mass of these interactions is usually boosted along the z direction. The non interacting partons left over from the disintegration of the hadrons escape down the beam pipe making it impossible to measure the longitudinal boost of the interactions. Since very little of the transverse momentum p_T of the particles is lost down the beam pipe, the conservation of energy and momentum can be applied in the transverse plane. The transverse momentum p_T, the transverse energy E_T and the transverse missing energy $\not\!\!E_T$are all extensively used variables in hadron collider experiments.

It is common to measure the rapidity y of particles in collider experiments because rapidity intervals are Lorentz invariant and particle multiplicity is approximately constant in rapidity. The rapidity y is defined as

$$y = \frac{1}{2} \ln \left(\frac{E + p_z}{E - p_z} \right). \tag{3.1}$$

The pseudo-rapidity of particles is also measured where the psuedo-rapidity η is related to the polar angle θ as

$$\eta = -\ln \left[\tan \left(\frac{\theta}{2} \right) \right]. \tag{3.2}$$

In the relativistic limit $p \gg m$, rapidity $y \approx$ pseudo-rapidity η. Rapidity y is useful for discussing physics processes while pseudo-rapidity η is the guiding principle used for designing detectors.

3.4 The Central Tracker

The tracking system in Run I was composed of a central transition radiation detector and drift chambers in the central and forward region. The absense of a magnetic field around the interaction region made charge discrimination impossible. The entire tracking system was replaced in Run II. The Run II central tracker is composed of a Silicon Microstrip Tracker (SMT), a Central Fiber Tracker (CFT), a solenoid magnet, and pre-shower detectors. Fig. 3.3 shows a cross section of the central tracker.

Charged particles interact with the tracking detectors and leave a pattern of 'hits' in the various layers of the detectors. Tracks can be reconstructed from the hits and represent the

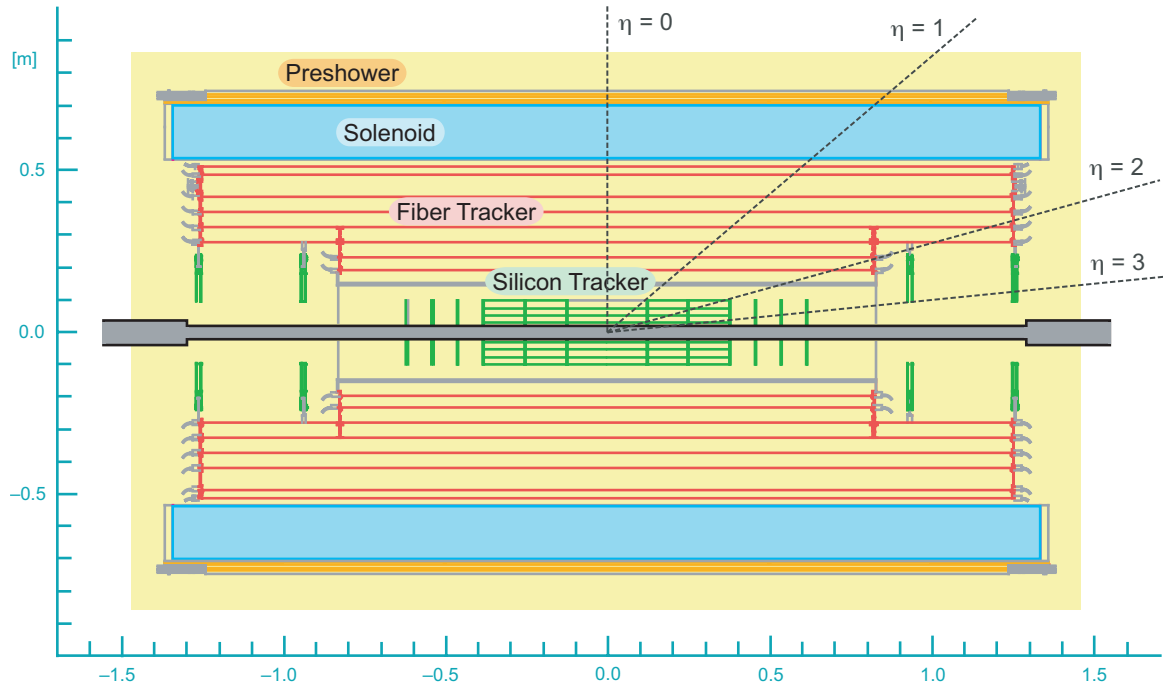

Figure 3.3: A cross section of the DØ Run II central tracking system.

trajectories of charged particles. The SMT provides good spatial resolution in the area closest to the beam line. The CFT provides a fast trigger for tracks. The magnetic field causes the trajectories of charged particles to be curved allowing their momenta to be measured. The preshower detectors sample the energy in showers that started in the material of the tracker and the solenoid and thus provides additional separation between electrons and photons from QCD jets. Tracks in the central tracker can be matched with information from the other sub-detectors for better particle identification.

3.4.1 Silicon Microstrip Tracker

The Silicon Microstrip Tracker (SMT) is the closest detector subsystem to the beamline and to the proton-antiproton collision region. It has the highest position resolution of all the sub-detectors and is used to match tracks to the primary vertex ($p\bar{p}$ interaction point) or to a secondary vertex associated with a long-lived particle like a B hadron. The SMT detector is made up of six barrels, twelve F disks interspersed along the barrels, and four larger disks called the H disks which cover the far forward region $|\eta| < 3$. Fig. 3.4 shows the schematic

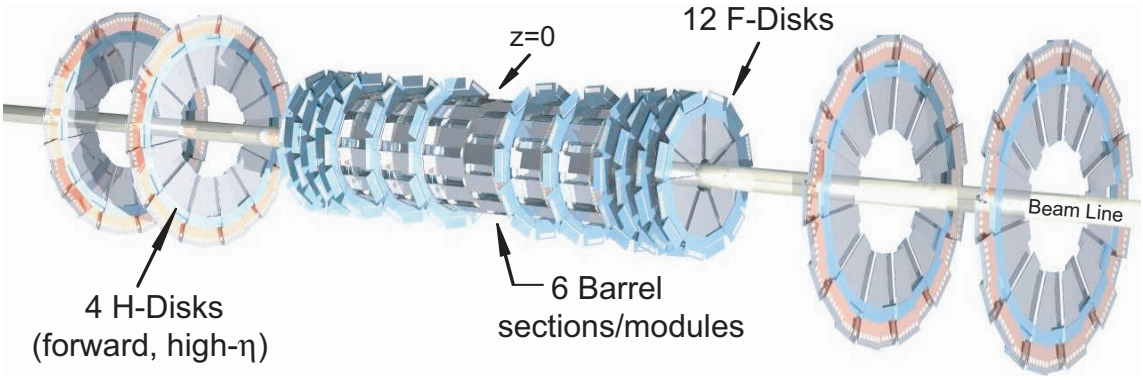

Figure 3.4: The Silicon Microstrip Tracker.

diagram of the SMT system.

Both the barrels and disks are made of n-type silicon wafers that are 300 μm thick. The strips are heavily doped along the length of the detector. A thin dielectric layer between the strips and an aluminum coating forms a capacitor which AC couples the detector to the readout electronics. A radiation hard polysilicon resistor is used to bias the sensor. The sensors operate essentially as reverse biased diodes.

The distribution of interaction points in the beampipe has a mean at $z = 0$ and a standard deviation of $\sigma_z = 28$ cm. The SMT was designed with the disk and barrel topology in order to track particles originating from this relatively long interaction region. The barrels are 12.0 cm long and 21.0 cm in diameter. Each barrel has four layers of silicon modules (called "ladders") at radii ranging from 2.7 cm to 10.5 cm. Each layer has an inner and outer sub-layer. For the four central barrels, layers 1 and 3 have single-sided silicon sensors while layers 2 and 4 have double-sided silicon sensors. The outermost two barrels have single-sided silicon sensors. There is overlap between adjacent ladders for complete detection. Fig. 3.5 shows the cross section of a barrel.

The active part of the silicon sensor is segmented into a series of parallel strips. The barrel module detectors are 12 cm long with 50 μ m strip pitch. The double sided detectors have axial strips parallel to the beam on one side while the strips on the other side are placed at an angle (either at 2° or 90°) with respect to the beam. The pitch of the strips provides an $r - \phi$ hit resolution of approximately 14 μm. The sensors are read out by SVX-

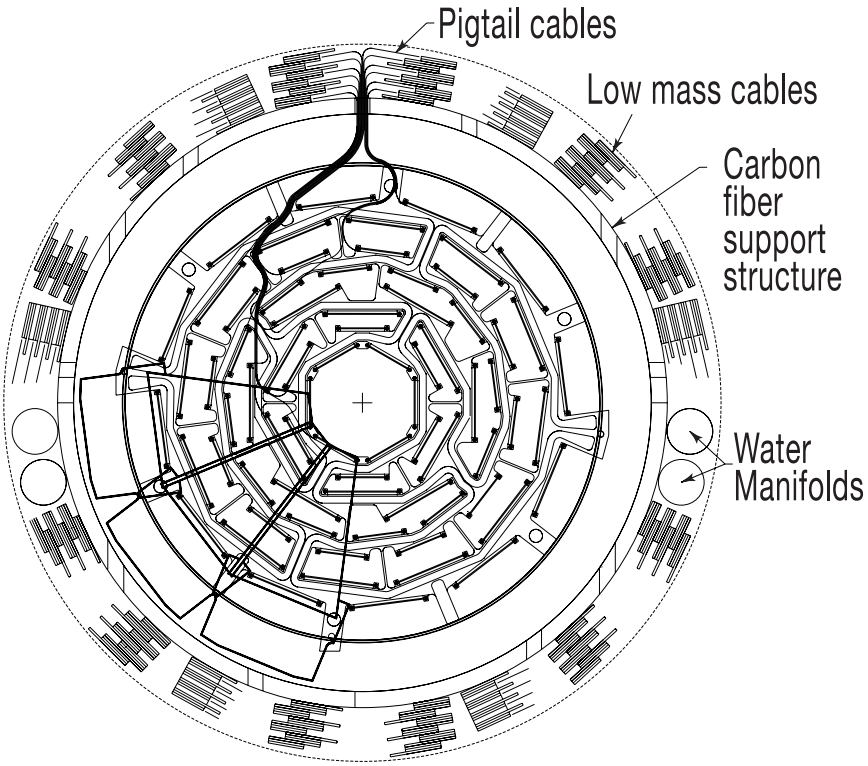

Figure 3.5: Cross section of an SMT barrel in the $x - y$ plane.

II chips which digitize the collected charge. The SVX-II chips are mounted on kapton high density interconnects (HDIs), which form part of the ladder. The ladders are supported by bulkheads that also water-cool the ladders to an operating temperature of around 5-10° Celsius. The SMT detector has approximately 800,000 readout channels in total. A typical ladder is shown in Fig. 3.6.

The 12 F-disks, are constructed from 12 overlapping wedges. Each wedge is double-sided with a height of 7.5 cm. The readout strips are at a stereo angle of 15°. There are separate 8-chip HDI's to read out both sides of a wedge. The 4 H-disks lie at $z = \pm 110$ cm and $z = \pm 120$ cm. The H-disk are made of single-sided wedges, 14.86 cm high. Twenty-four wedges make up one H-disk.

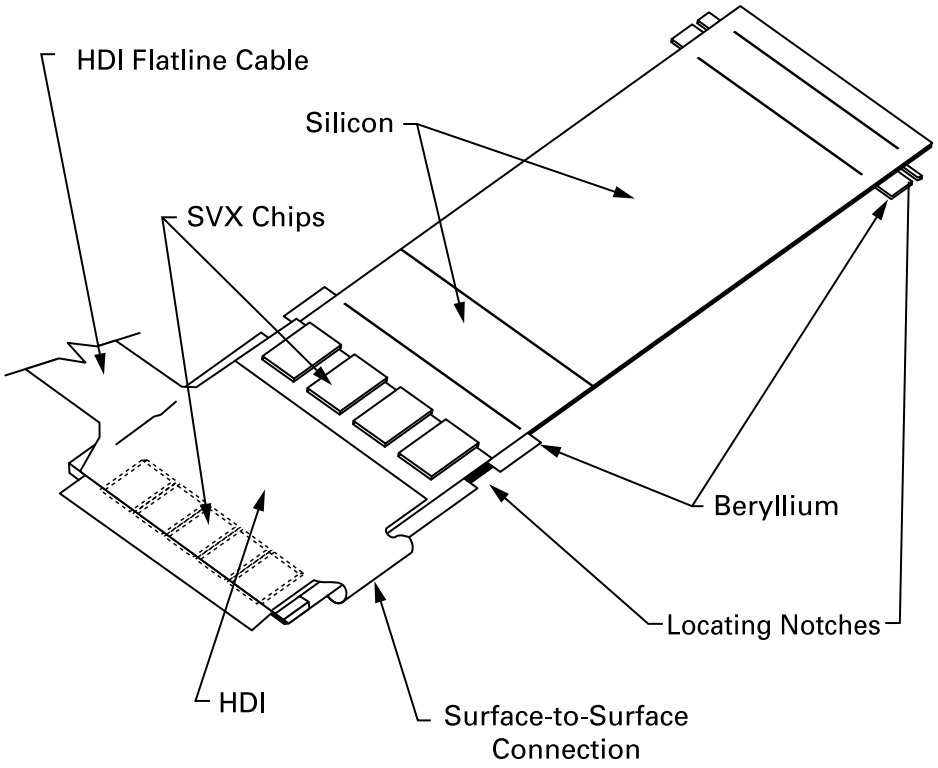

Figure 3.6: A typical SMT ladder.

3.4.2 Central Fiber Tracker

The Central Fiber Tracker (CFT) consists of scintillating fibers mounted on eight concentric cylinders. The cylinders extend from a radius of 20 to 52 cm. The two cylinders closest to the beamline are 1.66 m in length in order to accomodate the SMT H-disks. The six outer cylinders are 2.52 m long. Each cylinder consists of doublet layers with one layer parallel to the beam axis and the other layer oriented at a stereo angle of 2° with respect to the beam. There are a total of 76,800 scintillating fibers in the CFT. The scintillating fibers are 860 microns thick and between 1.7 and 2.6 meters long. The fibers were assembled into ribbons consisting of 256 fibers in two layers of 128 each. The CFT is organized into 80 sectors of 45° in ϕ to aid readout and triggering. Fig. 3.7 shows the CFT cross section and the structure of the fibers in the cylinders.

The scintillating fibers have a multi-clad structure consisting of a core surrounded by two claddings. The fibers have a base core of polystyrene (PS), doped with the organic

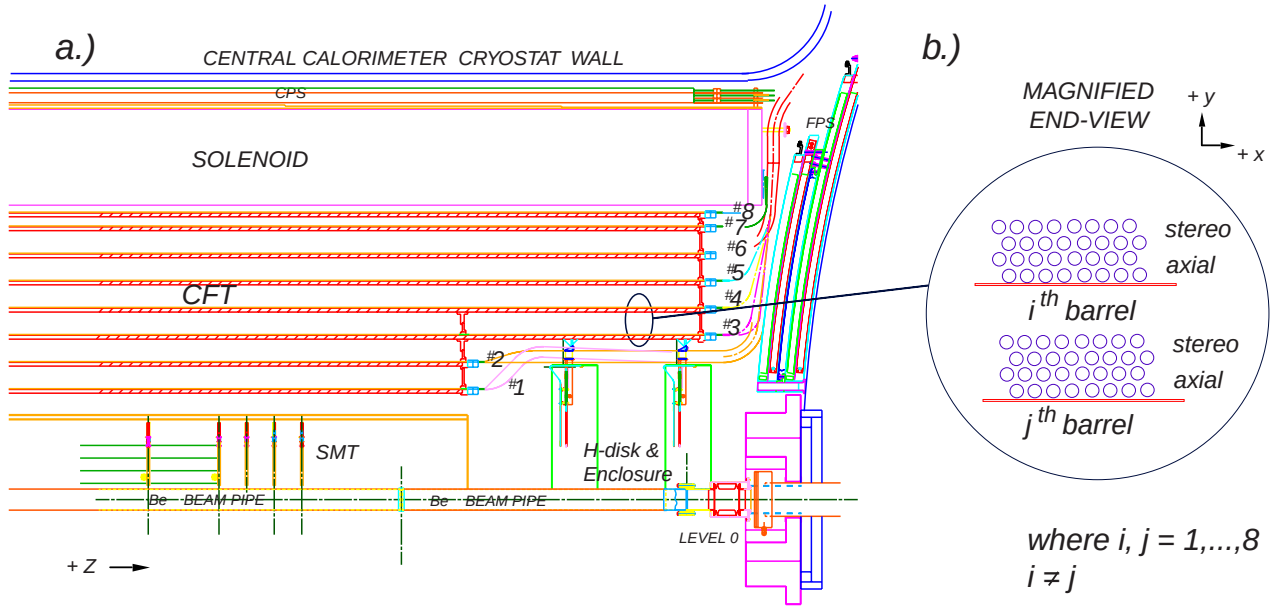

Figure 3.7: Cross Section of the CFT detector.

fluorescent dye paraterphenyl (pT) at about 1% by weight and with 3-hydroxyflavone (3HF) at a lower concentration. The polystyrene absorbs energy from incident ionizing radiation but has a long relaxation time. The excitation in PS is quickly transferred to the pT which promptly decays back to the ground state within a few nanoseconds by radiating a photon. However, pT emits light with a very short wavelength. Hence the other dye, 3HF, is used as a secondary wavelength shifter to get the light out of the detector. Light is collected from only one end of the scintillating fibers. The fibers are connected through an optical connector to a clear fiber waveguide. The waveguide transmits scintillation light to a Visible Light Photon Counter (VLPC), which converts the light into electrical pulses. The VLPCs are able to detect single photons and operate in a high background environment. The VLPC cassette is divided into 8 modules of 128 channels each, which give 1024 individual pixels for light detection. The VLPCs require a liquid Helium cryosystem to operate at a constant temperature of 9K.

3.4.3 Solenoid

The solenoid surrounds the inner tracking system and lies just before the central preshower. It creates a highly uniform axial magnetic field of 2 Tesla, constant upto 0.5% in the tracking region. The magnetic field causes the trajectory of charged particles to bend and hence makes it possible to measure the momentum of the particles. The solenoid is 2.73 m long and has a diameter of 1.42 m. The solenoid is constructed of two grades of superconducting high purity aluminum stabilized multi-filamentary Cu-NbTi cable.

The magnet runs at a current of 4825 A and stores 5.6 MJ of energy. In order to maintain such a high current the magnet must be superconducting. Liquid Helium is used to cool the solenoid to its operating temperature of 4.7 K. The low temperatures are necessary for the coil to conduct without resistance. To maximize the field uniformity inside the bore of the magnet, the current density in the windings is larger at the ends of coil. This is made possible by using a narrower conductor at the ends of the coil. The bulk of the coil and cryostat that make up the solenoid assembly is about 0.87 radiation lengths thick.

3.4.4 Pre Shower Dectectors

The Preshower Detector consists of the Central Preshower (CPS) and the Forward Preshower (FPS). The Preshower detectors are installed just outside of the magnet and before the calorimeter. Particles exiting the tracking volume must pass through a significant amount of material introduced by the presence of the solenoid, before they reach the calorimeter. This causes the particles to lose energy and this energy loss depends on the amount of material the particle passes through which can be determined by η. The purpose of the preshower detectors is to help restore electromagnetic energy resolution and particle identification in the calorimeter. These detectors consist of lead absorbers and plastic scintillating tiles. Additional lead sheets of varying thickness surrounds the solenoid to make the radiation length approximately the same for all particle trajectories. The radiation length X_0 is defined as the mean distance over which an electron loses all but $\frac{1}{e}$ of its energy [6]. Fig. 3.8 shows the location and structure of the preshower detectors.

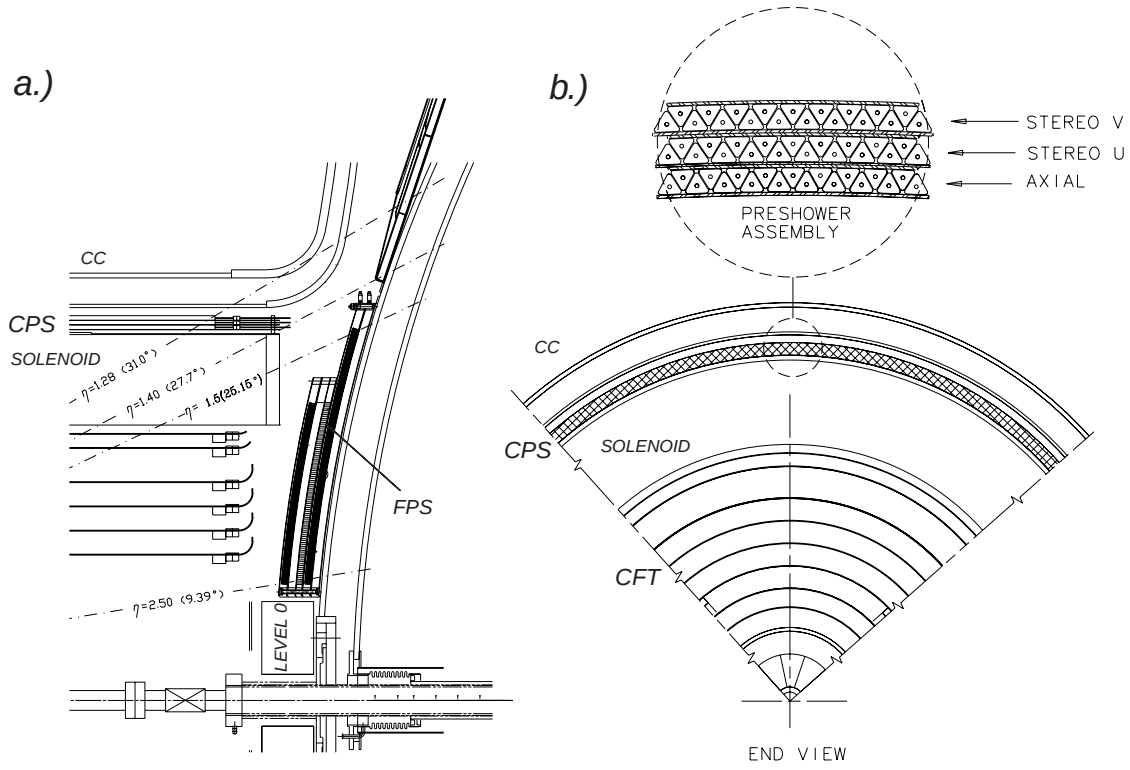

Figure 3.8: The central and forward pre-shower detectors.

3.5 Calorimeter

The DØ calorimeter is a liquid argon-uranium sampling calorimeter. The calorimeter provides energy measurements of electrons, photons, and jets. It also provides particle identification using the shapes of the energy distribution over the cells. The calorimeter consists of and is housed in three separate cryostats, a Central Calorimeter (CC), that covers the range $|\eta| < 1.2$, and two Endcap Calorimeters (EC) that cover the range $1.4 < |\eta| < 5.2$. Fig. 3.9 shows a cut out view of the DØ Calorimeter. Each cryostat weighs about 300 metric tons and is filled with about 15,000 liters of liquid argon. The calorimeters are segmented into three different regions, an electromagnetic (EM) region closest to the tracking system to detect electrons and photons, followed by a fine hadronic (FH) region and coarse hadronic (CH) region to detect jets. There are a totla of 55,296 calorimeter readout channels. Fig. 3.10 shows the geometry of the calorimeter in greater detail in the $r - z$ plane.

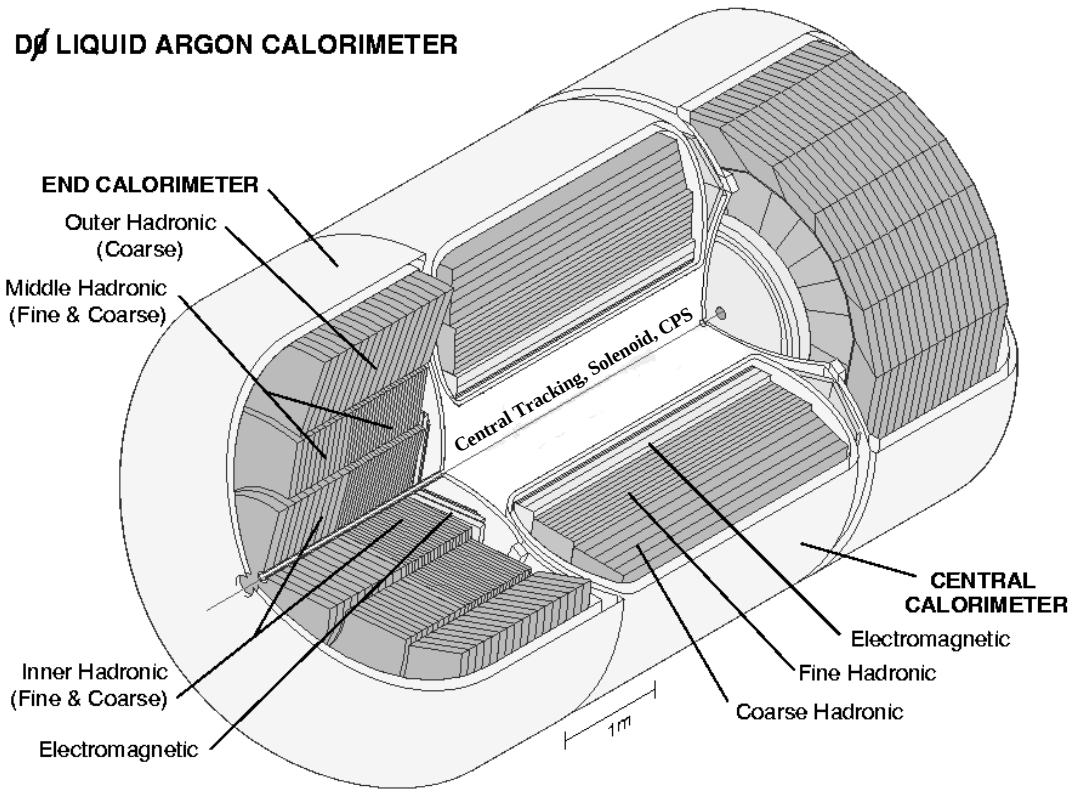

Figure 3.9: The DØ calorimeter.

The EM and FH sections use uranium absorber plates, while the CH section uses either copper absorber plates (CC) or steel absorber plates (EC). The absorber plates can initiate particle showers by creating low energy secondary particles. The liquid argon is the active medium used to sample the ionization. It gives a measure of the shower energy from the ionization of the charged secondary particles.

High energy electrons and photons lose their energy in the calorimeter through ionization and *bremsstrahlung* (braking radiation). Strong interactions between hadronic particles and the nuclei of the absorbing layers produce pions and nucleons which further collide inelastically with other nuclei. This results in a hadron shower. The electromagnetic section of the calorimeter represents $\approx$ 20 radiation lengths. Most of the energy from electromagnetic showers is therefore contained within the electromagnetic section of the calorimeter. The characteristic length scale of hadronic showers being much longer then

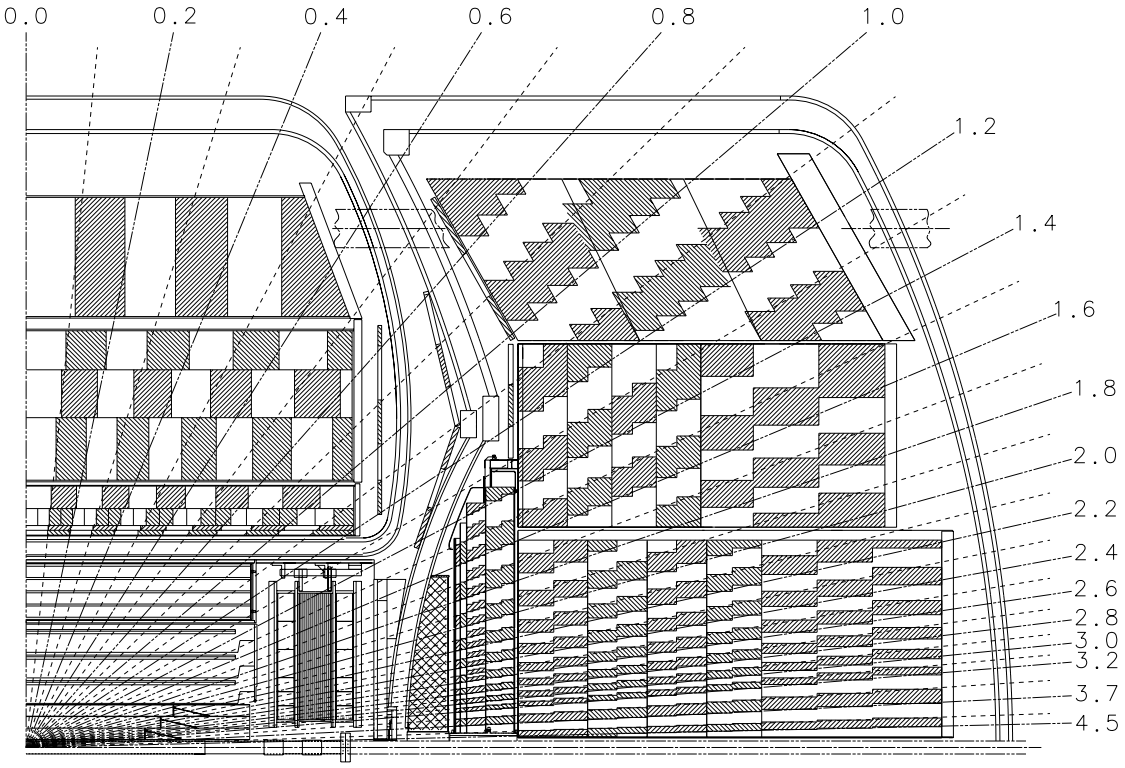

Figure 3.10: A schematic view showing the transverse and longitudinal segmentation pattern of a section of the DØ calorimeter. The lines and numbers indicate pseudorapidity intervals from the center of the detector.

electromagnetic showers, hadrons deposit a large fraction of their energy in the hadronic calorimeter.

Neutrinos pass right through the calorimeter without interacting with the material and can only be indirectly measured as the imbalance of transverse energy in an event. Muons deposit only a small fraction of their energy in the calorimeter and require an additional detector for identification.

The calorimeter remains unchanged from Run I but the readout and trigger electronics have been fully replaced to allow a faster readout in Run II. This was necessary to accommodate the reduced bunch spacing of the Tevatron in Run II. Beam crossings every 396 ns provide a challenge for the signal charge integration because charge from a previous event is still being collected as additional events occur. Pre-amplifiers and baseline subtracter (BLS) boards were replaced in Run II. Calorimeter channels are sampled before and after

a collision. The amount of energy measured before the beam crossing gives the "baseline" and this value is used for baseline subtraction after the collision.

3.6 The Intercryostat Detector

The Intercryostat Detector (ICD) helps to measure the energy of jets and missing transverse energy in between the endcap and central cryostats in the region $1.1 < |\eta| < 1.4$. This region contains a large amount of uninstrumented material like cryostat walls, support structures and cabling which leads to a degradation of energy measurement. The ICD partly restores the energy measurement in this region by providing an additional sampling. The ICD uses 384 scintillation tiles of size 0.1 x 0.1 in $\Delta\eta$ x $\Delta\phi$ to match the calorimeter cell size. These tiles are mounted on the inner face of the EC cryostat walls. Wavelength shifting (WLS) fibers in the grooves of each tile are mated to clear fiber ribbon cables to bring the light signals from the ICD tile's module connector to the readout crates. The readout crates contain phototubes and readout electronics to digitize the PMT signal.

3.7 The Muon Detector

The muon detector is the outermost detector subsystem and surrounds the calorimeter. It was designed exclusively to detect muons which are the only particles (besides neutrinos) that emerge through the calorimeter. Muons produced at DØ are minimum ionizing particles (MIP). They deposit only a small amount of energy in the calorimeter and the central tracker and rarely shower. The muon detector is a spectrometer composed of the central muon system, the forward muon system and a 2 Tesla toroidal iron magnet. The muon system has three layers which contain scintillation counters for triggering and wire chambers for coordinate measurements. One of the layers, the A layer, lies inside the toroid while the other two layers, the B and the C layers, lie outside the toroid. The central muon system has proportional drift tubes (PDTs) which are the same as in Run I and cover the region $|\eta| \approx 1.0$. The forward muon system extends the muon coverage to $|\eta| \approx 2.0$. It includes three layers of mini drift tubes (MDTs), trigger scintillation counters and improved shielding around the beam pipe. Fig. 3.11 shows a cut away of the muon detector.

The Run I muon detector had a cosmic cap which consisted of scintillation counters installed on the outside of the central muon PDTs. In Run II, this coverage was extended to

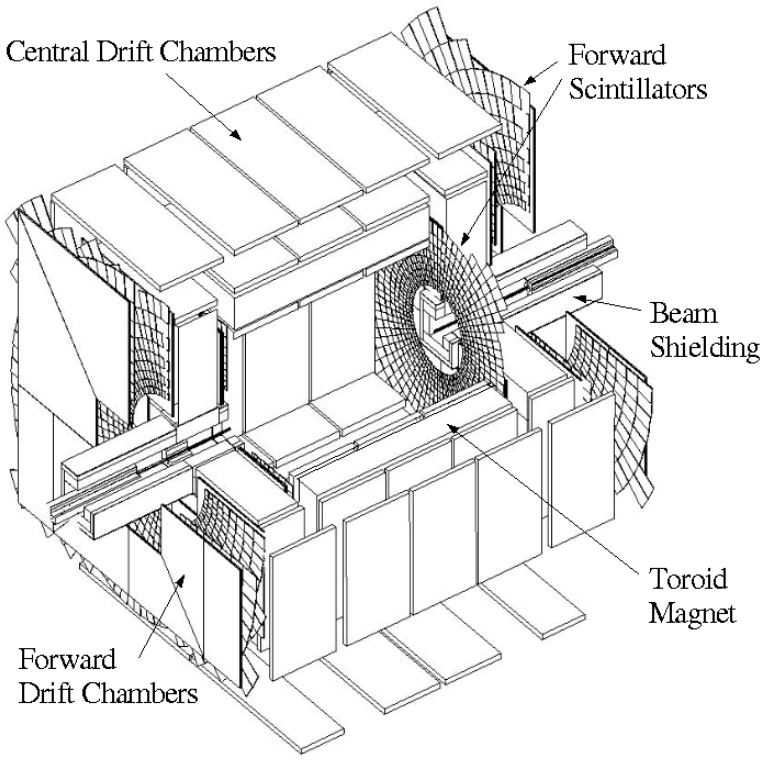

Figure 3.11: A cut away three dimensional view of the muon detector.

the lower sides and the bottom of the detector. These trigger scintillation counters reduce the cosmic ray background by associating muons with the appropriate bunch crossing.

The toroid magnet which is 109 cm thick and weighs 1973 metric tons, adds additional interaction lengths to the material and is used to make an independent measurement of the muon momentum. This is useful because

- it allows the Level 1 muon trigger to use a low p_T cutoff,
- it allows for a cleaner matching of the muon to a central track,
- it rejects π/K decays and
- it helps improve the momentum resolution of high p_T muons

The muon momentum is, however, primarily measured using the central tracker. The polarity of the toroid magnet is regularly reversed during data collection.

Table 3.1: Parameters of the Muon Drift Tubes.

Parameter	Proportional Drift Tubes	Mini Drift Tubes
Wire Step	130 mm	10 mm
Tube Wall Thickness	0.6 mm	0.6 mm
Tube Material	Extruded Al	Al, Stainless Steel
Wire Material	W-Au (96% : 4%)	W-Au (96% : 4%)
Wire Diameter	50 μm	50 μm
Gas Material	84% Ar, 8% CH_4, 8% CF_4	10% CH_4, 90% CF_4
Gas Gain	1.1×10^5	2×10^5
Cathode Potential	+2300 V	-3200 V
Maximum Drift Time	500 ns	60 ns
Wire Potential	4700 V	0
Drift Speed	10 cm/μs	25 cm/μs

3.7.1 Drift Tubes

The drift tubes are rectangular gas filled volumes with a sense wire strung taut through the center of the volume. Charged particles which pass through the volume ionize the gas and produce electrons and ions. The wire in the center of the chamber is kept at a positive voltage with respect to the walls of the tube. This causes the electrons to move towards the sense wire. As the electrons accelerate towards the wire, they gain energy and cause further ionization. This produces an avalanche of electrons which amplifies the signal.

The central drift tubes are 5.5 cm $\times$ 10.0 cm in cross-section and 240 cm in length. The forward drift tubes are much smaller having a cross section of 1.0 cm $\times$ 1.0 cm with varying lengths. Table 3.7.1 gives an overview of some of the more important drift tube parameters. The drift tubes are arranged such that the sense wire is parallel to the magnetic field and perpendicular to the particle's trajectory. By calibrating the drift time of the signal to the sense wire, a measurement of the arrival time of the pulse translates to a measurement of the radial distance of the particle from the wire. Fig. 3.12 shows an exploded view of the wire chambers of the muon detector.

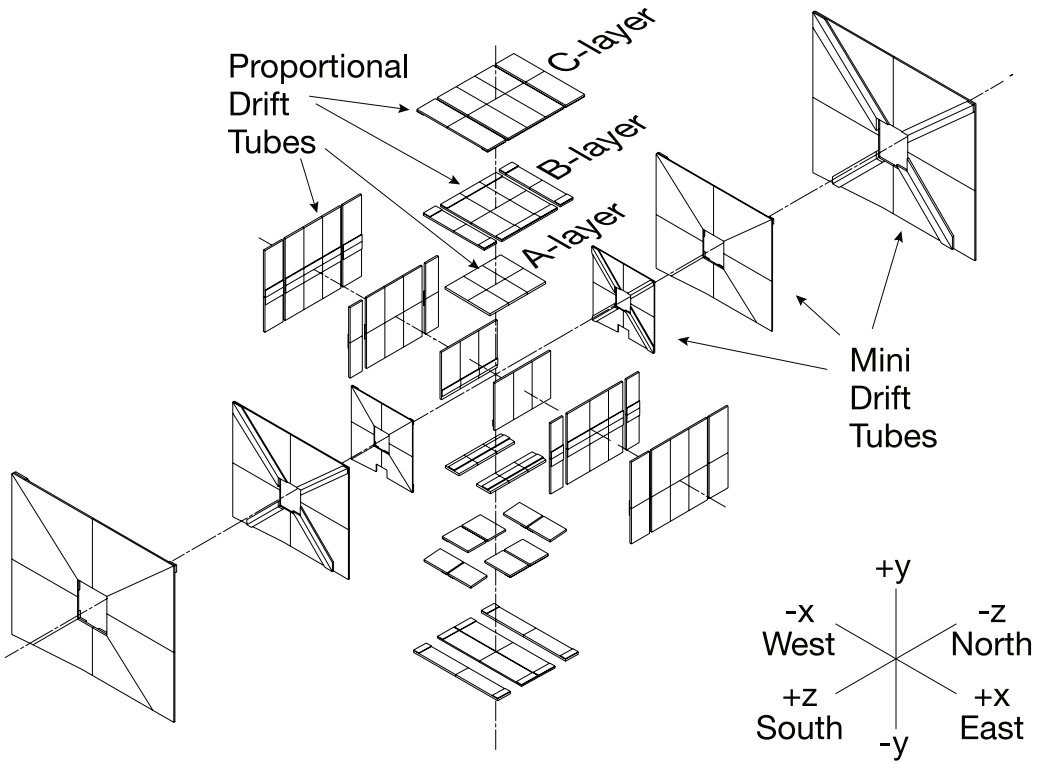

Figure 3.12: An exploded view of the muon wire chambers.

3.7.2 Scintillators

Layers of scintillation counters aid in muon identification and are used for triggering events that contain muons. The detectors in the forward region are trapezoidal sheets of scintillator with a ϕ segmentation of $\approx$ 4.5°. Rectangular counters with similar ϕ segmentation comprise the two scintillating layers in the central region. Photo-multipliers are mounted on the detector which collect the light and convert the signal to an electrical pulse for readout. Fig. 3.13 shows an exploded view of the scintillation counters of the muon detector.

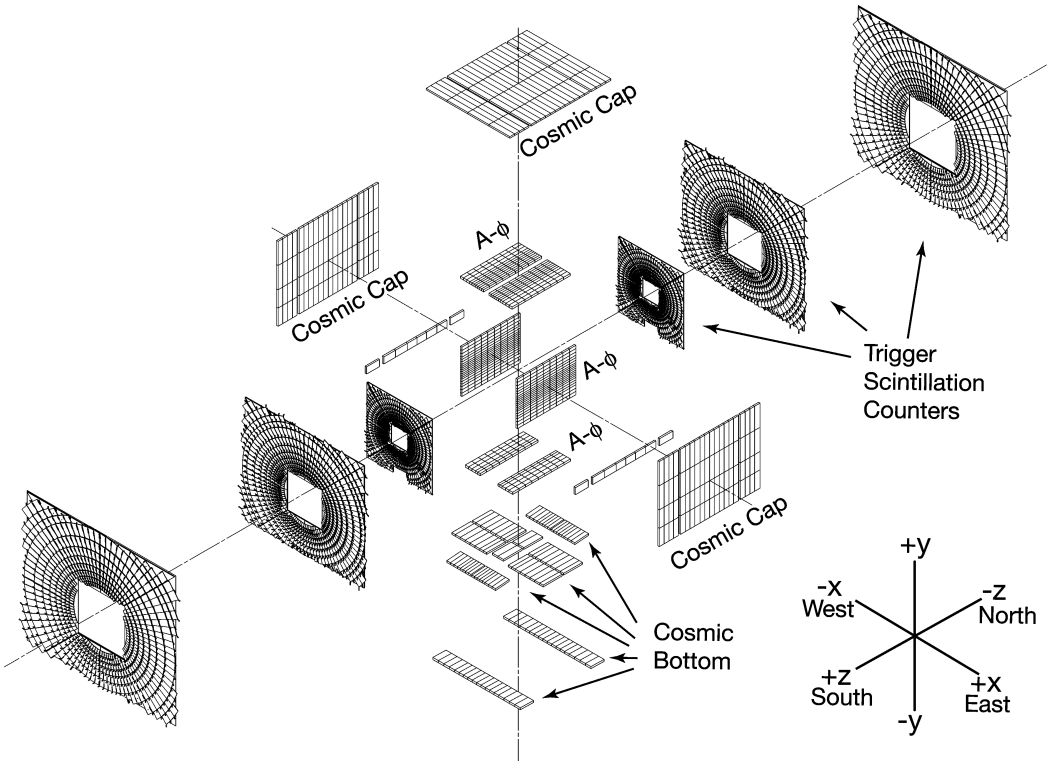

Figure 3.13: An exploded view of the muon scintillation counters.

3.8 Triggers

The Tevatron provides $p\bar{p}$ collisions at a rate of 2.5 MHz where most of the events are due to inelastic scattering. To select and record the more interesting events which occur at much smaller rates, DØ uses a three level, pipelined trigger system which gradually reduces the collision rate to a maximum of 50 Hz to be recorded to tape. The three levels are referred to as Levels 1, 2, and 3 (L1, L2, L3). L1 decisions are hardaware based, L2 uses a combination of hardware and software while L3 is based purely on software. Figure 3.14 shows an overview of the first two trigger levels with the specified design rates of each level.

In addition, there is a L0 trigger [44] that is used to make an accurate luminosity measurement from non-diffractive inelastic collisions. The L0 detector has two arrays of twenty-four plastic scintillation counters which are on the inside face of the Endcap Calorimeters and cover the range $2.7 < |\eta| < 4.4$. The L0 trigger can also be used to determine the z position of the event vertex by calculating the difference in arrival time

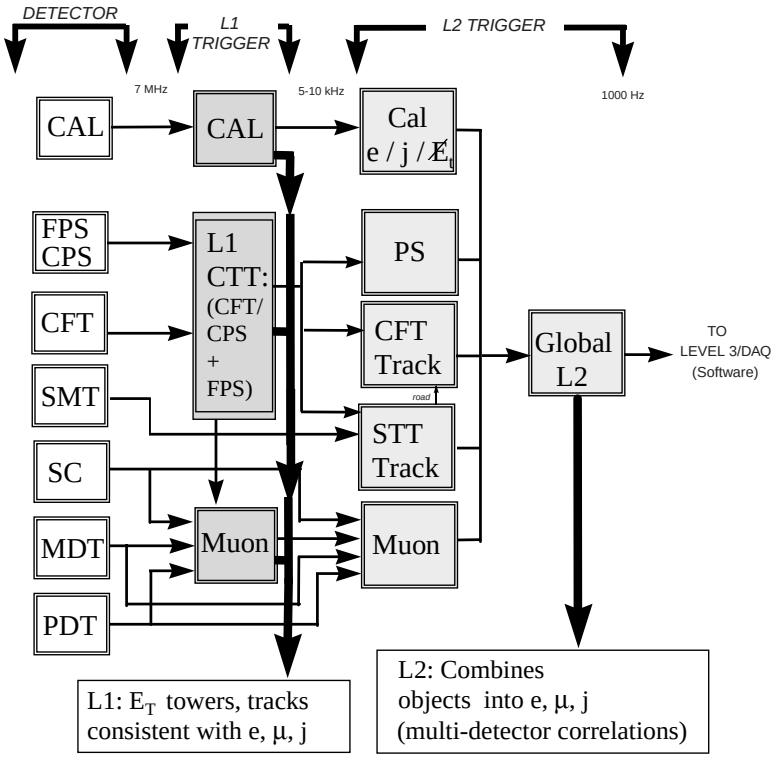

Figure 3.14: Level 1 and 2 Trigger Architecture. The information flow is indicated by the horizontal arrows.

for particles hitting the two L0 detectors. This information can then be used by the other trigger levels.

3.8.1 Level 1 Triggers

The L1 triggers are designed for fast triggering and reduce the rate from 2.5 MHz to ≈ 7.5 MHZ. The L1 triggers are based upon isolated detector elements like tracking, calorimeter, and muon. The exception is the muon trigger which also accepts inputs from the L1 track trigger. Each of the L1 trigger elements report their findings to the L1 Framework (L1FW) upon each beam crossing. The L1FW is responsible for collecting the information from each of the L1 trigger elements and making the global decision to accept or reject the event. In order to ensure that the L1 trigger is dead-timeless, each front-end digitizing crate has sufficient memory to buffer 32 events. The L1 system can support 128 separate L1 triggers or trigger bits. Each bit is pre-programmed to require a specific combination of trigger terms.

These trigger bits are determined by custom hardware and firmware implemented in a series of field programmable gate arrays (FPGAs). If the L1FW issues an accept, the event data is digitized and moved into a series of 16 event buffers to be analyzed by L2.

L1 Muon Triggers

At Level 1, the muon system has trigger terms consisting of scintillator and wire hits in each region and octant. The scintillator trigger can consist of an in-time hit in only one scintillator paddle, or a coincidence of scintillator hits in a road. Wire hits in the A-layer are likewise made up of roads based on the probable trajectories (from Monte Carlo) that a muon might travel leaving the interaction region. The muon trigger can also receive tracks from the fiber tracker in time to make a decision at Level 1. Otherwise, the only momentum measurement possible for Level 1 muon is if a coincidence of scintillators inside and outside the toroid is required, which implicitly requires that the muon have been of at least 3 GeV/c in transverse momentum.

(In the bottom of the detector, there is less scintillator coverage than in all of the other regions. Triggers requiring a scintillator coincidence will not fire when a muon passes through this area of the detector. This area is known as the 'hole', and exists because of the physical support necessary for the calorimeter. In the analysis, an area of $\eta_{detector} - \phi$ is defined so that this may be removed from the acceptance. This area is defined as being within $|\eta_{detector}| < 1.0$ and in $4.25 < \phi < 5.15$. Muons can still be reconstructed offline within this region, but will not fire the trigger.)

L1 Track Triggers

The central tracking trigger (CTT) is based upon recognition of hit patterns in the axial fibers in the central fiber tracker (CFT). As the ϕ segmentation of the CFT is 4.5°, there are eighty trigger sectors for the CFT. The digitized signals from all fibers are fed into VME cards with FPGAs that search for tracks via pre-programmed look up tables (LUTs). This is accomplished by considering different possible fiber hit patterns. The patterns that are consistent with particle tracks are programmed into the LUTs. If these hit patterns are seen in data, they generate a track candidate. Each track candidate is identified by its trigger sector, relative ϕ within a trigger sector, momentum, and direction of curvature. Although currently unused, the system also can hold information from corresponding hits in the pre-

shower detectors. These L1 track candidates are organized by further hardware to take part in the global L1 trigger decision, along with being passed to the muon trigger and silicon track trigger (STT).

3.8.2 Level 2 Triggers

The L2 trigger is designed to reduce the event rate by up to a factor of 10 to $\approx$ 5-10 kHz. This is done using a subsystem preprocessing and a final L2 global processor. Data from each of the sub-detectors is examined in greater detail to gather more precise information about the event. Then information from the entire detector is combined so that triggers can make use of the information from multiple detector elements. Except for one trigger, the STT, the processing is almost entirely carried out by software in the processor boards, using information from the L1 triggers. The calorimeter preprocessor, L2CAL, collects information from L1CAL and builds jet and electron candidates using clustering algorithms. Here, the preprocessors calculate the position and energy, and test them for shape and transverse energy requirements. The L2CTT sorts the list of L1CTT tracks according to p_T. The muon preprocessor improves muon identification by calculating the transverse momentum, rapidity, azimuthal angle, and 'quality' of the muon candidate.

The L2 Muon Trigger

In the muon system, pre-processed information from the readout is assembled into stubs in each of the different layers. Look-up tables provide a p_T measurement for those muon tracks that have hits inside and outside of the toroid. Based on the number of hits and the position of the track in the detector, the muon is assigned a 'quality'.

The Silicon Track Trigger

The silicon track trigger (STT) was designed for online track reconstruction using data from the silicon micro-strip detector (SMT) and tracks reconstructed in the Central fiber tracker at Level 1 [45] (L1CTT). L1CTT track candidates are used to define projective 'roads' inside the silicon. Only those axial cluster of strips from the SMT, which are within roads of ± 2 mm are associated with the CTT track candidates. The SMT detectors are arranged into 12 sectors of 30° in ϕ and the STT treats the tracks in the twelve sectors independently.

Unlike the rest of the L2 trigger system, there is no L1 trigger component which utilizes the silicon detector. The STT must therefore receive and process digitized data from all of the silicon detectors which are used in the trigger. The STT fits the tracks selected by the L1CTT with the information from the silicon tracker to obtain more detailed information of the tracks at the trigger level.

Data is received from the L1CTT and SMT detectors via optical fibers which plug into custom receiver cards located in the rear card cage of the crate housing the trigger electronics. The data is processed by FPGAs and DSPs on the logic daughter boards. The STT uses three custom built electronic boards called the Fiber Road Card (FRC), the Silicon Trigger Card (STC), and the Track Fit Card (TFC). Each of these modules is designed to plug into a common motherboard for use in a standard VME crate. Data communication between the three modules is achieved via custom mezzanine cards which use Low Voltage Differential Signal (LVDS) cables to transfer data between the cards. Each board also communicates with a common daughter board that buffers and manages the readout of the data to the data acquisition system. The daughter boards communicate with the buffer readout, the link boards, and the VME backplane via three PCI buses. One STT crate processes data for two 30° sectors (there are six STT crates). Fig. 3.15 shows a schematic diagram of an STT crate.

Fiber Road Card

The Fiber Road Card (FRC) consists of the road receiver, the trigger receiver, the road data formatter, and the buffer manager. The road receiver accepts data via optical cables from the L1CTT. It receives trigger information from the framework via a mezzanine card. The road data formatter reformats the CTT data and distributes roads and trigger signals to the other daughter boards via the LVDS link cards. The buffer manager handles the readout to the data acquisition system (DAQ). Upon every L1 accept, data is received and processed by all daughter cards. Data for readout is transfered to the buffer card for each event the system receives. If a L2 accept is issued the buffer manager sends control signals to the buffer cards which prepare the data for readout to the DAQ. There is only one FRC per crate.

Silicon Trigger Card

The STT receives the digitized output of the silicon detector directly and processes data

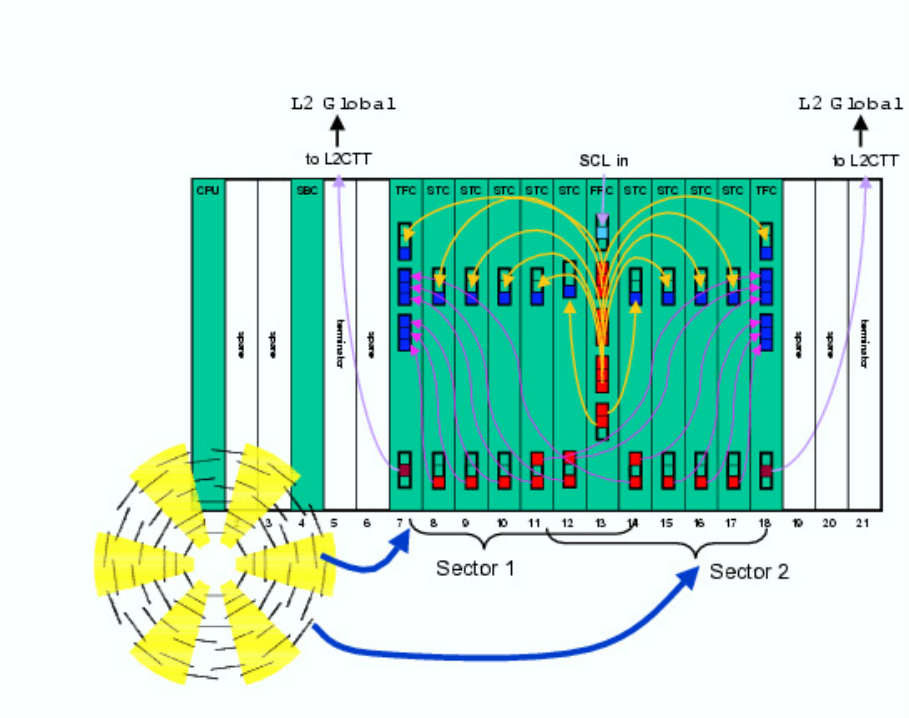

Figure 3.15: A schematic diagram of an STT crate.

from the axial Silicon strips. There are nine STCs per crate and each processes the data from eight detectors. Using downloaded Look up tables (LUTs) the STCs mask out noisy and dead silicon strips and perform a strip by strip gain and offset correction. The STCs also apply a fast clustering algorithm on the data where a cluster is allowed to start if the strip is above a certain threshold. Another simple algorithm is used to calculate a cluster centroid. The cluster centroid is then matched to a L1CTT track using LUTs. If the cluster centroid is within $\pm$ 2 mm of a CTT track it is kept, otherwise it is discarded. A cluster centroid can be associated with multiple CTT tracks. The information is then transfered to the Track Fit Card.

Track Fit Card

The Track Fit Card (TFC) receives L1CTT tracks over a serial data link from the FRC and the centroids of silicon clusters associated with those tracks from the STCs. There are two TFCs per crate to fit tracks in 30° sectors using both the CTT track information and the

SMT hits information to get more precise track parameters. The results are transfered to a preprocessor to be combined with the tracks from the other crates and sorted before being transfered to L2 global. Information is prepared for readout to the data acquisition system for monitoring the track fitting performance. Information about the beam spot (which is measured by on-line tracking) is downloaded to the TFC. A correction for the beam position offset is used in the final hit selection in the TFC and to correct the impact parameter.

The STT Examine

One of the tools used to monitor the performance of the STT is a real-time online tool known as the Examine. This makes use of a software package which unpacks the data coming out of the STT and plots histograms of various parameters for the different cards and crates utilized by the STT. Global parameters like the p_T and impact parameter b of the tracks are also plotted to check for hardware and firmware performance.

3.8.3 Level 3 Triggers and Data Aquisition System

At Level 3 the events from the detector undergo a fast reconstruction, similar to the full reconstruction that is carried out offline. The full detector information is available, including hits from the trackers, the full calorimeter precision readout, and muon system information. Generally, a Level 3 trigger fires if an object of the required type is reconstructed, such as a track above 10 GeV/c (using the entire tracker, silicon detector and fiber tracker), or a calorimeter cluster greater than 5 GeV (using the cell level readout information).

Upon a L2 accept, the data for that event is transfered out of each of the readout crates. A program (the L3 supervisor) monitors the performance and event buffers of the individual L3 computer nodes and decides which node each event will be sent to. The L3 nodes make use of an event builder (which is told by the L3 supervisor which readout crates to expect data from) and an event filter (which runs the event reconstruction and compares the event to a list of filters, each of which place different requirements on the event.) If the event builder does not get a full event from each crate, the event is discarded. If the event passes any of the event filters, the event is accepted and written to tape for offline analysis. Level 3 algorithms are designed to make decisions within 100 ms. L3 has an output bandwidth of approximately 50 Hz.

CHAPTER 4

Event Reconstruction

After a $p\bar{p}$ interaction, events that pass the DØ trigger filter are recorded to tape as digitized signals in the form of pulse heights, widths, and times. This is data in the raw format and it needs to be translated into something more tangible before it can be used for analyis. Offline reconstruction programs written in C++ unpack the digitized signals from each of the sub-detectors and interpret the information to form physical objects like tracks, calorimeter clusters and muons. Described below is the process of reconstructing various objects from the raw data. We concentrate on the reconstruction of only those objects most relevant to this analysis have been described more thoroughly.

4.1 Central Tracks

Track reconstruction begins with finding hits in the SMT and CFT detectors. Starting from hits in the innermost layer of the tracker and working towards the outermost layer, the tracking algorithm [46] creates a pool of track hypotheses. These are ordered according to well defined criteria and filtered to select the best possible track from the pool.

When a charged particle passes through a layer of the central tracker, the SMT and CFT detector electronics translate this information to a hit in the tracker. Initial tracks are made up of hits in at least three layers of the SMT. The first hit could be in any of the layers of the barrels or F-disks. The second hit has to be selected from an adjacent layer if $|\Delta\phi| < 0.08$ rad as viewed from the beam spot. The third hit is selected from the subsequent layer provided that

- the radius of curvature of the circle constructed by the track hypothesis > 30 cm (i.e. $p_T > 180$ MeV),

- the impact parameter of the track wrt the beam spot < 2.5 cm.
- the χ^2 of the fit < 16.

Fig. 4.1 shows the idea of a track hypothesis. Each track hypothesis is extrapolated to the next layer of the SMT or the CFT if the match to the fit track has a $\chi^2 < 16$. If there are multiple hits in any given layer, multiple hypotheses are constructed and each one is investigated separately. Any layer without a hit to match to the track hypothesis is termed a miss. The number of layers with missed hits is monitored, allowing for dead or disabled channels. There are three classes of misses which are defined as

Inside Misses: missed hits between the innermost and outermost hits on the track.

Forward Misses: missed hits after the outermost hit on the track.

Backward Misses: missed hits before the innermost hit on the track.

Forward and backward misses are collectively referred to as outside misses. If there are three continuous misses, the hypothesis is discarded. Otherwise, construction of the track hypothesis continues till the last layer of the tracker is reached. The track hypotheses are filtered down according to

1. Hits in at least four detectors of the SMT and CFT, including both axial and stereo hits.
2. No more than three inside misses with no more than two of those misses within the SMT
3. No more than six outside misses.
4. $N_{hits}/5 \geq N_{misses}$.
5. Seperate track hypotheses are allowed to share axial hits given that
   - $N_{shared} \leq (2/3) \times N_{total}$.
   - $N_{shared} \leq (1/5) \times N_{total}$ or $N_{total} - N_{shared} > 3$.

Hypotheses are then sorted according to

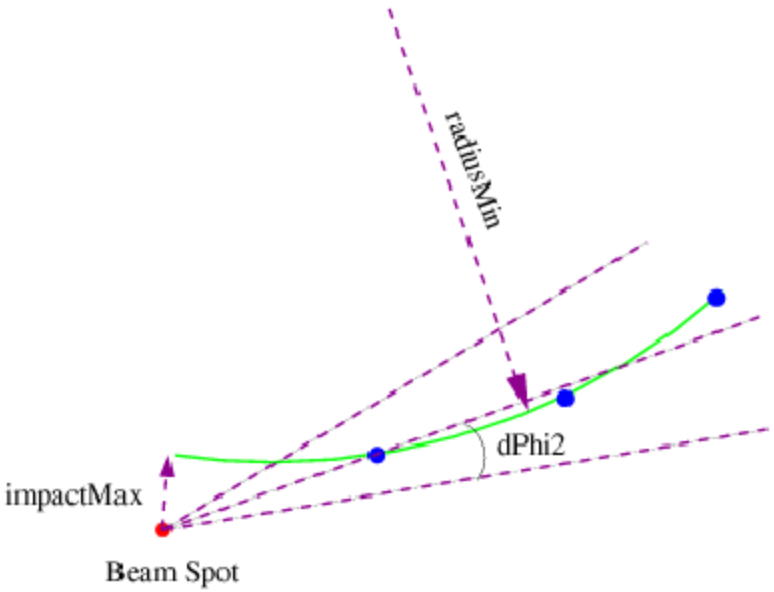

Figure 4.1: Tracking hypothesis based on fitting 3 hits to start a track. The points in blue represent hits in the detector layers.

- Largest number of hits.
- Smallest number of misses in case of same number of hits.
- Smallest χ^2 of track fit in case of same number of misses.

In order to further reduce false tracks, the position of vertices is next determined using the reconstructed tracks and the beam spot position (to within 0.1 cm in z and 0.2 in DCA of each other). Vertices are required to have at least five tracks with $\chi^2 < 36$. The tracks that are consistent with one of the vertices are assigned two additional hits. Using this information, the tracks are re-sorted and filtered as before. Since the track ordering controls which hits are considered shared, previously accepted tracks may be rejected as a result.

Tracks that do not have any hits in the silicon layers may be reconstructed within the fiber tracker but only if they are consistent with a vertex position. This reduces the combinatoric background which is much worse than in the SMT because the CFT does not have any segmentation in z. Using the vertex position provides an improvement in the p_T resolution

of the fiber tracker for CFT only tracks. Finally, a last refitting is performed over all the remaining track hypotheses from which the track parameters η, ϕ and curvature q/p_T can be extracted.

In some cases, pions or kaons decay to muons within the central tracker causing a 'kink' in the track of the particle. This may lead to the central track being reconstructed as a CFT only, high p_T track. This process is known as an in-flight decay. To reduce the backgrounds from in-flight decays, CFT only tracks are not used in this analysis.

4.1.1 Primary Vertex

The primary vertex is the location of the hard scattering interaction. Reconstructing the primary vertex is important in order to properly calculate transverse energies in the calorimeter and hence the $\not\!\!E_T$. Reconstructing the location of the primary vertex is done by examining the tracks found in the event. The reconstruction is done in three steps [47] which include

- track selection
- vertex finding
- vertex selection

The track selection is designed to find the tracks that most likely come from the primary vertex. Tracks with large impact parameter are typically produced by secondary particles which decay after they are produced in the hard scattering event and travel a small distance. Therefore, the tracks from which the primary vertices are reconstructed are required to have a small transverse impact parameter. Tracks are required to have clusters in two or more of the silicon layers, $p_T > 0.5$ GeV and a transverse impact parameter significance $(b/\sigma_b) < 3.0$. (b is the distance of closest approach and has an uncertainty of σ_b).

In order to separate tracks that come from different interactions, the tracks are clustered together in the z direction. Tracks that are within 2.0 cm of each other are clustered together. The tracks in each of the z clusters are then fit to vertices using the Kalman Filter algorithm. This algorithm relies on a fast, least squares fit approach. Using the track parameters $z, \phi, tan(\lambda), b$ and the curvature q/p_T as well as vertex parameters and the momentum of tracks associated with the vertex, the χ^2 of the fit is minimized [48].

As a first pass, candidate tracks associated with the vertices are required to pass a loose selection cut of $(b/\sigma_b) < 100$ with respect to the center of the detector in (x,y). In the second pass, only those tracks with $(b/\sigma_b) < 3$ are selected where b is now the distance of closest approach with respect to a vertex from the beam spot position, using the list of vertices in the first pass.

There now results a list of several vertices which could have originated from the hard scattering interaction point. An algorithm selects the vertex which has the least probability of having originated from a 'minimum bias' interaction [49]. A minimum bias interaction is a low momentum transfer interaction between a proton and an anti-proton also known as inelastic scattering where the hadrons do not break up.

For each track with $p_T > 0.5$ GeV attached to the vertex, a probability for the track to have come from a minimum bias event is assigned based on $log_{10}p_T$. Since higher p_T tracks are less likely to come from a minimum bias interaction, this probability is evaluated by studying the $log_{10}p_T$ spectrum obtained from Monte Carlo. The vertex with the smallest probability of originating from a minimum bias interaction is then taken to be the location of the hard scattering event.

4.2 Muons

Muons generate tracks in the central tracker and as minimum ionizing particles, deposit a small amount of energy in the calorimeter. But a muon is really identified as a muon by hits in the muon detector. The muon system is made up of drift tubes and scintillators. Drift tubes measure the position of the muon in the detector while the scintillators also provide timing information. Muon reconstruction involves finding hits in the muon system, combining the hits to make segments and using the segments to fit to a track. A track in the muon detector is called a local muon. A local muon matched to a central track is termed a global muon.

There are several sources of backgrounds when reconstructing muons. There can be real muons from cosmic rays. There can also be real muons from the scattering of protons off the beam pipe or magnets further down the Tevatron tunnel. These muons do not originate from the $p\bar{p}$ interaction region. The ceiling of the collision hall which has been exposed to beam losses from the Tevatron is radioactive and bombards the outer chambers with low energy photons. The calorimeter which is made of depleted uranium, gives off secondary

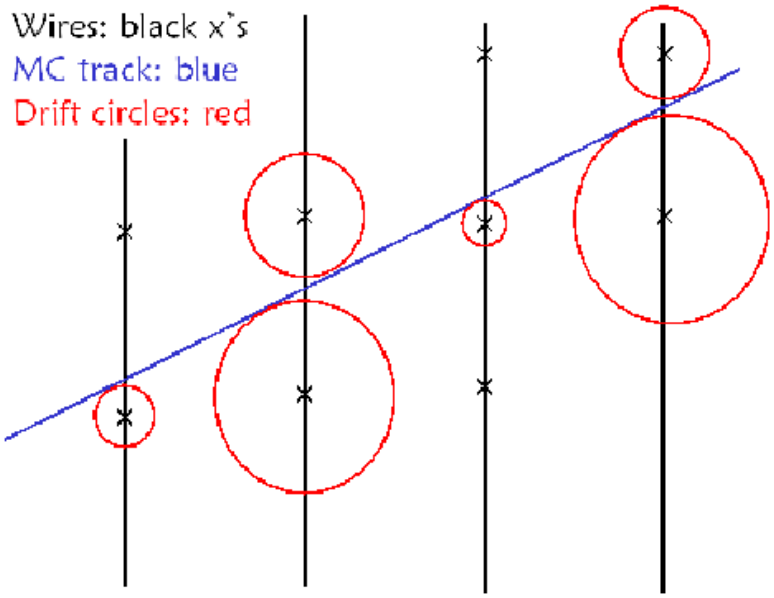

Figure 4.2: Segment reconstruction in the drift plane.

particles leading to backgrounds in the innermost chambers. The scintillator detectors in the muon chambers provide timing information with respect to the beam crossing and this is used to largely reduce both the physics and the instrumental backgrounds.

Hits: Hits are identified using information from the drift tubes and the scintillators. The PDTs measure the drift times and the axial times. The drift time is the time it takes the electron cloud to reach the sense wire while the axial time is the time it takes the signal to be collected from the wire. The distance from the sense wire is measured using the relationship between the drift time and the drift distance. In the case of MDTs where the measured time is the sum of the drift and axial time, the hit is taken to be in the center of the MDT.

Segments: The muon system has three layers of scintillators and drift tubes. Each of these layers has several sublayers to be able to better measure the position of the muon. The sublayers also increases the probability of detecting a muon. The reconstructed path of the muon in each layer is called a segment. Reconstructing segments involves several steps [50]. Fig. 4.2 shows the idea of segment reconstruction.

1. Links between the hits are formed when the hits are within 20 cm of each other, not in the same plane, and not from the same underlying wire hit. The location and direction of the resulting segment is calculated. Due to the large size of the drift tubes in the central region, the position of the hits in the segment depends on the angle of the segment. After the segment direction is calculated, the hit positions are recalculated relative to the segment position. Finally, the segment direction is recalculated according to the new hit positions.

2. The local segments are linked to form larger segments. The position and the direction of the segments are examined and if the pair forms a straight line, the two are merged into a larger segment.

3. The segement is lined up with the vertex when the segments in the A layer which lies before the muon toroid, have the direction in the drift plane set to be the same as the direction of a line from the origin to the position of the segment.

4. Matching B and C segments is then attempted to make larger segments with more precise information. Since there is no magnetic field between the B and C layers the particle should travel in a straight line.

5. Segment Filtering is the final step. A χ^2 is calculated for each possible segment assuming a straight line path. The segment with the lowest χ^2 in each octant is kept.

After segments have been found, these segments are linked together and a track fit in the muon system is attempted. The track fitting consists of local track fitting and matching to tracks from the central tracker. Segments from the A layer and segments from the B and C layers are fit to find a local muon track. The procedure takes into account the bending of the trajectory by the toroid field and the energy loss as the muon passes through the iron of the toroid [51]. The track is propagated step by step from the center of gravity of the BC layer to that of the A layer using circular helices. The result is a local muon track parameterized by the position and momentum at the A layer. The next step is to match the track with a track from the central tracker. The matching procedure takes into account the magnetic fields (solenoid and toroid) and multiple Coulomb scattering and energy loss in the toroid

and the calorimeter by using the error matrix propagation [52]. The matching is performed and the distance of closest approach to the beam is computed.

4.2.1 Muon to Track Matching

If two or more segments have successfully been fit into a muon track (meaning the fit to segments inside and outside the toroid has converged), then the Muon-to-Central "Saclay" match will be attempted. Using the position, momentum, and associated errors on each, the error matrix for the measured muon track may be calculated:

$$E_{6x6} = \begin{pmatrix} E^{PP}_{3x3} & E^{PX}_{3x3} \\ \\ E^{XP}_{3x3} & E^{XX}_{3x3} \end{pmatrix}.$$

Here, E^{PP} is the error matrix for the momentum defined as $E^{PP} =< \delta p^T(\delta p) >$, where δ stands for the difference with respect to the mean value $\delta p = p - < p >$. Using the errors from the muon system track, and the like errors from the central tracker parameters, it has been shown that the final combined muon-central tracker parameters and errors may be found [52].

If the muon system reconstruction did not produce a converged fit then tracks from the central tracking volume are propagated to the A-layer of the muon system. Only tracks of greater than 2 GeV in momentum are used in this propagation. All tracks within $\Delta\phi < 1$ and $\Delta\theta < 1$ are associated with the muon, but only the best (meaning the closest) is selected as the proper track to associate with the muon. Using the same method as previously cited, only beginning with the central track instead of the muon, the parameters are propagated to the A-layer of the muon system. In this case no attempt is made to merge the local track fit and the fit from the central track and the central tracker momentum is used.

4.2.2 Muon identification

Muons can be identified in the DØ detector using three independent sub-detectors: the muon detector system, the central tracking system, and the calorimeter. The muon detector system provides the most unambiguous way of identifying muons covering about 90% of the angular acceptance up to psuedo-rapidity $|\eta| < 2$. The loss in acceptance is mostly due missing detector coverage below the detector (see chapter 3). The central tracking system

is highly efficient in finding tracks from charged particles in the entire region of the muon detector. Due to multiple scattering in the toroids, there is better position resolution of the hits in the central tracker and hence a more precise momentum measurement. For this reason, the momentum of the muon is measured from the central track matched to the local muon track. Finally, since muons are minimum ionizing particles in the calorimeter they also deposit a small amount of energy in the calorimeter The efficiency of identifying muons with only calorimeter information is $\approx 50\%$ and far less efficient than other muon signatures.

Muons are required to have:

- at least two A layer wire hits.
- at least one A layer scintillator hit.
- at least two BC layer wire hits. [1]
- at least one BC scintillator hit.
- the time from the beam crossing to the scintillator hit within 10 ns for the A layer and 15 ns for the BC layers.
- $\frac{\chi^2_{track}}{D.O.F.} < 4$ for the central track fit.
- the distance of closest approach of the track less than three standard deviations from zero.

The requirement on the scintillator hit timing is to further ensure that the muon originated from the hard scattering event [2]. The requirement on the distance to the primary vertex serves two purposes. First it reduces the number of cosmic ray muons which coincidentally pass through the detector. Secondly, it removes background from poorly reconstructed tracks.

[1] Since the B and C layers are after the toriods local muon segments are formed which contain hits in both the B and C layer. These segments are refered to BC segments and hits in the muon system that are part of these local segments are refered to as hits in the 'BC layer.

[2] Muons created in the upper atmosphere (cosmic ray muons) penetrate the DØ detector and are reconstructed by the muon system. They can be removed by requiring that the muon is consistent with coming from the primary vertex both spatially and temporally.

4.3 Calorimeter Clusters

The calorimeter signal consists of the collection of electrons from the ionization of liquid argon. The signal is then digitized and sent through a series of readout electronics. As in the case of the central tracker, the first step is to correct (on a cell by cell basis) the number of ADC counts due to intrinsic differences in cell to cell response and electronic readout. The next step is to convert the ADC counts into an energy deposition in GeV. The calibration comes from both test beam results (where particles of known energy were targeted on portions of the calorimeter [53]) and *in-situ* calibration (reconstructing the invariant mass of particles whose mass is known to much higher precision than the resolution of the calorimeter [54]). After finding the deposition in each cell, the cell energies are summed in towers of equal η and ϕ. While taking this sum, the high energy approximation is made such that the particles are assumed to be massless. In this approximation, the energy and momentum are equivalent such that an 'energy four-vector' may be constructed [54] given by:

$$(E, E\sin\theta\sin\phi, E\sin\theta\cos\phi, E\cos\theta) \tag{4.1}$$

The towers are then assigned direction variables given by:

$$\phi = \tan^{-1}\left(\frac{E_x}{E_y}\right) \text{ and } \theta = \sin^{-1}\left(\frac{\sqrt{E_x^2+E_y^2}}{E_z^2}\right) \tag{4.2}$$

The tower energies and direction are then used in reconstructing the energies and directions of electrons, photons, and jets.

4.3.1 Electrons and Photons

Electrons and photons, collectively referred to as electromagnetic particles exhibit similar behavior in the calorimeter, depositing almost all of their energy in a narrow shower in the electromagnetic layers. Since electrons play only a minor role in the analysis presented in this dissertation and photons are not used at all their reconstruction is only described briefly.

The reconstruction process is similar to the preclustering algorithm used in the first step of the jet finding. Seed towers of 500 MeV are used to find cones with a radius of 0.4. The calorimeter shower is required to be narrow and mostly contained in the electromagnetic layers of the calorimeter. A shower shape χ^2 (calculated using the "H-matrix") is used

to control backgrounds from jets. Since photons do not generally leave any signatures in tracking system the presence of a track match distinguishes electrons from photons. Furthermore a likelihood based on the matched track as well as any additional nearby tracks provides additional suppression of hadronic backgrounds and improves the electron-photon distinction [55].

4.3.2 Neutrinos

Neutrinos mostly pass through the detector without interacting with any of the detector components and as such cannot be detected directly. Using energy and momentum conservation, neutrinos can be measured indirectly as the energy imbalance in each event. Since protons and antiprotons are not point particles, the exact center of mass energy of a $p\bar{p}$ collision at the Tevatron is not known. The longitudinal component of the interaction energy which is along the direction of the beam pipe also cannot be measured. However, the vector sum of the transverse energy of all the particles in the interaction should be zero. Neutrinos are identified as the missing transverse energy or $\not\!\!E_T$ required to vectorially balance the x and y components of the measured energy in the event. Most events will have a small amount of $\not\!\!E_T$ due to noise in the detector parts. Events with real neutrinos usually have a larger value of $\not\!\!E_T$.

The x and y components of $\not\!\!E_T$ are calculated by summing the transverse energy deposited in all calorimeter cells above a threshold of 200 MeV.

$$\not\!\!E_{T_x} = -\sum E_T cos\phi \quad \text{and} \quad \not\!\!E_{T_y} = -\sum E_T sin\phi. \tag{4.3}$$

The total missing transverse energy is then given by

$$\not\!\!E_T = \sqrt{\not\!\!E_{T_x}^2 + \not\!\!E_{T_y}^2}. \tag{4.4}$$

The coarse hadronic part of the calorimeter is significantly more noisy and is not used for calculating $\not\!\!E_T$ unless it is part of a reconstructed jet. To calculate the transverse energy from the scalar energy measured in each cell, the primary vertex that was calculated using tracks is used. For this analysis, the $\not\!\!E_T$ used is corrected for the jet energy scale, the muon momentum and the energy deposited by the muon in the calorimeter.

The $\not\!\!E_T$ distributions can also be used to used to diagnose problems with the calorimeter such as a 'hot' cell or a 'warm region'. This can indicate a problem with the electronics such as a pedestal drift.

4.3.3 Jets

Jets are reconstructed from calorimeter information using the cone algorithm. Towers of size $\Delta\eta \times \Delta\phi = 0.1 \times 0.1$ that have an energy above 1 GeV are used as seeds in preclusters. Preclusters are formed by combining adjacent calorimeter towers within a radius of 0.3 to the seed towers. Jet clusters are defined by preclusters in a cone size $\Delta R = 0.5$ or 0.7 around the jet centroid. Jets with $E_T < 8$ GeV are thrown away. If two jets share the same tower, a split/merge fraction is calculated, which is the ratio of the shared energy of the jets to the energy of the least energetic jet. If the ratio is larger than a 50%, the jets are merged and a new centroid is calculated. Otherwise, the shared towers are split between the jets.

4.3.4 Jet Energy Scale

The measured jet energy from the calorimeter is not equal to the true energy of the parton that initiated the hadron shower. Effects of calorimeter noise, non-uniform energy response, and out-of-cone energy deposition can cause an inaccurate measurement. A Jet Energy Scale (JES) correction is applied to the measured jet energy to correct back to parton-level jet energies. The true jet energy, E_{jet}^{true}, measured with a cone algorithm of radius $\mathcal{R}$, is calculated using the measured jet energy E_{jet}^{meas} by

$$E_{jet}^{true} = \frac{E_{jet}^{meas} - E_O(\mathcal{R}, \eta, \mathcal{L})}{R_{jet}(\mathcal{R}, \eta, E) S(\mathcal{R}, \eta, E)}, \tag{4.5}$$

where

- $E_O(\mathcal{R}, \eta, \mathcal{L})$ is an offset term used to account for detector noise, and energy deposition from the underlying event (i.e. spectator quarks and gluons), from previous $p\bar{p}$ crossings, and from additional $p\bar{p}$ interactions. Since the number of additional interactions depends on the luminosity, the offset term is a function of luminosity $\mathcal{L}$. The offset increases as the cone size $\mathcal{R}$ increases.

- $R_{jet}(\mathcal{R}, \eta_{det}, E_{jet})$ defines the energy response of the calorimeter for jets. This depends on the cone size $\mathcal{R}$ because the cone size determines how much of energy from the calorimeter cluster is included in the measurement.

- $S(\mathcal{R}, \eta, E)$ is the fraction of the jet energy inside the jet cone.

4.4 Jet Energy Scale Corrections

After the standard event reconstruction process, further corrections are applied to jets and to the missing transverse energy. Also, events recorded during periods in which there were problems with some detector subsystems or with the data acquisition system are discarded.

4.4.1 `d0correct`

The software package `d0correct` is used to apply the proper jet and missing transverse energy corrections. It performs the following tasks:

1. Creates a list of good muon candidates ("medium muons"). These are muon candidates which pass a set of standard muon identification requirements.

2. Creates a list of good electromagnetic (EM) clusters. These are EM calorimeter clusters which pass certain p_T, η and isolation requirements taking into account the energy observed in a given layer and its correlations with the energy deposited in the other layers.

3. Creates a list of good jets which takes into account the fraction of the jet energy deposited in the EM part as well as the Coarse Hadronic part of the calorimeter. The ratio of transverse energy of the most energetic tower to that in the next leading tower in the jet, the number of towers in a jet that contain 90% of the jet energy and the total number of towers in the jet are also used in order to suppress fake jets due to noisy cells.

4. Removes the jets that match to the EM clusters. These are highly electromagnetic jets that also appear in the list of EM clusters.

5. Performs jet energy scale corrections. Corrections are made for the effects of calorimeter noise, non-uniform energy response, out-of-cone energy deposition and muons within the jet cone.

6. Corrects $\not\!\!E_T$. Loops over good muons, good EM clusters, and good jets to get the corrected $\not\!\!E_T$ for the event.

4.4.2 `wz_analyze`

After data events have been reconstructed and the Jet Energy Scale corrected using `d0correct`, a software package called `wz_analyze` is used to analyze the events. It creates a storage array called a "ROOT-tuple," which reads over the reconstructed output and makes physics quantities that are useful for analysis. The program also removes runs that have known problems with detector sub-systems or with the data acquisition system.

CHAPTER 5

Event Selection

This analysis describes the charge asymmetry of muons from W boson decays. Consequently, the signal for this analysis is a $W^{\pm}$ boson that decays into a muon and a muon neutrino. Events which consist of a single muon and missing transverse energy characterize $W \to \mu\nu$ events. All other processes which produce muons make up the background. Event selection is the process of applying certain conditions to the data in order to maximize the signal efficiency and to minimize the background. For this analysis we use two data samples: a sample of $W \to \mu\nu$ events from which the asymmetry distribution is extracted and a sample of $Z \to \mu\mu$ events, which are used to study identification efficiencies, charge mis-identification and other quantities that affect the asymmetry measurement.

5.1 Pre-Selection

For this analysis, the `wz_analyze` [56] package was run over the common samples single muon skimmed `[CS_1MUSKIM]` thumbnails for pass 1 data [57], in the p16.05.02 release, to generate `wz_analyze` root-tuples[1]. Runs marked bad by the SMT, CFT, CAL and Muon groups were removed. All special runs were excluded. Luminosity blocks marked bad by the luminosity, jet and missing energy groups were also removed. The remaining data sample is approximately 230 pb^{-1}.

The `CS_1MUSKIM` sample contains events with at least one muon with $p_T > 8$ GeV. A muon is identified as a track with hits in all layers (A, B and C) of the muon detector [59], both inside (A) and outside (B,C) the toroid. This sample contains the full muon p_T spectrum and was used for calculating the fake rate in Section 7.2.1. These `wz_analyze` root-tuples were then further skimmed to select events containing at least one muon with a

[1]The `CS_1MUSKIM` thumbnails contain data reconstructed with version p14 of the reconstruction code.

central track match and $p_T > 20$ GeV to facilitate faster processing. This sample was used for the final event selection and for all other studies conducted in this analysis.

5.2 Triggers

In this analysis we use two single muon triggers. These are MUW_W_L2M3_TRK10 and MUW_A_L2M3_TRK10 (the "wide" and the "all" triggers). The "wide" trigger covers the region $|\eta| < 1.5$ while the "all" trigger covers the region $|\eta| < 2.0$. At Level 1 (L1), these triggers require hits in the scintillators and wires of the muon detector (the trigger bits are mu1ptxwtlx and mu1ptxatlx), at Level 2 (L2) the triggers require one medium muon with $p_T > 3$ GeV and at Level 3 (L3), a track reconstructed in the central tracker with $p_T > 10$ GeV.

Since the "all" trigger is prescaled, alone it contributes less than 20% of the events in the W sample while using only the "wide" trigger alone contributes more than 97% of the events in the sample. Using the "all" trigger in addition to the "wide" trigger provides a gain in acceptance at higher η so the "all" trigger is used only for the forward η region not covered by the "wide" trigger. This is discussed in greater detail in Section 7.3. Since the triggers are used irrespective of the prescales, the luminosity of 230 pb^{-1} quoted for this analysis is an estimate.

5.3 Event Selection

In order to make maximal use of studies already performed at DØ , most of the selection cuts used in this analysis are the same as those used in the $W \to \mu\nu$ cross section analysis [61]. The selected events are required to have one 'good' muon. A 'good' muon is one which satisfies the following criteria.

1. The muon is required to lie within the geometrical acceptance of the muon detector which is defined as

   (a) $|x|$ or $|y| > 110$ cm to exclude the forward region around the beam pipe.

   (b) $|\eta| > 1.25$ for $4.25 < \phi < 5.15$ to exclude the 'bottom hole' of the muon detector.

   where x, y, η and ϕ are *local* muon track coordinates measured at the A-layer of the muon system.

2. The muon is required to be of at least 'medium' quality where 'medium' is defined in the p14 muon certification note [59].

3. The muon is required to be matched to a track in the central tracker [60] with track $p_T > 20$ GeV.

4. To ensure well reconstructed tracks with a low charge mis-identification rate, the following quality cuts are applied to the track associated with the muon:

   (a) The track is required to have > 8 hits in the CFT.

   (b) The track is required to have > 0 hits in the SMT.

   (c) The χ^2/degree of freedom of the track is required to be < 3.3.

5. Muons from cosmic rays are rejected in the following ways:

   (a) By applying scintillator timing cuts of ± 10 ns in the A layer of the muon detector.

   (b) By rejecting events where the absolute value of the distance of closest approach (dca) of the track matched to the muon, with respect to the primary event vertex in the $x - y$ plane, is more than 110 μm ($|\text{dca}| > 0.011$ cm). The beam position is measured separately for every run by the DØ tracking algorithm [62].

6. To reduce the probability of the muon originating from a semi-leptonic decay, the muon is required to be isolated in both the calorimeter and the central tracker, where

   (a) $\sum_{etcone5}(p_T) < 2.5$ GeV, where $\sum_{etcone5}(p_T)$ is the sum of the p_T of tracks in a cone around the muon with a radius $\Delta R < 0.5$, where $\Delta R = \sqrt{(\Delta\eta)^2 + (\Delta\phi)^2}$.

   (b) $\sum_{halo}(E_T) = \sum_{etcone4}(E_T) - \sum_{etcone1}(E_T) < 2.5$ GeV, where $\sum_{etcone4}(E_T)$ and $\sum_{etcone1}(E_T)$ are the sum of calorimeter clusters around the muon in cones of radius $\Delta R < 0.4$ and $\Delta R < 0.1$ respectively. The coarse hadronic part of the calorimeter is not considered when calculating these sums.

Besides having one 'good' muon, the following additional conditions are imposed on the event.

1. The event must have fired one of the single muon triggers MUW_W_L2M3_TRK10 in the region $|\eta| < 1.4$ or MUW_A_L2M3_TRK10 in the region $1.4 < |\eta| < 2.0$.

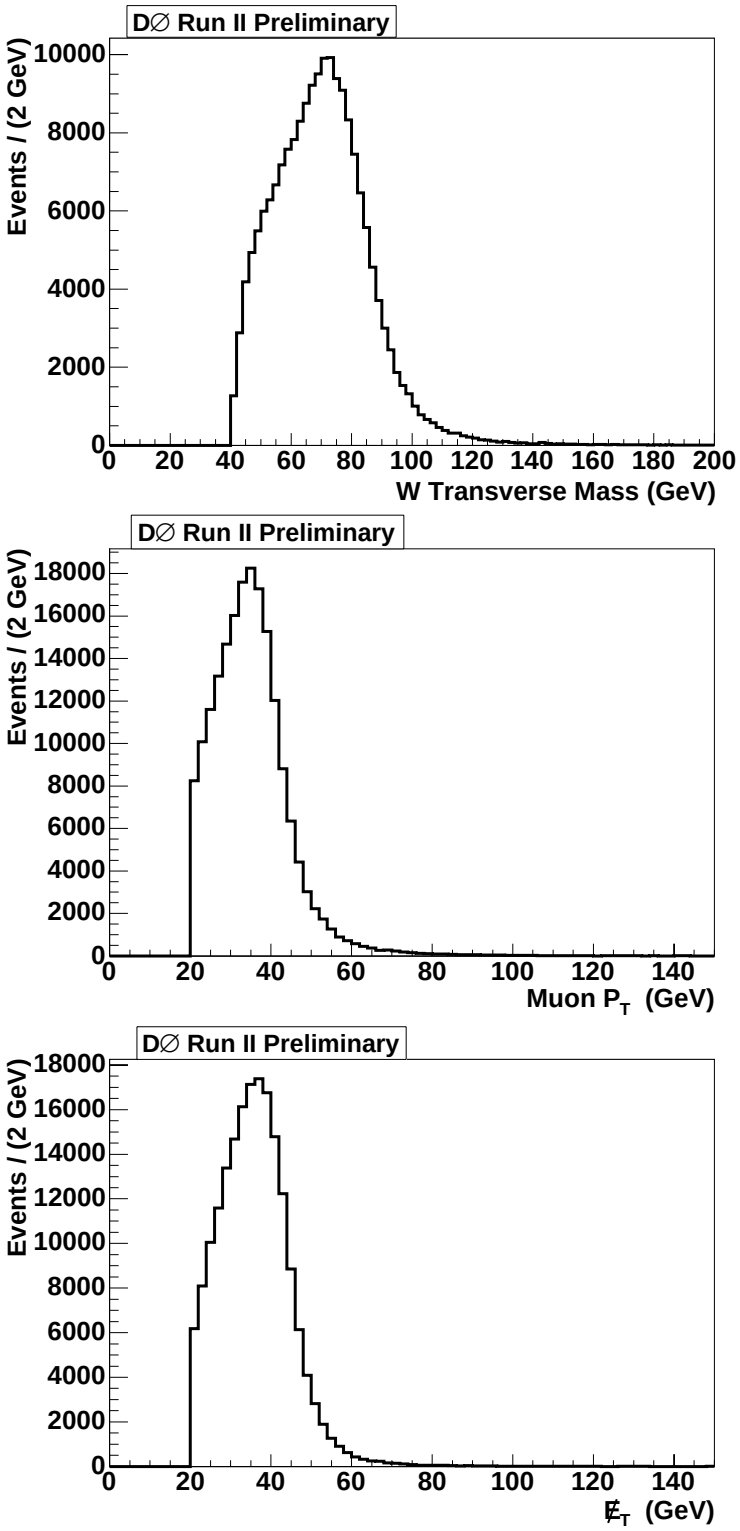

Figure 5.1: The resultant distributions of W transverse mass, the p_T of the muon and the $\not\!\!E_T$ after all selection cuts have been applied to data.

2. To account for the escaped neutrino in the case of W candidates, $\not\!\!E_T > 20$ GeV is required for the event.

3. In order to reduce the $Z \rightarrow \mu\mu$ background in the W sample,

   (a) All events with a second medium muon, with or without a central track match, are rejected. To avoid vetoing on mis-reconstructed muons close to the original muon, the second muon is required to be at least $\Delta\phi > 0.1$ away from the original muon.

   (b) All events with a second good track, satisfying 'good' muon conditions 4 and 5 above, back to back with the muon track ($|\Delta\phi| > 2.1$), are rejected.

4. In addition, the W transverse mass, M_T, is required to be > 40 GeV,
   where $M_T = \sqrt{(\not\!\!E_T + p_T)^2 - (\not\!\!E_x + p_x)^2 - (\not\!\!E_y + p_y)^2}$ and p_T, p_x and p_y are the transverse, x and y components of the muon momentum. This cut also limits the contribution from semi-leptonic decays.

Fig. 5.1 shows the resultant distributions of the W transverse mass, the muon p_T and the $\not\!\!E_T$ of the 189697 events after all the above selection cuts have been applied to data.

CHAPTER 6

Checking for Biases in Data

This chapter covers the investigation into any possible bias in the data. This includes looking for muon charge mis-identification, biases in efficiencies for positive and negative charges and checking for solenoid and toroid polarities.

6.1 Charge Misidentification

The measurement of the W boson charge asymmetry is sensitive to the misidentification of the charge of the muon as it depends on the number of positive and negative muons in each bin of rapidity. A positive muon misidentified as a negative muon or vice versa would dilute the true charge asymmetry. The charge mis-identification rate is estimated in data using a dimuon sample in which the events are required to fire one of the single muon triggers. This is then verified using a dimuon sample where the events are required to fire an independent set of dimuon triggers. The misidentification rate is also checked using a Geant (full detector simulation) Monte Carlo sample of $W \to \mu\nu$ events. The significance of momentum and the significance of curvature of the tracks are used as further qualitative cross checks.

6.1.1 Charge Misidentification rate

To check for charge misidentification in the data sample, dimuon events which have fired either of the single muon 'wide' or 'all' triggers are chosen. Two medium, track-matched muons are selected and they are required to satisfy all of the muon and track selection cuts described in Section 2.3. Events with a dimuon invariant mass > 40 GeV are selected to form a Z sample. The charge misidentification rate is defined as

$$\text{charge misid} = \frac{\text{N(same sign)}}{\text{N(same sign)} + \text{N(opposite sign)}}, \tag{6.1}$$

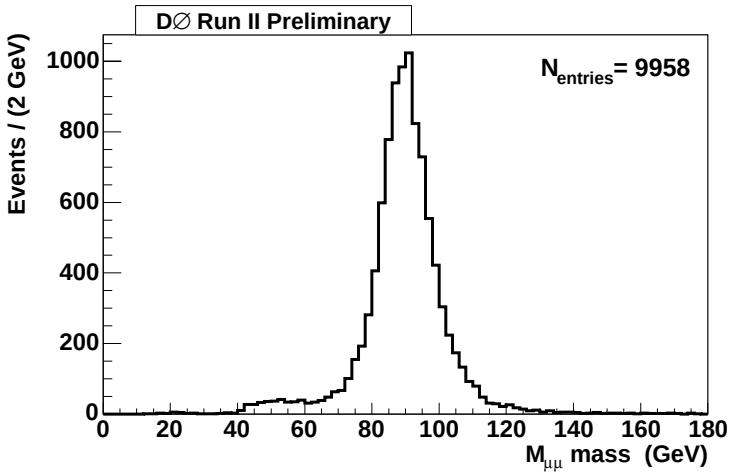

Figure 6.1: The dimuon invariant mass.

The Z sample is found to contain 9958 events (Fig. 6.1). In the sample, only one event is found to contain two same sign muons. Removing the dimuon invariant mass cut does not lead to an increase in the number of events with same sign muons. Neither does lowering the p_T cut on the muons from 20 to 15 GeV. In all cases, only the one event with two same sign muons was observed.

Tracks associated with the muons are required to pass very strict selection criteria. As these criteria are relaxed, an increase in the number of events in which both muons have the same sign charge is observed. Conversely, the decrease in the charge misidentification rate as a function of η was studied as the track quality conditions were gradually tightened in the sample.

If no track quality cuts are imposed whatsoever, the number of events with same sign muons in the sample where $M_{\mu\mu} > 40$ GeV, is found to be $(2.36 \pm 0.03)\%$ of the sample. Fig. 6.2 shows this misidentification rate as a function of η and the p_T distribution of the same sign muons. When only the isolation conditions are applied, the charge misidentification rate is found to be $(1.62 \pm 0.04)\%$ of the sample. Fig. 6.3 shows the charge misidentification rate in this case as well as the p_T distribution of the same sign muons. The isolation requirement is used to reduce the QCD contamination in the sample by rejecting muons originating from jets. It is expected that the excess of events with like-sign muons when no isolation is required likely arise from $b\bar{b}$ events which are characterized by a muon within a jet.

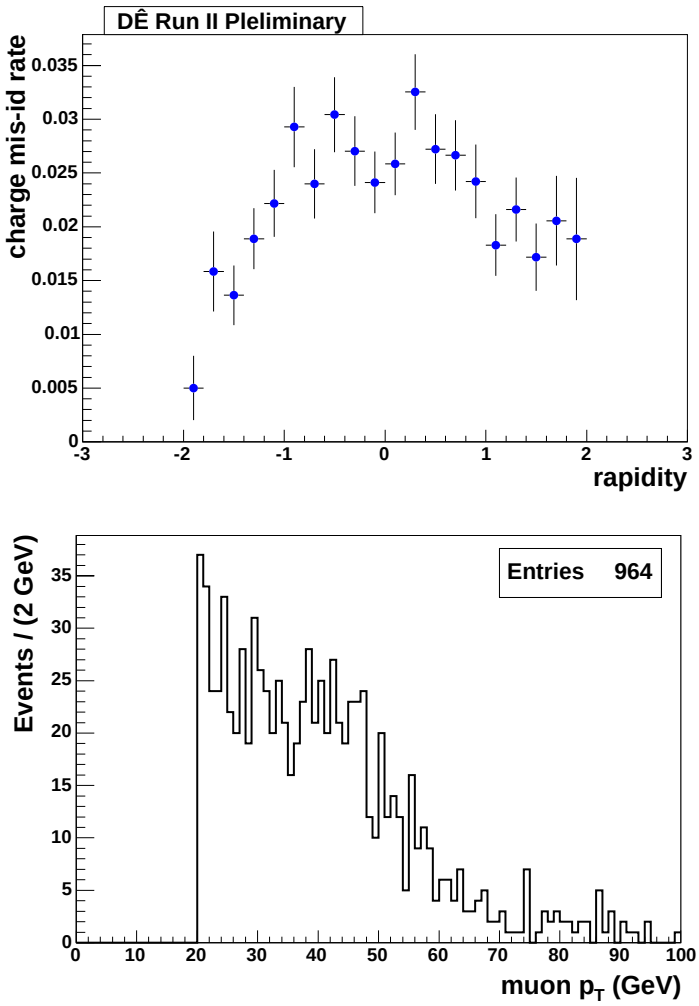

Figure 6.2: The upper plot shows the charge misidentification distribution as a function of η when the events are selected without any track quality requirements whatsoever. The lower plot shows the p_T distribution of the like-sign muon in this sample.

If CFT hits requirements are applied in addition to the isolation requirement, the fraction of events with same sign muons in the dimuon sample where $M_{\mu\mu} > 40$ GeV, decreases to $(0.35 \pm 0.05)\%$. Fig. 6.4 shows the charge misidentification rate as a function of η when both the CFT and the SMT hit requirements are appplied along withe isolation. Fig. 6.5 shows the charge misidentification rate as a function of η when the χ^2 requirement is further applied and Fig. 6.6 shows the charge misidentification rate as a function of η when t he dca but not the χ^2 requirement is further applied to the sample.

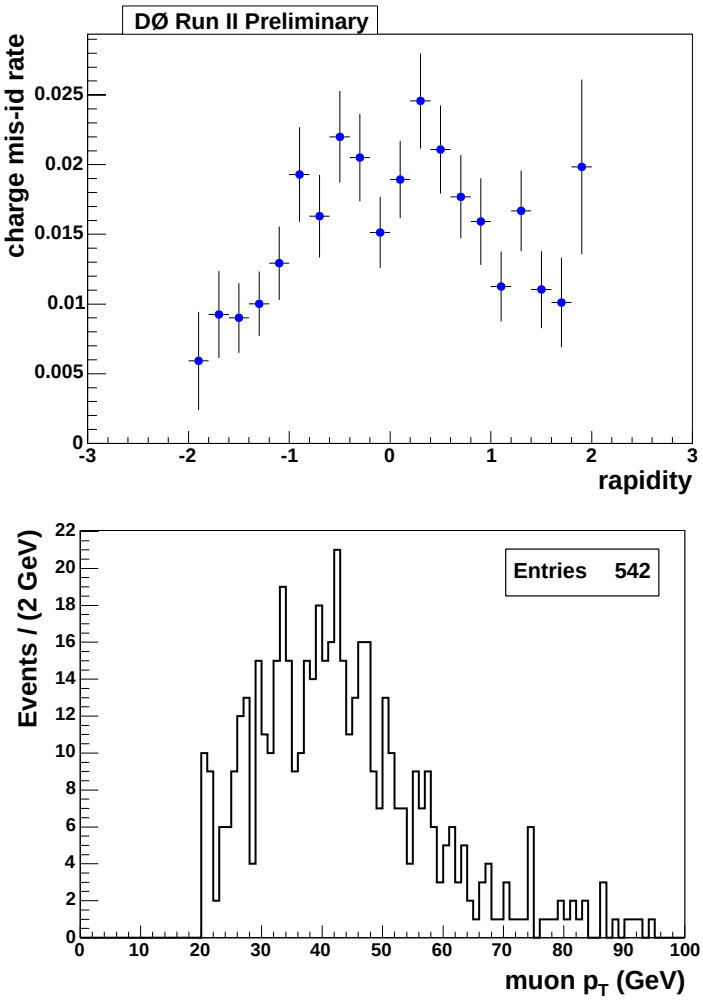

Figure 6.3: The upper plot shows the charge misidentification distribution as a function of η when the events are selected without any track quality requirements whatsoever. The lower plot shows the p_T distribution of the like-sign muon in this sample.

It can be inferred that the selection cuts are very efficient at picking tracks (associated with muons) with a good charge resolution and that the charge mis-identification rate is very low. This rate is estimated to be $(0.01 \pm 0.01)\%$.

Fig. 6.7 shows the scaled p_T distributions of muons in W and Z events. Since the muons in Z events have a harder p_T distribution than those in W events and since the probability that the charge of a track had been mis-assigned is greater for higher p_T tracks, it is unlikely that the charge mis-identification rate will be higher for W events than for Z events.

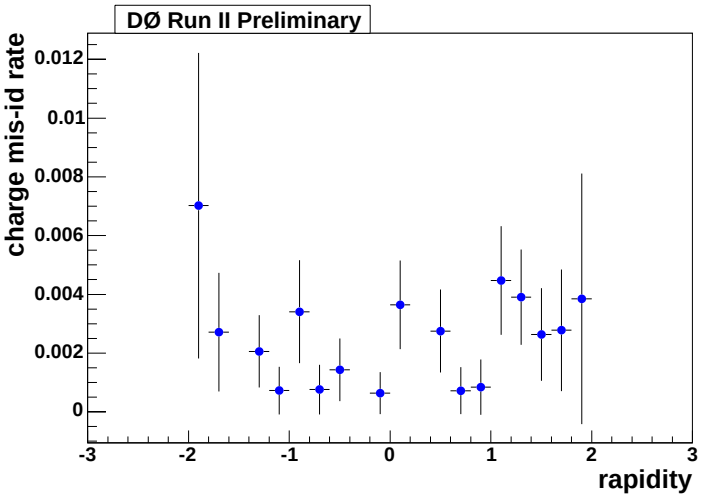

Figure 6.4: The charge misidentification distribution as a function of η when isolation requirements as well as SMT and CFT hits requirement are applied.

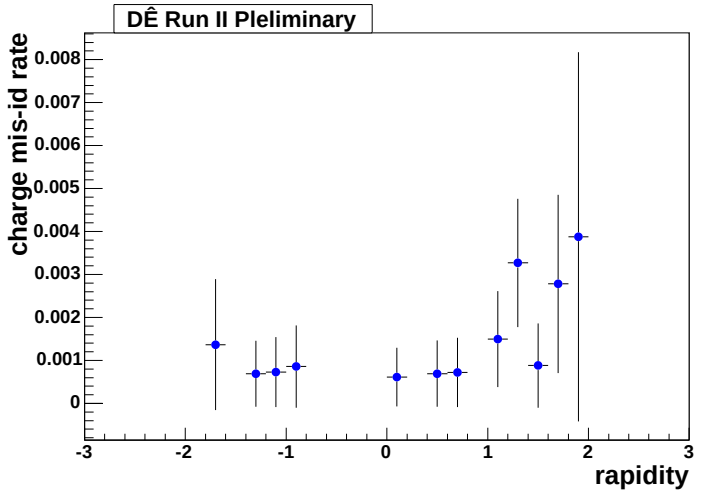

Figure 6.5: The charge misidentification distribution as a function of η when isolation requirements, SMT and CFT hits requirement as well as dca requirements are applied.

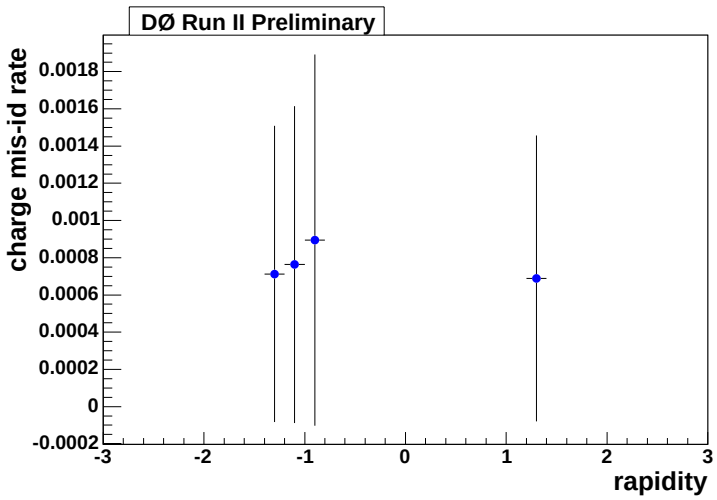

Figure 6.6: The charge misidentification distribution as a function of η when isolation requirements, SMT and CFT hits requirement as well as χ^2 (but no dca) requirements are applied.

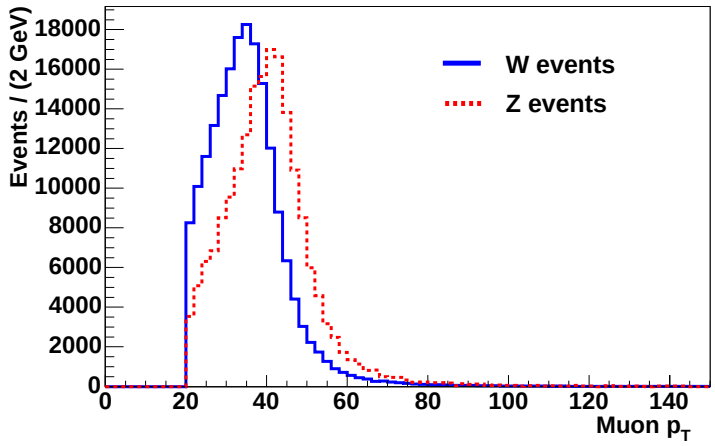

Figure 6.7: p_T distribution of muons in W events in blue solid and in Z events in red dashed (the p_T distribution of Z events was scaled to the number of events in the W sample).

6.1.2 Charge mis-identification with dimuon triggers

The charge mis-identification rate was further studied using an independent sample of events in which one of the dimuon triggers, 2MU_A_L2M0, 2MU_A_L2ETAPHI, 2MU_A_L2M0_L3L6 or 2MU_A_L2M0_L3L15, was required to have fired. Since these triggers do not have any track requirements (they only require two muons above a certain p_T threshold in given $|\eta|$), they can provide an unbiased sample on which to test the effectiveness of the track quality requirements imposed on the analysis sample. To select a dimuon sample, we require one good muon satisfying all the muon and track selection criteria described in Section 5.3. This is the tag muon.

In addition we require a second muon, the probe muon, which

1. is a medium, track matched muon with local muon $p_T > 15$ GeV.
2. is matched to an isolated track as described in Section 5.3, criterion 6.
3. lies within the muon detector acceptance.
4. satisfies the muon A-layer scintillator timing cut of ± 10 ns.
5. has an angular separation of $\Delta R > 2.0$ with the tag muon.

In the resultant dimuon sample we count how many events have the same sign charge for both of the muon central tracks. Fig. 6.8 shows the distribution of same sign tracks in η together with the distribution of all tracks in the sample. The resultant dimuon invariant mass is shown in Fig. 6.9. The charge mis-id rate is found to be $(0.25 \pm 0.03)\%$ of the sample. Tightening the local p_T cut on the probe muon to 20 GeV slightly increases the charge mis-id rate to $(0.27 \pm 0.02)\%$ of the sample. Tightening the p_T cut on the track of the tag muon to 30 GeV also has a similar effect. This indicates that the charge mis-id in this case is less likely to arise from the $b\bar{b}$ background.

If further track quality cuts are imposed on the central track matched to the probe muon, requiring it to satisfy conditions 4 (SMT, CFT hits and the χ^2 requirement) and 5b (dca requirement) as described in Section 5.3, we are left with 2 events in the sample of 19284 di-miuon events which have muons with the same sign charge. This supports the assigned charge mis-id rate of $(0.01 \pm 0.01)\%$ for the analysis sample.

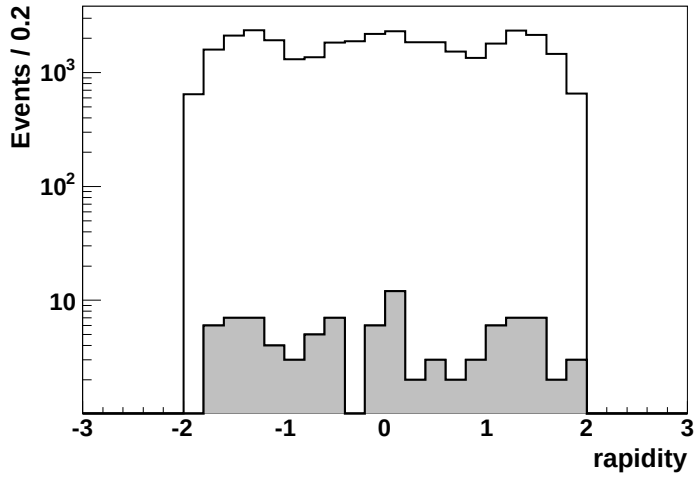

Figure 6.8: η distribution of same sign tracks in grey and the η distribution of all tracks in white for the dimuon sample.

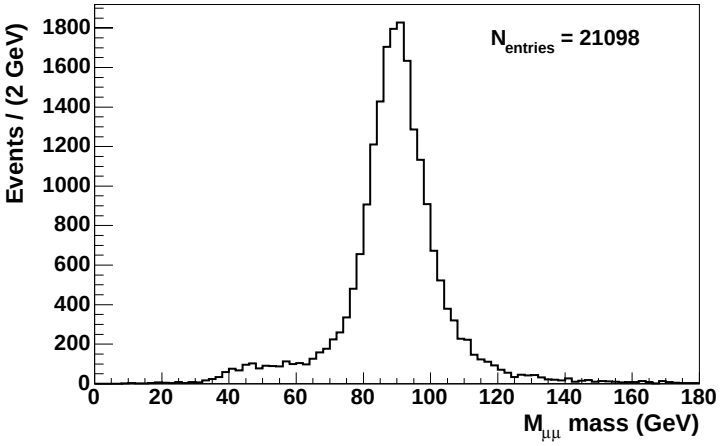

Figure 6.9: The dimuon invariant mass in a sample of events which fires one of the dimuon triggers.

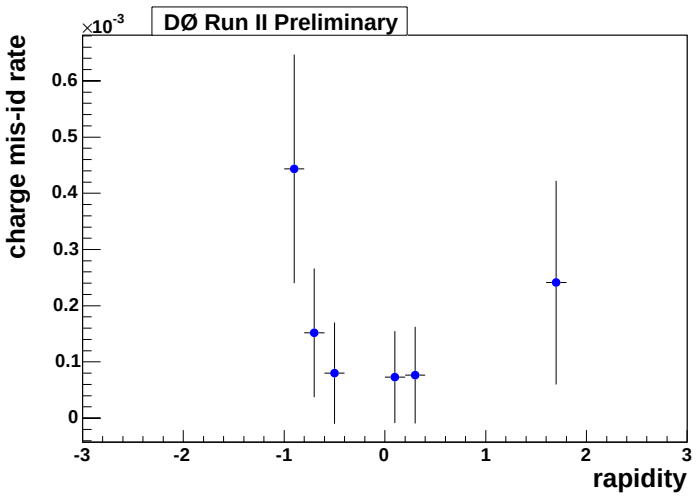

Figure 6.10: The charge misidentification distribution in Monte Carlo as a function of η.

6.1.3 Cross check of charge mis-identification using Geant

The charge mis-identification rate was also studied using a sample of 594K $W \to \mu\nu$ events generated with Pythia and passed through the full Geant simulation. The charge of the track at the generator level was compared to the charge of the recontructed track. The charge mis-identification rate in this sample is defined as

$$\text{charge misid} = \frac{\mathrm{N}(\mathrm{q_{gen}} \neq \mathrm{q_{reco}})}{\mathrm{N}(\mathrm{q_{gen}} \neq \mathrm{q_{reco}}) + \mathrm{N}(\mathrm{q_{gen}} = \mathrm{q_{reco}})}. \tag{6.2}$$

Fig. 6.10 shows the charge misidentification rate as a function of η in the Geant sample. The charge misidentification rate is found to be very low with the largest value at an η of -1 which is $< 0.05\%$. Charge mis-identification is therefore not expected to have any significant influence on the final charge asymmetry distribution. However, the charge misidentification rate of $(0.01 \pm 0.01)\%$ found in data is used to assign a systematic uncertainty to the muon charge asymmetry. Since the statistics are somewhat inconclusive at higher η, the systematic uncertainty for $|\eta| > 1.0$ is scaled by a safety factor of 5.0. This value for the safety factor is arrived at 'by eye' using the results of the charge misidentification rate in data and in Monte Carlo.

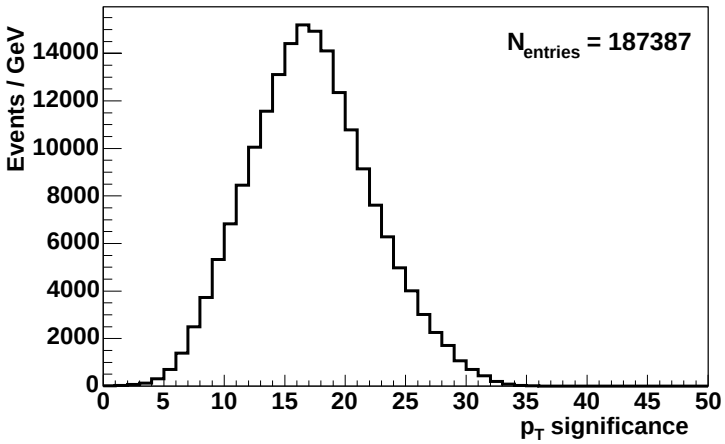

Figure 6.11: p_T significance of all muon tracks in the W sample

Significance of p_T

As an additional cross-check, we look at the p_T significance of the tracks in the W sample after all the selection cuts have been applied. The p_T significance of a track is defined as

$$S(p_T) = \frac{p_T}{\text{error in } (p_T)}. \tag{6.3}$$

The probability of a track being mis-identified is highest when the significance is close to zero and falls away rapidly as the significance increases. Fig. 6.11 shows that the bulk of the tracks in the W sample are safely away from $S(p_T) = 0$.

Significance of Curvature of tracks

The curvature of a track is $\propto \ (q/p_T \times B)$ where B is the magnetic field of the solenoid. Since p_T is always positive, the charge of a track determines the sign of its curvature. This is described in more detail in the DØ note on the W charge asymmetry in the electron channel [64]. The curvature of a track is measured by fitting an arc parameterized by chord length and arc height. The error in the curvature is approximately Gaussian, more so than the error in p_T. Therefore, we also look at the significance of *curvature* of the track, which is defined as

$$S(q/p_T) = \frac{(q/p_T)}{\text{error in } (q/p_T)}. \tag{6.4}$$

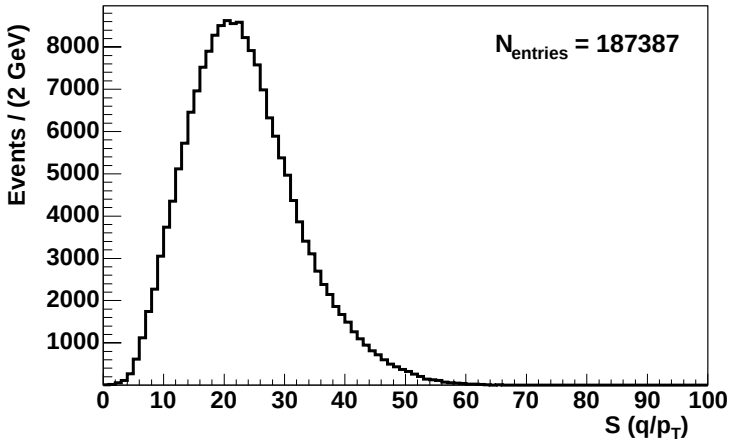

Figure 6.12: Curvature significance of all muon tracks in the sample.

Fig. 6.12 shows the significance of curvature of the muon tracks in the sample of W events. The probability density of the significance of curvature provides a way to assess the probability that a track is mis-identified due to an error in the measurement of the track curvature (likeliest at higher p_T). We do not cut on the curvature significance for this analysis. Only 0.01% of the events lie in the region $S(q/p_T) < 2$ where the probability that the charge of a track has been incorrectly assigned is the highest ($< 5\%$).

6.2 Efficiencies

The W boson charge asymmetry can be measured as the difference divided by the sum of the number of positive and negative muons in each η bin (Eq. 4), corrected for the backgrounds, when the efficiencies for positively and negatively charged muons are the same. So it is important to check that there are no charge, p_T or η biases in the efficiencies. We look at the offline medium muon reconstruction efficiency, the L1-L2 muon trigger efficiency, the tracking efficiency, the L3 trigger efficiency and the isolation efficiency. The differences between the efficiencies of the positive and negative charges, if any, need to be corrected for and would contribute towards systematic uncertainties.

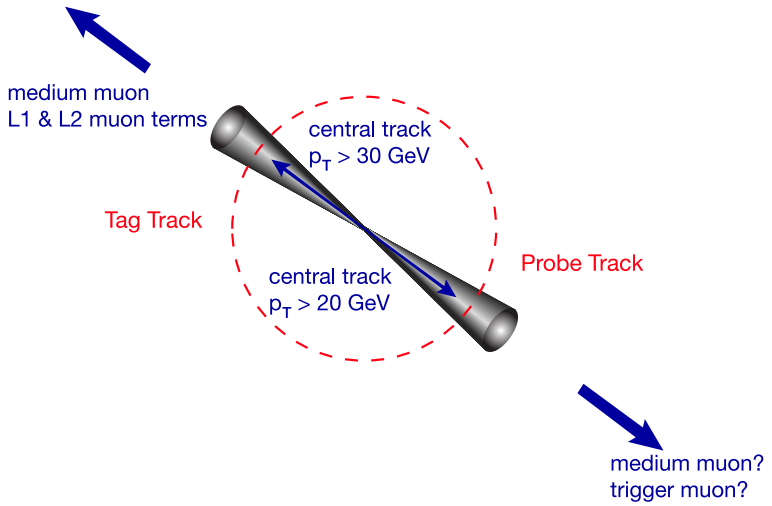

Figure 6.13: Tag and probe method for L2 trigger and offline muon reconstruction efficiencies

6.2.1 Offline Muon Reconstruction Efficiency

The offline muon reconstruction efficiency is the efficiency of finding an offline medium muon that is matched to an offline central track. We use the tag and probe method described in Fig. 6.13 for a sample of dimuon events. It is possible to select a clean dimuon sample, free of $b\bar{b}$ background and cosmic ray muons even if only one of the two muons fires a single muon trigger and is reconstructed in the muon chambers [63]. To choose the sample we require that the event fire any one of the single muon triggers MU_W_L2M3_TRK10, MU_W_L2M0_TRK3, MU_W_L2M0_2TRK3, MU_W_L2M5_TRK10, MUW_W_L2M3_TRK10, MUW_W_L2M5_TRK10 or MUW_A_L2M3_TRK10.

We require a tag muon that satisfies all the criteria that define a 'good' muon as defined in Section 5.3 except that the central track has a tighter p_T requirement with $p_T > 30$ GeV. In addition, the tag muon is required to

1. have an associated L1 trigger term, defined as
   (a) Δscintillator octant(trigger, offline) < 2.0
   (b) Δscintillator η(trigger, offline) < 2.0
   (c) Δwire octant(trigger, offline) < 2.0

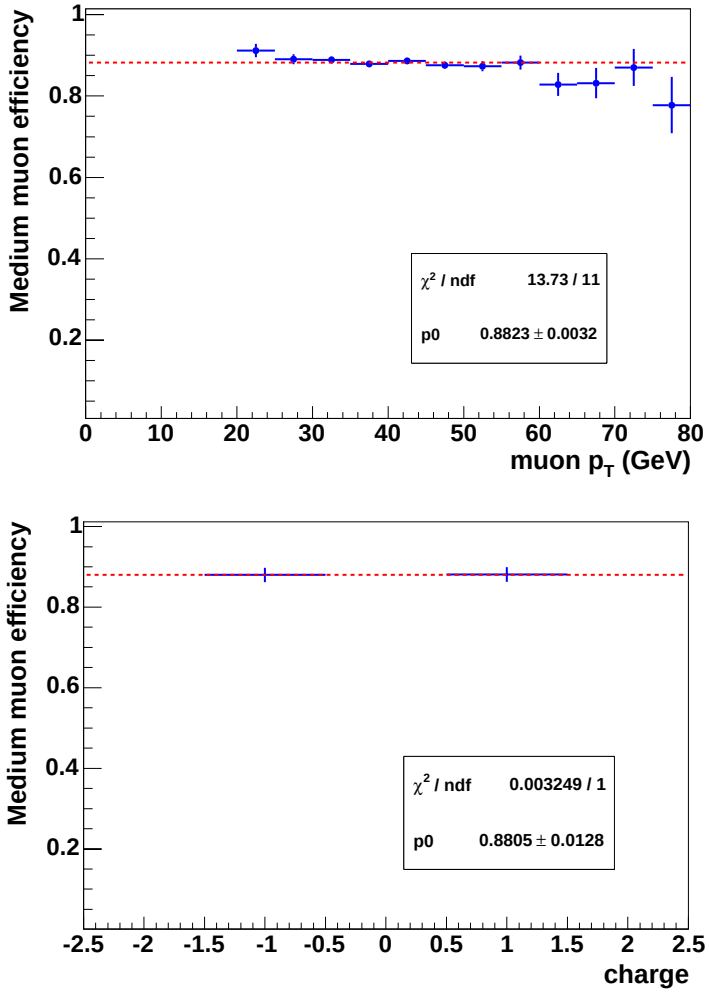

Figure 6.14: The offline medium muon reconstruction efficiency as a function of a) p_T and b) charge.

(d) Δwire η(trigger, offline) < 2.0

2. have an associated L2 trigger term defined as a match in η and ϕ with $\Delta R < 0.95$ between the offline and the trigger muon object.

We require an additional probe track in the sample which

1. is a central track with $p_T > 20$ GeV

2. lies within the muon detector acceptance

3. has > 8 CFT hits, > 0 SMT hits, $\chi^2/d.o.f. < 3.3$ and $|dca| < 0.2$

4. is isolated in the calorimeter and the tracker

5. has an angular separation of $\Delta R > 2.0$ from the tag track.

The tag muon is required to have the associated L1 and L2 trigger terms in order to avoid any bias with the trigger fired, that is to ensure that the tag muon fired the trigger. For the ditrack invariant mass of > 40 GeV, we count for how many of the events the central probe track has a muon associated with it. In other words, we check to see that the probe track was indeed assigned to a valid muon candidate. This gives the loose muon reconstruction efficiency. Furthermore, if the muon matched to the central track is a medium muon, that is the medium muon reconstruction efficiency. For this analysis, we are interested in possible biases in the medium muon reconstruction efficiencies.

Fig. 6.14 shows the efficiency for medium muon reconstruction as a function of p_T and of charge. The efficiency appears to be flat with a value of 0.882 ± 0.003 and with a $\chi^2/d.o.f.$ of 1.25. The efficiencies when split into positive and negative charges also agree with each other within statistical errors.

Fig. 6.15 shows the medium muon reconstruction efficiency as a function of η with the positive and negative charges charges separated out in the top plot. This plot gives a Kolmogorov probability of 0.992 with a maximum displacement of 0.051 between points, where a Kolmogorov probability of 1.0 implies perfect agreement between two distributions. The errors on the plot of efficiency as a function of η (throughout this technical note) are calculated as Bayesian uncertainties on the efficiencies[65]. The details of the efficiency calculations are provided in Appendix A. The bottom plot in Fig. 6.15 shows the ratio of the efficiencies of positive and negative muons. This ratio fitted to a constant gives an average value of 1.001 ± 0.007 with a $\chi^2/d.o.f.$ of 0.48.

6.2.2 L2 Muon Efficiency

We study the efficiencies for the "wide" and "all" single muon triggers, (described in Section 5.2), to ascertain to what level the efficiencies for triggering on positive and negative muons are the same. These triggers together cover the region $|\eta| < 2.0$. We study the muon efficiencies at L1 and L2 (together referred to L2) and the track efficiencies at L3 for

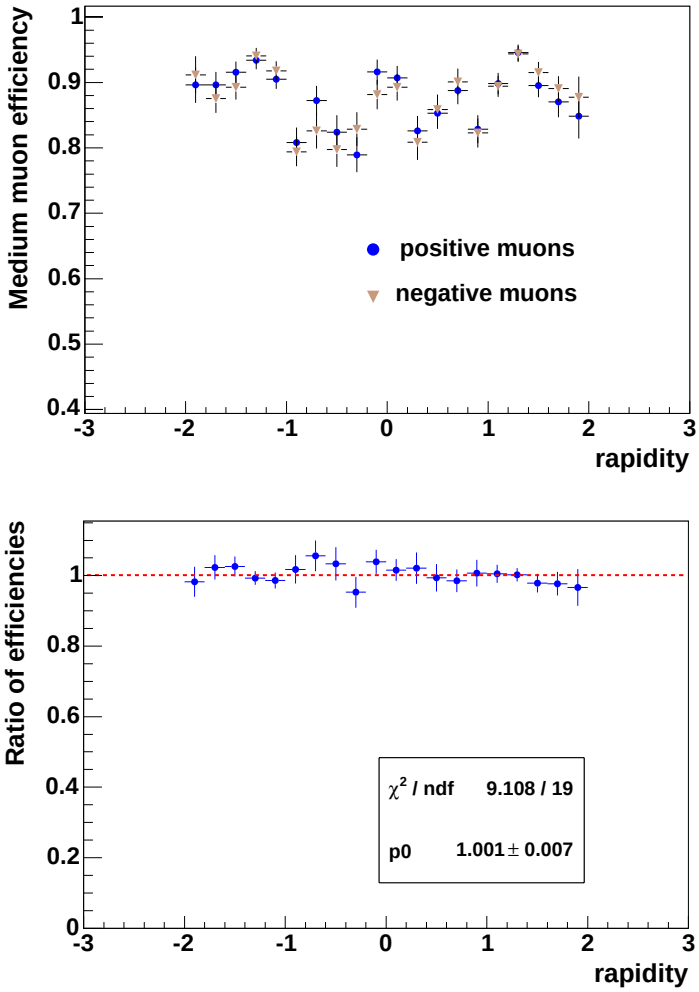

Figure 6.15: The upper plot shows the offline medium muon reconstruction efficiency as a function of η with the positive and negative charges are separated. The lower plot shows the ratio of positive and negative efficiencies as a function of η.

these triggers. Rather than the absolute efficiencies, we are interested in any charge or p_T dependence in the efficiencies in the sample.

The L2 muon efficiency is measured given the medium muon reconstruction efficiency. The tag and probe method (Fig. 6.13) in a clean dimuon sample is again used in this case. This sample is chosen in the same way as for the offline muon reconstruction efficiency, with the additional condition that the probe muon is required to be of at least medium quality. For dimuon mass $>$ 40 GeV, we count how many of the probe muons have an associated L2

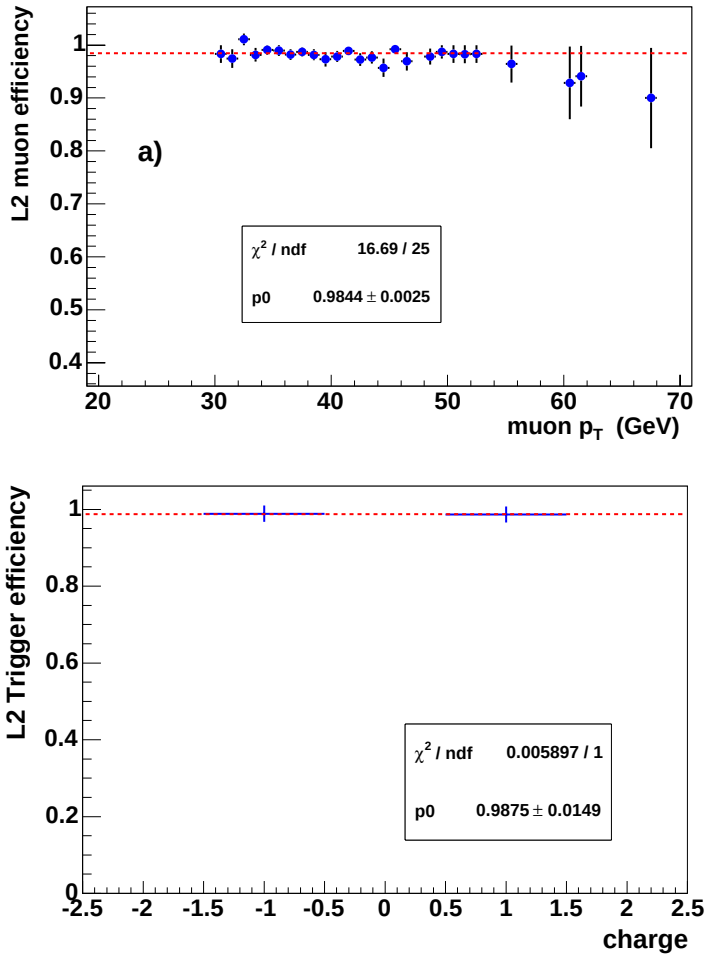

Figure 6.16: The L2 muon efficiency as a function of p_T (top) and charge (bottom).

trigger term which is defined as a spatial match with $\Delta R < 1.0$.

We look at the L2 muon efficiencies as functions of p_T and of charge as shown in Fig. 6.16. The efficiency as a function of p_T appears flat at a value of 0.9844 ± 0.0025 and with a $\chi^2/d.o.f.$ of 0.668. The average efficiencies when split into charges also show good agreement with each other.

Fig. 6.17 shows the efficiencies for positive and negative charges as functions of η. This gives a Kolmogorov probability of 0.999 with a maximum displacement of 0.003 between points showing that the efficiencies for positive and negative charges are consistent with each other. The ratio of these efficiencies is also plotted as a function of η and fitted to a

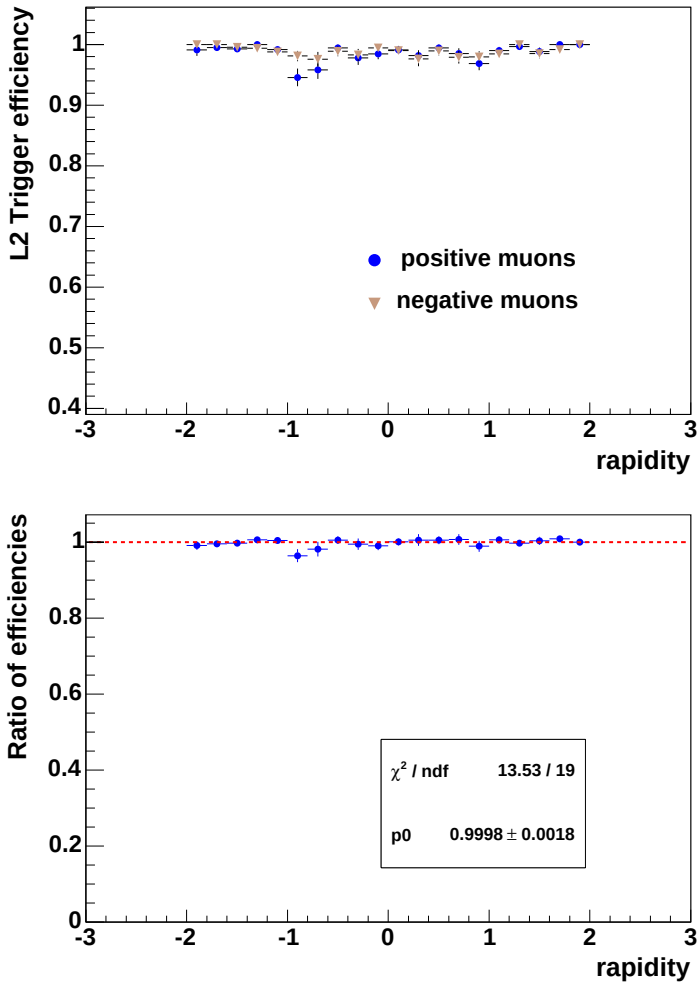

Figure 6.17: The L2 muon trigger efficiencies as a function of η, when separated into positive and negative charged muons in the top plot and the ratio of these efficiencies in η at the bottom.

constant value. The average value of the ratio is 0.999 ± 0.002 with a $\chi^2/d.o.f.$ of 0.712.

6.2.3 Track Reconstruction Efficiency

The track reconstruction efficiency is defined as the efficiency of finding a central track that satisfies the track quality conditions and is matched to an offline muon. It is possible to select a clean dimuon sample by requiring only one of the muons to have a central track [63]. The track reconstruction efficiency is measured using the tag and probe method (Fig. 6.18)

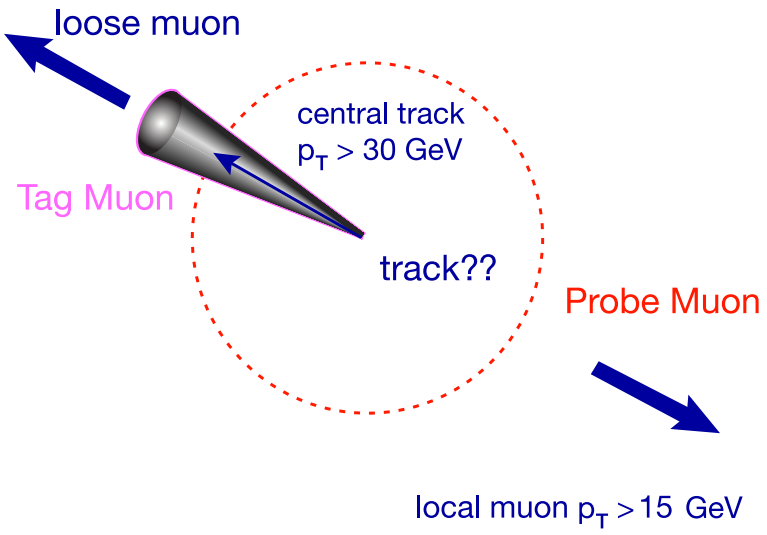

Figure 6.18: Tag and probe method for L3 trigger and track reconstruction efficiencies

in such a sample of dimuon events. In order to avoid any trigger bias we require the event to fire one of the dimuon triggers 2MU_A_L2M0, 2MU_A_L2ETAPHI, 2MU_A_L2M0_L3L6 or 2MU_A_L2M0_L3L15 which do not have any track requirements.

To select the dimuon sample we require a tag muon that satisfies all the criteria for a 'good' muon as defined in Section 5.3 except that the central track matched to the muon must have $p_T > 30$ GeV. In addition we require a probe muon in the sample that

1. is at least a loose muon (where 'loose' is defined in the p14 muon certification note [59]), with local muon $p_T > 15$ GeV (the definition of a loose muon has been modified to avoid requiring a central track matched to the muon)

2. lies within the muon detector acceptance

3. satisfies the muon A-layer scintillator timing cut of ± 10 ns

4. has an angular separation of $\Delta R > 2.0$ from the tag muon.

For the dimuon invariant mass (reconstructed using the tag muon track and the probe local muon track) > 30 GeV, we count how many events have a track associated with the probe muon when the track has > 8 CFT hits, > 0 SMT hits, $\chi^2/d.o.f. < 3.3$ and $|dca| <$

0.2. Fig. 6.19 shows the efficiency as a function of p_T which is 0.842 ± 0.003 when fitted to a straight line with a $\chi^2/d.o.f.$ of 1.72. There is no observable bias when the efficiencies are separated out by charge.

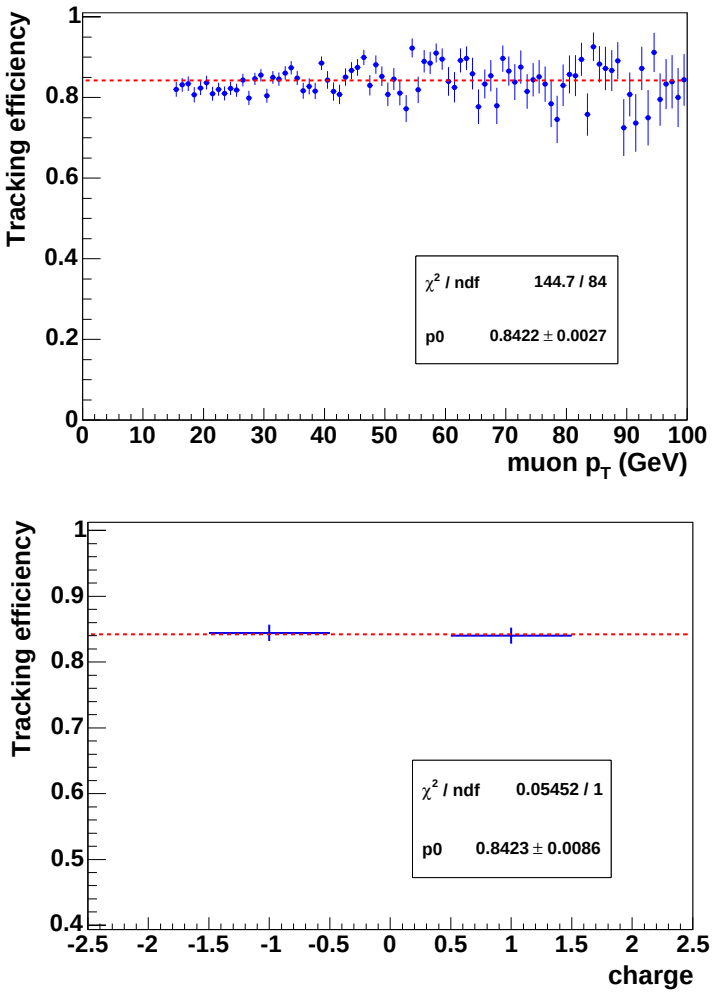

Figure 6.19: The upper plot shows the tracking efficiency as a function of p_T while the lower plot shows the tracking efficiency as a function of charge.

Fig. 6.20 shows the efficiency as a function of η, split into positive and negative charges. The Kolmogorov probability is 0.99 with a maximum displacement of 0.049 between points which shows very good agreement between the efficiencies of the charges. The ratio of the efficiencies for the positive and negative charges is also shown in this plot. Fitted to a

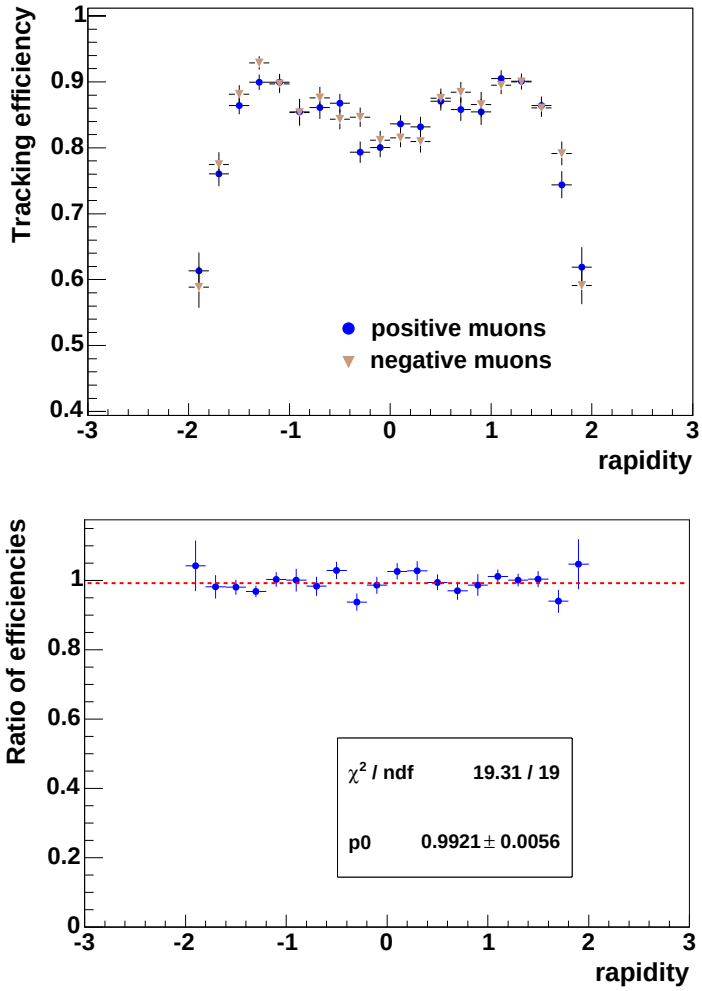

Figure 6.20: The upper plot shows the tracking efficiency as a function of η with the positive and negative charges separated out while the lower plot shows the ratio of these efficiencies as a function of η.

constant, this gives an average efficiency of 0.992 ± 0.006 with a $\chi^2/d.o.f.$ of 1.02.

6.2.4 L3 Track Efficiency

To measure the L3 track efficiency, we use the tag and probe method as described in Fig. 6.18 in a sample of dimuon events with loose muon candidates that fire the "wide" or "all" single muon triggers (described in Section 5.2), lie within the detector acceptance and are

not cosmic muons. In addition to the conditions required as in the offline tracking efficiency as described in Section 6.2.3, we also require an offline track to be associated with the probe muon.

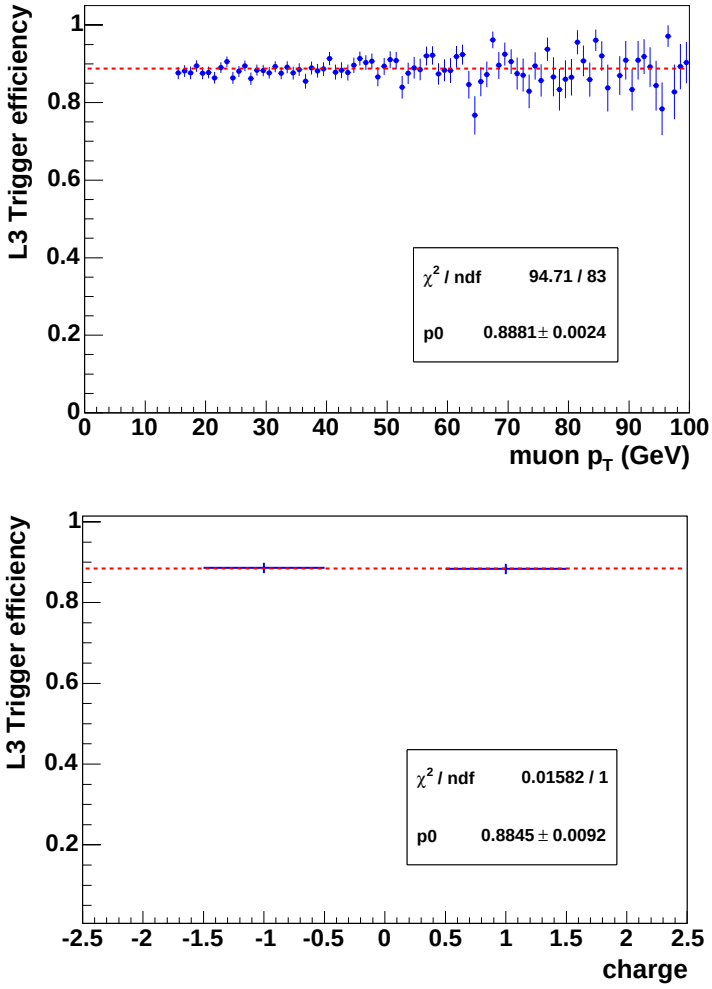

Figure 6.21: The upper plot shows the L3 track efficiency as a function of p_T and the lower plot shows the L3 track efficiency as a function of charge.

For events with dimuon mass > 30 GeV, we count how many of the probe muons have an associated L3 trigger term which is defined as a spatial match with $\Delta R < 1.0$ between the offline and the trigger track objects. The L3 track efficiency as functions of p_T and of charge are shown in Fig. 6.21. The efficiency as a function of p_T appears flat at a value

of 0.888 ± 0.002 and with a $\chi^2/d.o.f.$ of 1.14. The efficiencies separated into positive and negative charges are again consistent within statistical errors.

Fig. 6.22 shows the L3 track efficiency as a function of η, split into positive and negative charges. The Kolmogorov probability is 0.999 which shows good agreement between the charges. The ratio of these efficiencies plotted as a function of η have an average value of 0.993 ± 0.004 when fitted to a constant with a $\chi^2/d.o.f.$ of 0.96.

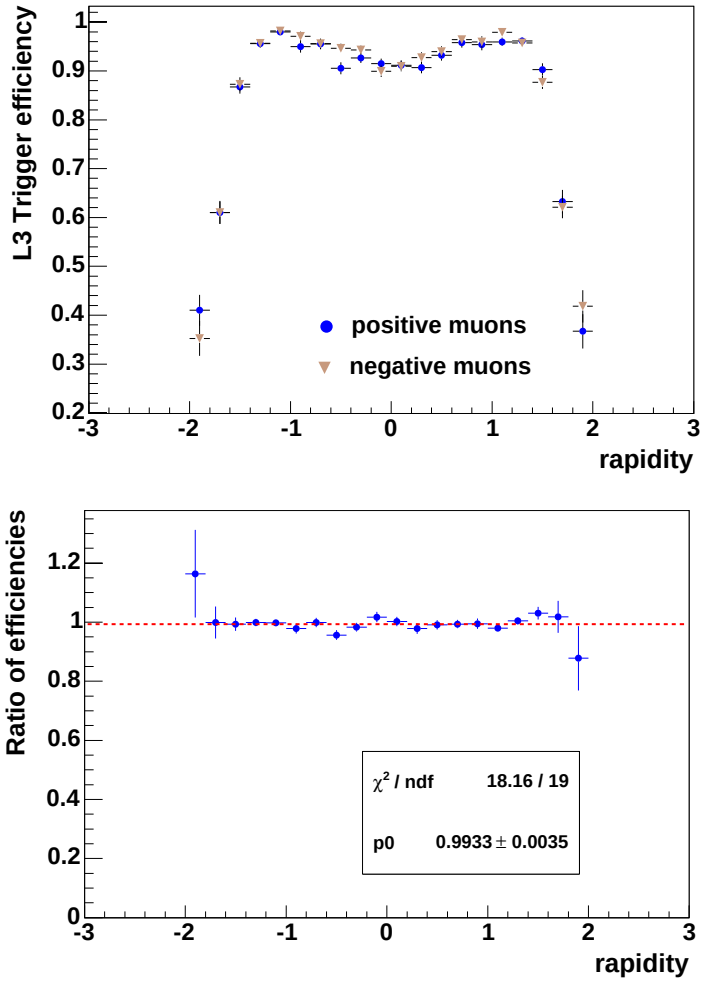

Figure 6.22: The upper plot shows the L3 track efficiency as a function of η with the positive and negative muons separated out while the lower plot shows the ratio of positive and negative efficiencies for L3 track trigger efficiencies as a function of η.

6.2.5 Evaluation of Systematics

To evaluate the systematic uncertainties arising from the difference in the efficiencies of positive and negative muons, we combine the various efficiencies as follows for each bin in η:

$$\varepsilon_{\pm} = \varepsilon_{\pm}(\text{offline muon}) \times \varepsilon_{\pm}(\text{L2 muon}) \times \varepsilon_{\pm}(\text{offline track}) \times \varepsilon_{\pm}(\text{L3 track}) \qquad (6.5)$$

Fig. 6.23 shows this combined efficiency distribution as a function of η with the efficiencies for the positive and negative charges separated out. The errors for each individual efficiency have been added in quadrature to give the errors for this distribution. There may be correlations between the individual components due to the fact that the muon identification efficiency makes use of the tracking while the tracking efficiency makes use of muon identification. However, since the ratio of the positive and negative efficiencies in each case is very close to 1.00 as demonstrated in the previous sections, it is expected that any correlations that come into play while combining the efficiencies are only second order effects and can be ignored for our purposes.

The bottom plot in Fig. 6.23 shows the combined ratio between positive and negative efficiencies. This ratio is found to be constant as a function of η at the value of 0.99 ± 0.01 and with a $\chi^2/d.o.f.$ of 0.71. For the purpose of this analysis a value of $k = 1.0$ is used in Eq. 6 to calculate the W charge asymmetry. The systematic uncertainties are evaluated by varying k by $\pm 1\sigma$ where $\sigma = 0.01$. The systematic uncertainties due to the variation of k are propagated to the asymmetry and are listed in Table 8.5 for each bin in η.

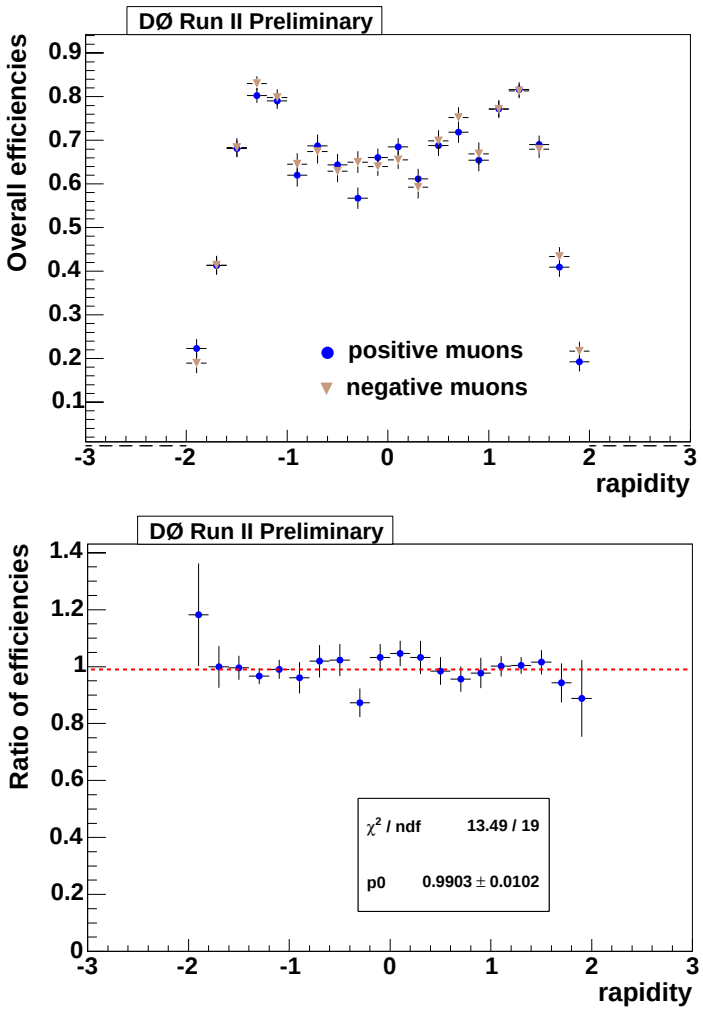

Figure 6.23: Combined efficiency distributions by charge as a function of η on the top and the plot of the ratio of these efficiencies as a function of η fitted to a straight line at the bottom.

6.2.6 Isolation Efficiency

The electroweak background contamination in the data sample is estimated using Monte Carlo events that have been smeared for detector effects using PMCS (see Sec. 6). However, the isolation condition for muons is not modeled in PMCS. The isolation efficiency measured in data is therefore used to correct the Monte Carlo p_T distribution for isolation effects.

The QCD background contamination in the data sample is evaluated from data using the Matrix method (see Section 7.2.2). One of the input parameters for the Matrix method

is the signal isolation cut efficiency. The isolation efficiency measured in data is therefore also used as an input to the Matrix method.

The isolation efficiency is measured in data using the tag and probe method in a sample of dimuon events where the tag is chosen as a track-matched isolated muon satisfying all track and muon selection requirements as described in Section 5.3 and the probe is chosen as a track-matched muon satisfying all of the same conditions except that it is not required to be isolated in either the tracker or the calorimeter. The fraction of isolated probe tracks with dimuon mass > 40 GeV give the efficiency.

The isolation efficiency is plotted as a function of p_T in Fig. 6.24a. The efficiency is fitted to a constant value of 0.9209 ± 0.0018 with a $\chi^2/d.o.f. = 5.77$. A better value of $\chi^2/d.o.f.$ can be obtained by fitting this distribution to a first order polynomial. Due to the fact that a single value of the isolation efficiency is used as an input to the Matrix method and for the sake of consistency throughout the analysis, the fitted constant value of 0.9209 is chosen as the central value of the isolation efficiency. An error, larger than the error in the fit, is assigned to the efficiency in order to make up for the bad χ^2 of the fit.

To determine this error, the isolation efficiency distribution is projected onto the y axis with weights assigned for the number of events in each bin of p_T. The mean of this distribution is the average isolation efficiency and it has an rms = 0.022. This value of the rms is assigned as the error in the isolation efficiency so that,

$$\text{Isolation cut efficiency}(\varepsilon) = 0.9209 \pm 0.022. \tag{6.6}$$

The isolation efficiency is also shown in Fig. 6.24 as a function of charge and as a function of η separately for $+$ and $-$. The efficiency as a function of η has a Kolmogorov probability of 0.999 with a maximum displacement of 0.006 between points. The average isolation efficiency is 0.916 ± 0.009 with good agreement between the positive and negative charges.

The systematic uncertainty due to the error in the isolation efficiency is evaluated by varying the value of the efficiency by $\pm 1\sigma$ while estimating the electroweak backgrounds from Monte Carlo. The systematic uncertainties due to the variation of isolation efficiency, for each bin in η, are listed in Table 8.5.

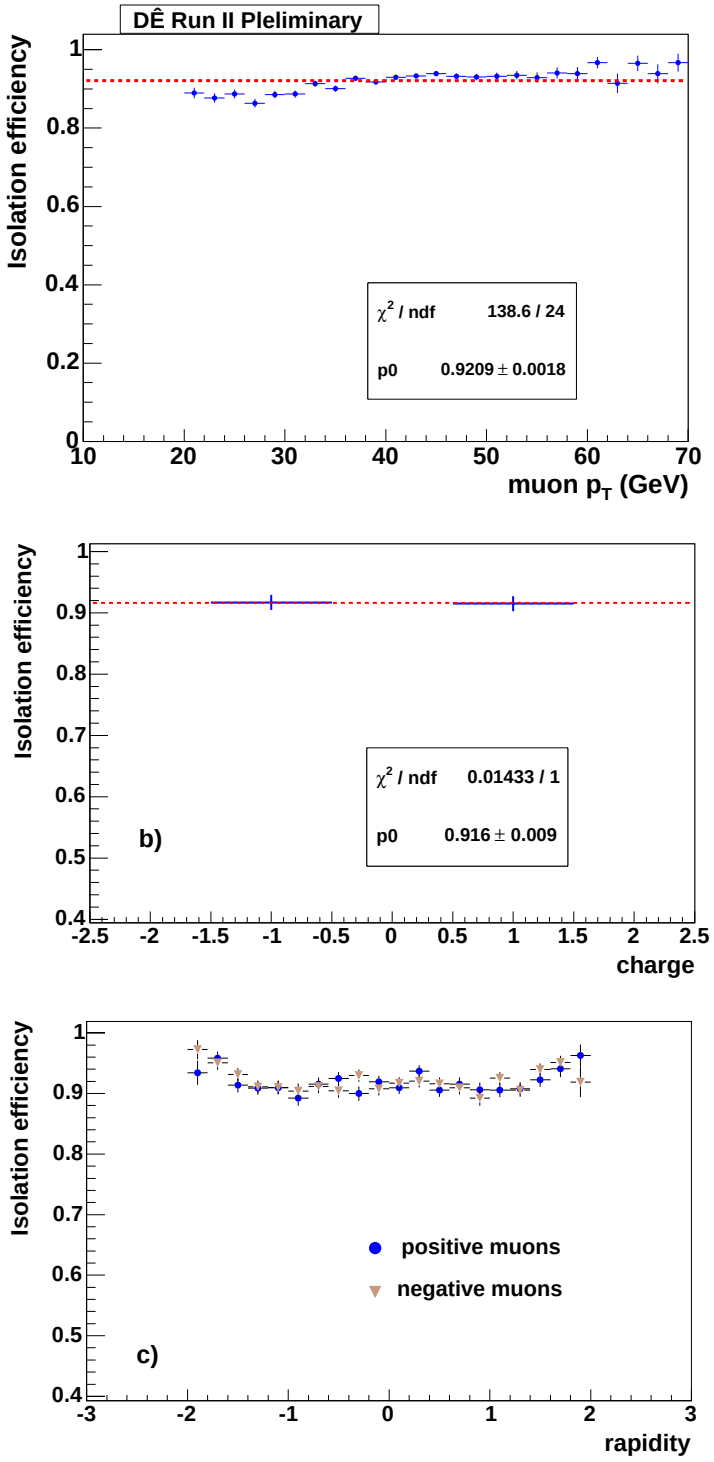

Figure 6.24: The isolation efficiency plotted as a function of a) p_T, b) charge and c) as a function of η with the positive and negative charges separated out.

6.3 Other Biases

We also look for other possible sources of bias. We look at the raw asymmetry distribution for different solenoid and toroid polarities and check for possible detector effects by comparing the raw asymmetry distribution for positive and negative rapidities (or CP folding, described in Section 6.3.2).

6.3.1 Polarity effects

The solenoid polarity influences the charge identification of tracks in the central tracker and can introduce a bias. Fig. 6.25 shows the raw asymmetry distributions for the two solenoid polarities. The toroid polarity influences the muon trigger efficiencies and could be another source of bias. Fig. 6.26 shows the raw asymmetry distributions for the two toroid polarities. To increase statistics, the solenoid polarities have been studied independently from the toroid polarity and vice versa.

Fig. 6.25 gives a χ^2 probability of 0.703 for the asymmetry distributions for the two different solenoid polarities, independent of the toroid polarity. This indicates good agreement between the forward and reversed solenoid field directions. Fig. 6.26 gives a χ^2 probability of 0.079 for the asymmetry distributions for the two different toroid polarities, independent of the solenoid polarity. A closer examination reveals that this value is primarily due to three bins in η which lie within (2–3)σ of each other. This is acceptable within statistical errors. The χ^2 probability, if these three points were to be excluded, is 0.902. Also, 50.7% of the selected W sample was found to have forward Toroid polarity while 49.3% of the selected W sample was found to have reverse Toroid polarity. So any systematic uncertainties arising due to the difference in Toroid polarities should cancel.

Moreover, since the differences between the positive and negative efficiencies due to the trigger and the tracking have already been used to estimate the systematic uncertainties, it is believed that further corrections due to the solenoid or toroid polarities would lead to double counting.

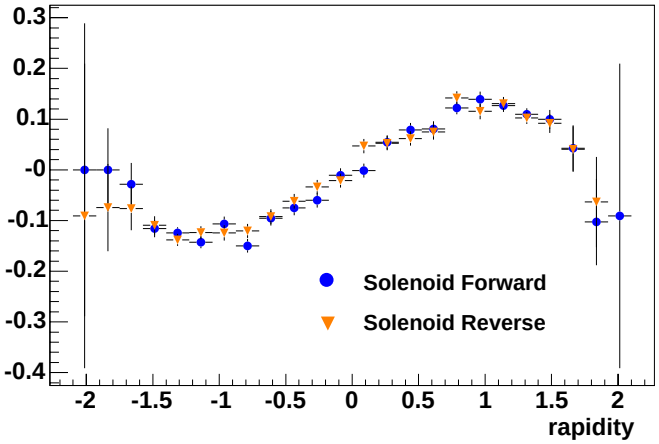

Figure 6.25: This shows the asymmetry distribution when the solenoid polarity is forward (blue circles) and when the solenoid polarity is reversed (orange triangles), independent of the toroid polarity.

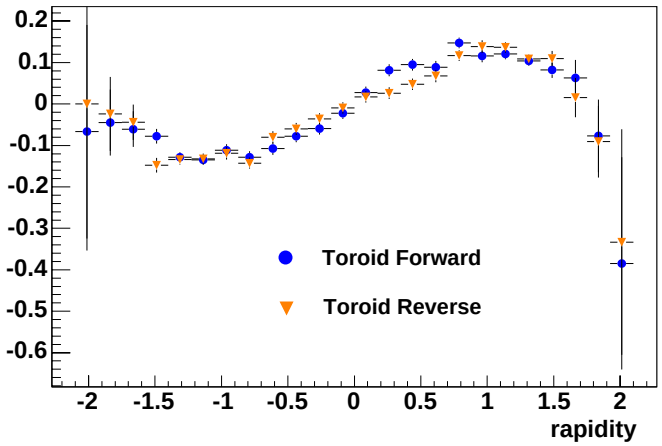

Figure 6.26: This shows the asymmetry distribution when the toroid polarity is forward (blue circles) and when the toroid polarity is reversed (orange triangles), independent of the solenoid polarity.

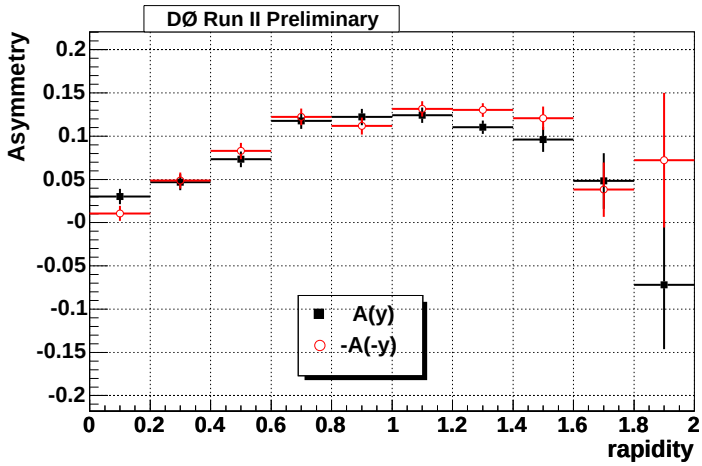

Figure 6.27: This plot shows the CP folded asymmetry. The square black data points represent $A(y)$ while the red open-circle data points represent $-A(-y)$.

6.3.2 CP folding

Since the initial parton collisions are CP invariant, we expect to see agreement when folding over the asymmetry distribution such that $A(y) = -A(-y)$. Any differences that might arise could be attributed to detector effects. Fig.6.27 shows the CP folded raw asymmetry distributions. The asymmetry in the negative rapidity region is rotated by π rads in order to compare it with the asymmetry in the forward rapidity region. A χ^2 probability of 0.528 with a $\chi^2/d.o.f.$ of 0.91 is obtained which indicates no major detector effects in rapidity.

CHAPTER 7

Backgrounds

This chapter covers the various sources of background and their estimated contribution to the data. The chapter also contains a description of the Monte Carlo that was used to estimate some of the backgrounds.

7.1 Monte Carlo Simulation using PMCS

The Monte Carlo samples used to estimate the electroweak backgrounds in this analysis ($Z \to \mu\mu$, $Z \to \tau\tau$ and $W \to \tau\nu$ decays where $\tau \to \mu$) are the same as those used in the $W \to \mu\nu$ cross section analysis [61]. The Monte Carlo events are first generated with the PYTHIA event generator [66] using the CTEQ6.1 PDF sets [67]. The detector resolution effects are then modeled using PMCS.

PMCS (Parameterized Monte Carlo Simulation) is based on parameterized physics processes and reconstruction, making it much faster than full detector simulation and reconstruction. It works by smearing certain objects like jets and muons to simulate the detector response. This smearing is done by tuning certain parameters to data collected by the DØ detector.

The reason that it is possible to use the same MC samples as are used in the $W \to \mu\nu$ cross section analysis is that almost the same selection cuts are used for this analysis and so should have the same efficiencies that go into PMCS. The exception is the isolation cut. Since the isolation variables are not modeled in PMCS and the isolation efficiency is applied only later as a correction to the p_T spectrum, it should not affect the Monte Carlo simulation. The systematics uncertainties arising from the use of the Monte Carlo events are described below.

Table 7.1: Summary of parameters used to smear p_T.

Parameter	Value with Uncertainty
A	0.00232 ± 0.00010
B	0.0258 ± 0.0008
C	0.995 ± 0.003

7.1.1 Tuning of PMCS

The effects of detector resolution on the p_T measurement are simulated using three parameters A, B and C, described in Equation 7.1. First the generated p_T is smeared using a gaussian with a width given by equation 7.1. Then the smeared p_T is scaled using Equation 7.2 [68].

$$\frac{\sigma_{1/p_T}}{1/p_T} = \sqrt{A^2 \frac{p_T^2}{L^4} + \frac{B^2}{L \sin\theta}} \tag{7.1}$$

$$p_T(scaled) = C \cdot \ p_T(smear) \tag{7.2}$$

A parameterizes the effect of the error in the measurement of individual hits in the tracker on the p_T resolution. This increase is directly proportional to p_T and inversely proportional to the normalized track bending lever arm (L). B parameterizes the effect of multiple scattering on the resolution. C parameterizes the imperfect description of the magnetic field in the reconstruction process and the energy loss due to matter when passing through the calorimeter.

The parameterization is the same as that described in reference [68], but the values of the parameters have been re-tuned to reflect the requirements made on the track quality by this analysis. It is assumed that the effect of multiple scattering on the p_T resolution is insensitive to the track quality requirements. The values of parameters A and C are tuned using a sample of $Z \to \mu\mu$ data, where the track quality cuts from the $W \to \mu\nu$ analysis have been applied. The values of A, B and C obtained from the tuning of PMCS in the $W \to \mu\nu$ analysis are shown in Table 7.1.

The parameterization of the missing energy resolution is almost the same as that used in the $W \to \ e\nu$ analysis (see reference [69] for details). The difference is the inclusion of

Table 7.2: Summary of parameters used to smear $\not\!\!E_T$.

Parameter	Value with Uncertainty
α	0.60 ± 0.02
β	0.05 ± 0.01
S	0.80 ± 0.20 GeV$^{\frac{1}{4}}$
U	3.02 ± 0.04 GeV

an additional term which is required to model the energy deposited by the muon in the calorimeter.

In the $W \rightarrow e\nu$ analysis the smeared $\not\!\!E_T$ is evaluated using the recoil jet, the smeared lepton, the generated $\not\!\!E_T$ and a term to simulate the effect of the underlying event.

The E_T of the recoil jet is smeared using the following parameterization,

$$E_T{}'_{recoil} = E_{T\,recoil} \cdot \alpha \tag{7.3}$$

$$\frac{\sigma_{E_T{}'_{recoil}}}{E_T{}'_{recoil}} = \sqrt{\beta^2 + \frac{S^2}{\sqrt{E_T{}'_{recoil}}}} \tag{7.4}$$

$$E_{T\,recoil}(smear) = E_T{}'_{recoil} + x \cdot \sigma_{E_T{}'_{recoil}} \tag{7.5}$$

where α is the hadronic energy scale[1], β and S are the constant and sampling terms for the hadronic calorimeter, and x is a random number with a gaussian distribution with mean 0 and rms 1.

The underlying event is simulated using a vector with random direction and a magnitude randomly distributed according to a gaussian of mean zero and width U.

All the parameters are taken from reference [69] and are summarized in Table 7.2.

The other $\not\!\!E_T$ component is the addition of the energy deposited by the muon as it passes through the calorimeter. This uses a simplified model of the calorimeter constructed by D. Hedin in Run I [2]. This models the energy that a muon is expected to deposit in the calorimeter. To get the transverse component, the energy is divided by $\cosh(\eta)$. The

[1] α is denoted the hadronic energy scale to keep consistency with the nomenclature used in reference [69]. However it is really an energy scale for the 'whole calorimeter'. Similarly β and S are the sampling and constant terms for the whole calorimeter.

[2] No reference has been determined for this as yet. The code is available in MuoCandidate.

quantity is then multiplied by a tunable parameter which represents a kind of 'MIP' energy scale and is called p.

To determine the value of p, the distribution of the W recoil along the direction of the muon, $u_{\parallel}$, is used. This variable integrates calorimeter quantities projected onto the direction of the muon and is therefore the most sensitive variable to any change in the MIP scale factor. The value of p is found to be 0.78 ± 0.02 by optimizing the agreement between data and PMCS in the distribution of $u_{\parallel}$ as shown in Fig. 7.1(a). The optimization of p is also performed using the $\not\!\!E_T$ distributions. This yields a different value of $p = 0.53 \pm 0.03$, as shown in Fig. 7.1(b). Since PMCS models the $u_{\parallel}$ distribution quite a bit better than the $\not\!\!E_T$ distribution, the value of p obtained from the optimization of $\not\!\!E_T$ is not taken as the central value but is instead used to assess the systematic uncertainty on p.

The difference $0.78 - 0.53 = 0.25$ is taken as a systematic error. This uncertainty is propagated to the W charge asymmetry by varying the value of $p = 0.78 \pm 0.25$ and re-evaluating the charge asymmetry. The systematic uncertainty due to the variation of p, for each bin in η, is listed in Table 8.5.

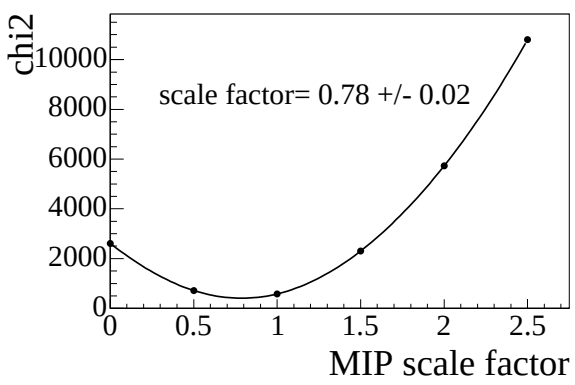

(a) χ^2 using the distribution of $u_{\parallel}$.

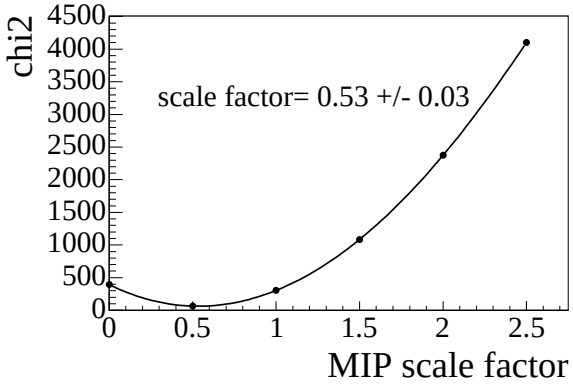

(b) χ^2 using the distribution of $\not\!\!E_T$.

Figure 7.1: χ^2 versus value of mip in data-PMCS comparison of $W \to \mu\nu$ data.

The smeared $\not\!\!E_T$ is then calculated using the following vector sum

$$\underline{\not\!\!E_T} = -\underline{p_{T\mu}} - \underline{E_{T recoil}}(smear) - \underline{E_{TU.E.}} - \underline{E_{TM.I.P.}} \tag{7.6}$$

where $\underline{p_{T\mu}}$ is the scaled p_T of the muon, $\underline{E_{T recoil}}(smear)$ is the smeared E_T of the recoil jet, $\underline{E_{TU.E.}}$ is the smeared E_T of the underlying event and $\underline{E_{TM.I.P.}}$ is the transverse energy deposited by the muon in the calorimeter.

Even though all the p_T and $\not\!\!E_T$ parameters used for tuning PMCS could possibly contribute to the systematic uncertainties, the parameter that is expected to provide the largest contribution is the hadronic energy scale, α. This was found to be true in the $W \to \mu\nu$ cross section analysis where all the $\not\!\!E_T$ smearing parameters were varied [61] to obtain a systematic uncertainty of 0.3% on the cross section. For the purpose of this analysis, 25K signal and 10K background Monte Carlo eventss were regenerated for each of the two triggers by varying α by $\pm 1\sigma$. The systematic uncertainty due to the variation of α, for each bin in η, is listed in Table 8.5.

7.2 Background Estimate

The largest source of contamination in the sample comes from electroweak backgrounds, $Z \to \mu\mu$, $W \to \tau\nu$ and $Z \to \tau\tau$ events. These backgrounds are estimated using Monte Carlo samples that were generated as described in Section 6. The other major source of contamination in the sample is from quarks that decay semi-leptonically. This is the multijet background (referred to as the 'QCD' background) and is estimated from data. In order to extract the amount of electroweak background contamination in the data sample using Monte Carlo, it is necessary to normalize the signal + background Monte Carlo to data from which the QCD background has been subtracted. 500K $W \to \mu\nu$ signal Monte Carlo events were generated for each of the two triggers and smeared for detector effects as described earlier. 102384 events from the "wide" MC sample and 117717 events from the "all" MC sample passed the selection cuts.

7.2.1 Electroweak Backgrounds

1. The largest source of background in the W sample comes from $Z \to \mu\mu$ events in which one of the muons has been poorly reconstructed or lies outside the detector

acceptance. The Z event then emulates a W event with one muon and $\not\!\!E_T$. The muon from a Z decay does not have a preferred direction as in the case of a muon from a W decay and this dilutes the asymmetry. It is hard to extract this background from data, so it is estimated using 200K $Z/\gamma \rightarrow \mu^+\mu^-$ ($M_{Z/\gamma^*} > 30$ GeV) events generated with PYTHIA and run through PMCS for each of the two triggers. The number of Z Monte Carlo events was scaled to the W signal Monte Carlo events using the SM ratio of the $Z \rightarrow \mu\mu$ to the $W \rightarrow \mu\nu$ cross section (0.092) and from the ratio of $Z/\gamma \rightarrow \mu^+\mu^-$ ($M_{Z/\gamma^*} > 30$ GeV) to $Z \rightarrow \mu^+\mu^-$ cross sections (1.30) [70]. 16239 events from the "wide" MC sample and 19057 events from the "all" MC sample passed the selection cuts.

2. $W \rightarrow \tau\nu$ events contribute to the contamination of the W sample when the τ decays to a muon and a neutrino. The muons from $W \rightarrow \tau$ decays have an inherent asymmetry of their own which tends to wash away the true asymmetry. Correcting for the backgrounds bin by bin in η takes care of the inherent τ asymmetry. This background is estimated using 200K $W \rightarrow \tau\nu$ Monte Carlo events generated separately for the two triggers. 1071 events from the "wide" MC sample and 1256 events from the "all" MC sample passed the selection cuts.

3. There is also a contribution from $Z \rightarrow \tau\tau$ events in which one of the τs decays to a muon. The contribution from this type of background is typically very small but again, due to the muon from the τ decay not having a preferred direction, the true asymmetry is diluted. This background is similarly estimated from 200K $Z \rightarrow \tau\tau$ Monte Carlo events (generated separately for the "wide" and the "all" triggers) which are normalized to the W sample just like the $Z \rightarrow \mu\mu$ sample. 742 events from the "wide" MC sample and 877 events from the "all" MC sample passed the selection cuts.

The same selection conditions applied to data (Section 2.3) are used on the smeared Monte Carlo samples to extract the number of events for each type of electroweak background. The background events were scaled to the signal MC events by a factor of 2.5 to account for the different sample sizes. As the isolation conditions are not modeled in PMCS, the isolation efficiency obtained in Section 4.6 is applied separately to reflect the isolation cuts applied to data. A random number between 0 and 100 was thrown. If the events had a transverse momentum that was greater than the random number, the event was discarded.

In addition, D. Hedin's toy calorimeter model is used to estimate the energy deposited by the μ when passing through the calorimeter and this energy is used to correct the $\not\!\!E_T$ in the Monte Carlo samples. Track quality conditions (hits in the SMT and CFT, χ^2 and the dca cut) are all applied when evaluating the efficiencies that are fed into PMCS and are not externally imposed on the Monte Carlo samples.

Table 7.4 gives the breakdown of the different electroweak backgrounds in the sample separately for the "wide" and "all" triggers.

7.2.2 QCD Background

The QCD or multijet background, arising from quarks that decay semi-leptonically into muons, is estimated from data using the Matrix Method. The Matrix Method is simply two simultaneous equations which are used to extract the number of signal and background events in the sample.

A sample of events N_1 is selected, using all the selection cuts described in Section 2.3, except the isolation cut. The isolation criteria efficiently reject QCD background events and are used as the discriminator. The selected N_1 events contain B number of background events and S number of signal events. The isolation cut is then applied, resulting in the selection of N_2 events which is a subset of N_1. The selected N_2 events is a combination of the number of signal and QCD background events which have passed the isolation cut.

$$N_1 = B + S, \tag{7.7}$$

$$N_2 = fB + \epsilon S, \tag{7.8}$$

where f is the efficiency for the background events to pass the isolation cut (or the fake rate) and ϵ is the efficiency for the signal events to pass the isolation cut (isolation efficiency). Solving the two equations we get the number of background events as

$$B = \frac{\epsilon N_1 - N_2}{\epsilon - f} \tag{7.9}$$

The isolation efficiency for signal events (0.9201 ± 0.022) was measured on a sample of $Z \rightarrow \mu\mu$ events in Section 4.6. The fake rate, or the isolation efficiency for background events, is obtained using low p_T data.

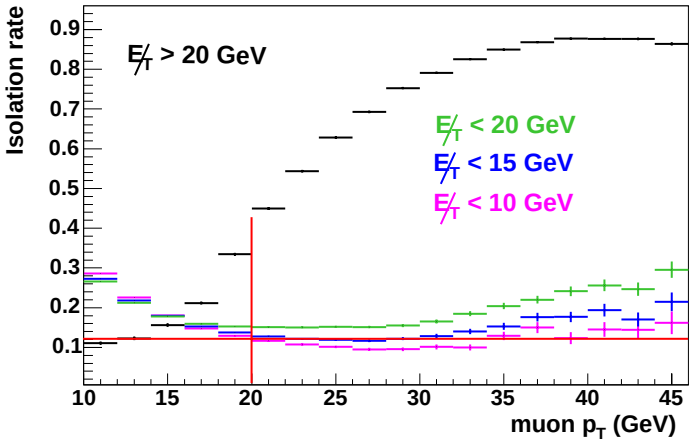

Figure 7.2: Probability for a single muon to pass the isolation cut as a function of p_T when $\not\!\!E_T > 20$ GeV ($M_T > 40$ GeV) and also when $\not\!\!E_T < 20$, 15 and 10 GeV (without any M_T cut).

Fake Rate

The fake rate, or the efficiency of the background to pass the isolation cut, is estimated using low p_T muons. The samples are selected by using all the selection cuts described in Section 2.3, except the cuts on p_T, $\not\!\!E_T$ and M_T, on the unskimmed data set. Fig. 7.2 shows the isolation rate (in black) as a function of the muon p_T when $\not\!\!E_T > 20$ GeV and $M_T > 40$ GeV. The isolation rate is 0.11 at $p_T = 10$ GeV ($p_T = 10$ GeV is the cut-off value for the single muon triggers used in this analysis). As p_T increases, the isolation condition is more efficient in rejecting background events and signal events are expected to dominate the sample. The fake rate is therefore not expected to increase with increasing p_T.

Fig. 7.2 also shows the isolation rates when $\not\!\!E_T < 20$, 15 and 10 GeV (but without any cut on the M_T). For low values of $\not\!\!E_T$, it is expected that the sample will be dominated by multijet events. This rate is not seen to increase by much in the p_T region where it is most likely that there might be a multijet contamination.

Fig. 7.3 shows the isolation rate as a function of the muon p_T fitted to a constant in the sample where $\not\!\!E_T < 10$ GeV. This sample is chosen because it should be well seperated from the signal sample. As the $\chi^2/d.o.f.$ of fit is rather large (> 5), an error larger than the error in the fit is assigned to the fake rate. The isolation rate for $p_T > 20$ GeV (selection condition

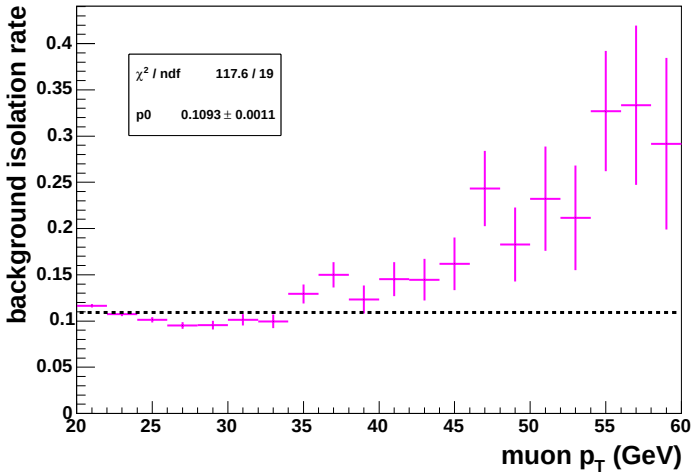

Figure 7.3: Probability for a single muon to pass the isolation cut as a function of p_T when $\not\!\!E_T < 10$ GeV.

for signal events in this analysis) when projected onto the y axis, has a mean value of 0.11 with an rms of 0.025. The mean is in good agreement with the value of fake rate obtained from the signal sample. The rms of this distribution is therefore chosen as the error in the fake rate.

Fig. 7.4 shows the isolation rate as a function of η when $\not\!\!E_T < 10$ GeV and $p_T > 20$ GeV. There appear to be no major fluctuations of the background isolation rate in η. The fake rate computed separately for positive and negative charges shows good agreement. The fake rate for the sample is therefore

$$f = 0.11 \pm 0.025. \tag{7.10}$$

The rms value of the isolation rate obtained from the QCD sample (with $\not\!\!E_T < 10$ GeV) is taken as the systematic error. This error is propagated to the systematic uncertainty for the asymmetry by varying the value of the fake rate by $\pm 1\sigma$. The systematic uncertainty due to the variation of the fake rate, for each bin in η, is listed in Table 8.5.

QCD background estimation

The amount of QCD background in the $W \to \mu\nu$ sample is estimated using the number of W events N_1 and N_2, with and without the isolation requirement. We then solve for the

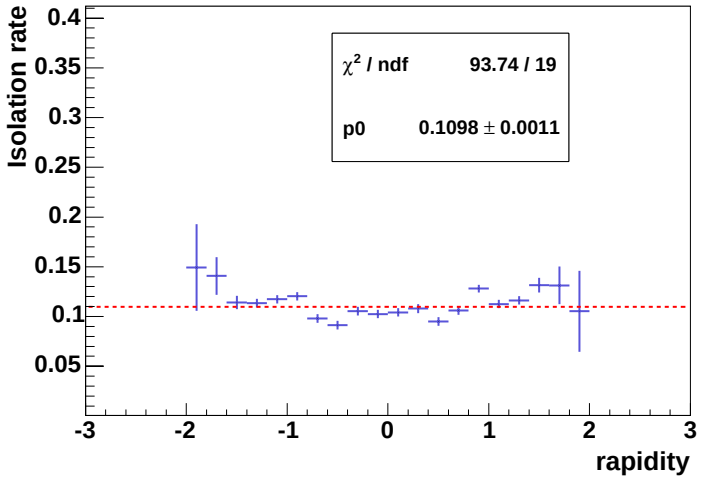

Figure 7.4: Probability for a single muon to pass the isolation cut as a function of rapidity when $\not\!\!E_T < 10$ GeV and $p_T > 20$ GeV with the charges separated out.

background using Eq. 19, bin by bin in η. The values of fake rate and isolation efficiency used are those that were evaluated earlier. The values obtained for the two different triggers for all of the data sample are summarized in Table 7.3.

Table 7.3: Summary of the QCD background estimation where f_{QCD} gives the fraction of QCD contamination in the $W \to \mu\nu$ data sample.

Variable	"wide" trigger	"all" trigger
N_1	248081	48720
N_2	187454	37048
ε	0.91±0.01	0.91±0.01
f	0.11±0.03	0.11±0.03
B	48920	9311
fB	5381	1024
f_{QCD}	0.0277±0.0004	0.0276±0.0009

Table 7.4: Summary of all estimated backgrounds in the W sample

Background	"wide" trigger	"all" trigger
$Z \rightarrow \mu\mu$	4.31 ± 0.05%	4.39 ± 0.11%
$Z \rightarrow \tau\tau$	0.19 ± 0.01%	0.20 ± 0.02%
$W \rightarrow \tau\nu$	2.32 ± 0.02%	2.43 ± 0.08%
QCD	2.77 ± 0.04%	2.76 ±0.09%

7.2.3 Total Background

Table 7.4 shows the breakdown of all the backgrounds for the two single muon triggers, in the sample used for this analysis. To get the number of events for each type of background for the analysis, all the electroweak backgrounds (with proper scaling) were added to the number of events obtained from the $W \rightarrow \mu\nu$ signal Monte Carlo sample and this sum was normalized to the total number of W events obtained from data minus the calculated QCD background for the sample. This normalization is done over the range $|\eta| < 1.6$ for events which fire the "wide" trigger and $|\eta| < 2.0$ for events which fire the "all" trigger. The errors in each background are also similarly scaled for each bin in η. The scaled background errors are quadratically added to the error in data to get the total statistical error for each bin in η.

Figs. 7.5 – 7.10 show the W transverse mass, muon p_T and $\not\!\!E_T$ distributions. These distributions show the comparison between data and the total expected sum of (signal + background) Monte Carlo + QCD background for the "wide" and "all" triggers. Figs. 7.11 – 7.14 show the same comparison in the case of positive and negative η distributions for the two triggers.

7.3 Combining of triggers

There are two single muon triggers used in this analysis, MUW_W_L2M3_TRK10 and MUW_A_L2M3_TRK10 (the "wide" and the "all" triggers) as defined in Section 2.2. The "wide" trigger covers the region $|\eta| < 1.5$ while the "all" trigger covers the region $|\eta| < 2.0$. In Section 7, Monte Carlo samples modeling signal and background have been separately generated for each trigger and smeared for detector effects using PMCS. The different

efficiencies fed into PMCS were evaluated using a bin width of 0.2 in η. To achieve the best possible agreement between data and Monte Carlo, the data were also binned using a bin width of 0.2 in η. Using the "all" trigger for $|\eta| < 1.4$ or the "wide" trigger for $|\eta| > 1.6$ provides no significant gain in statistics and is not considered worthwhile. Since the "wide" trigger only goes out to $|\eta| < 1.5$, events which fire the "all" trigger in the η bin $1.4 - 1.6$ were used. This results in some loss of statistics but the statistical uncertainty is still less than the errors that would arise due to the systematic uncertainties and from the scale factor if the two triggers were combined in this bin. The different prescales for the two triggers do not affect the asymmetry measurement when the two triggers are used in this way.

Table 8.2 and 8.3 gives a breakdown of the number of events for data and each type of background in bins of rapidity. This is shown separately for positive and negative muons.

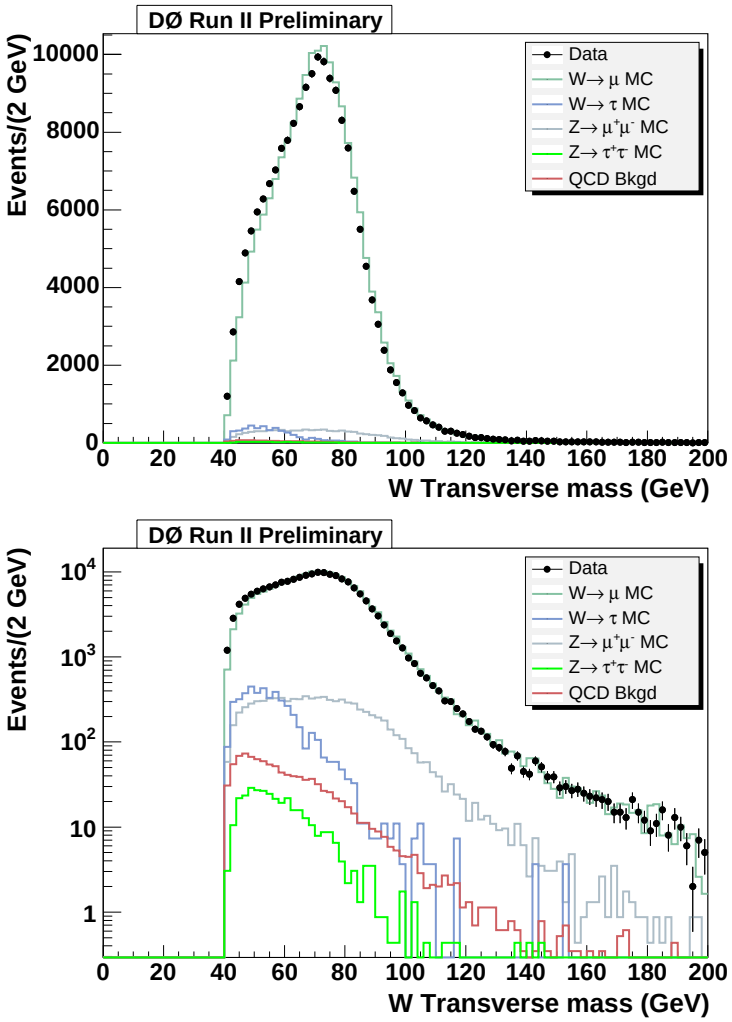

Figure 7.5: The W transverse mass (data and Monte Carlo) in linear scale (upper plot) and in log scale (lower plot) for the "wide" trigger. The $W \to \mu\nu$ MC line is the sum of $W \to \mu\nu$, $W \to \tau\nu$, $Z \to \mu\mu$, $Z \to \tau\tau$ and QCD.

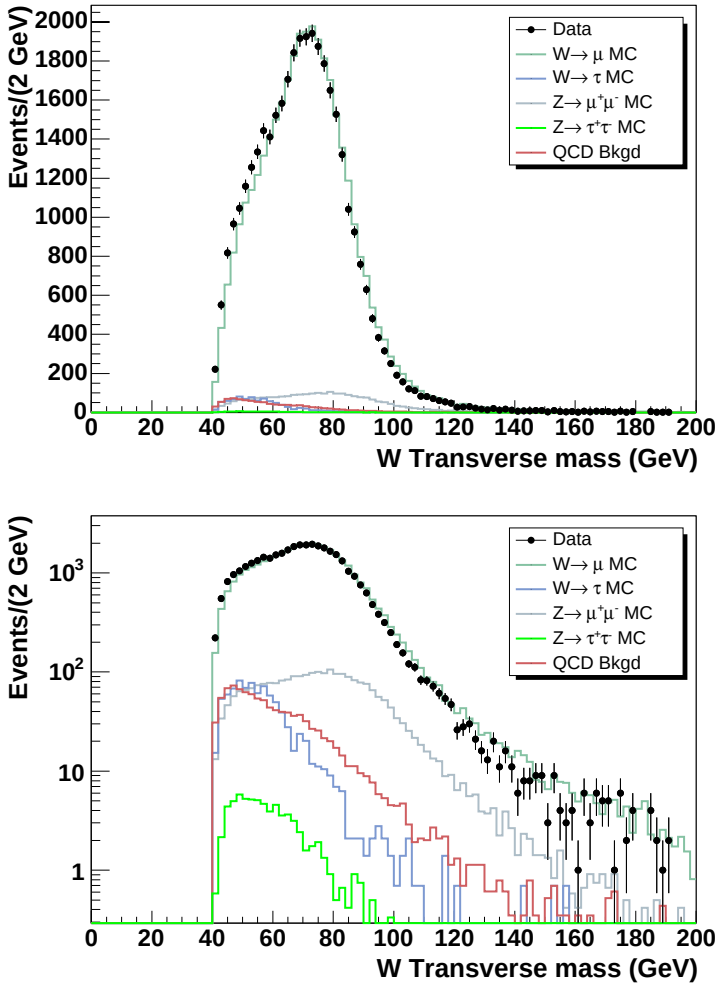

Figure 7.6: The W transverse mass (data and Monte Carlo) in linear scale (upper plot) and in log scale (lower plot) for the "all" trigger. The $W \to \mu\nu$ MC line is the sum of $W \to \mu\nu$, $W \to \tau\nu$, $Z \to \mu\mu$, $Z \to \tau\tau$ and QCD.

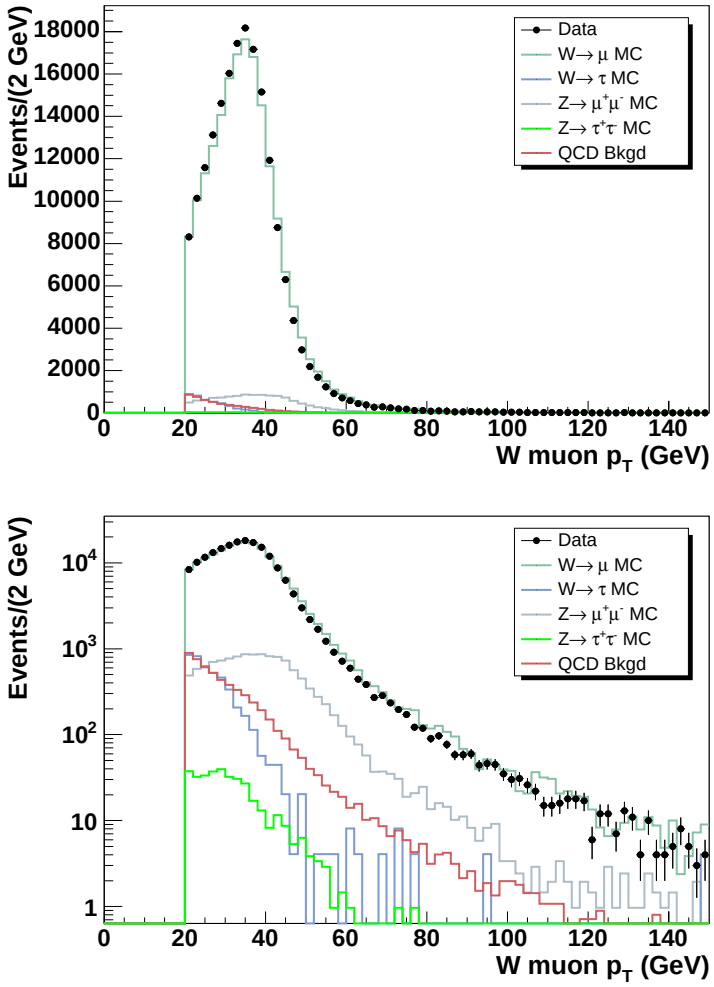

Figure 7.7: The muon p_T distribution (data and Monte Carlo) in linear scale (upper plot) and in log scale (lower plot) for the "wide" trigger. The $W \to \mu\nu$ MC line is the sum of $W \to \mu\nu$, $W \to \tau\nu$, $Z \to \mu\mu$, $Z \to \tau\tau$ and QCD.

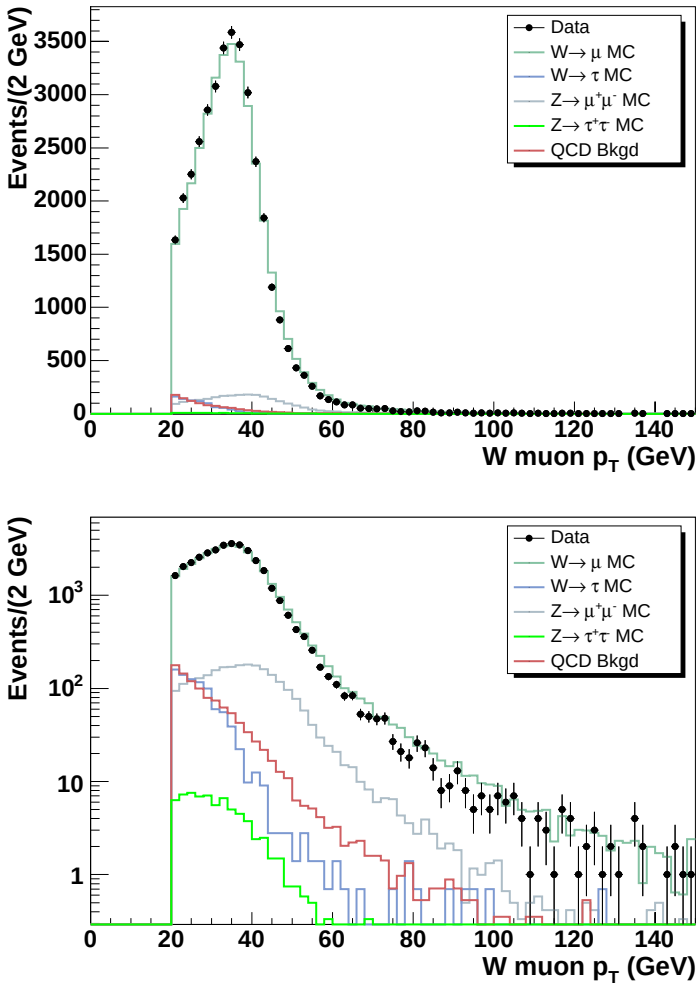

Figure 7.8: The muon p_T distribution (data and Monte Carlo) in linear scale (upper plot) and in log scale (lower plot) for the "all" trigger. The $W \rightarrow \mu\nu$ MC line is the sum of $W \rightarrow \mu\nu$, $W \rightarrow \tau\nu$, $Z \rightarrow \mu\mu$, $Z \rightarrow \tau\tau$ and QCD.

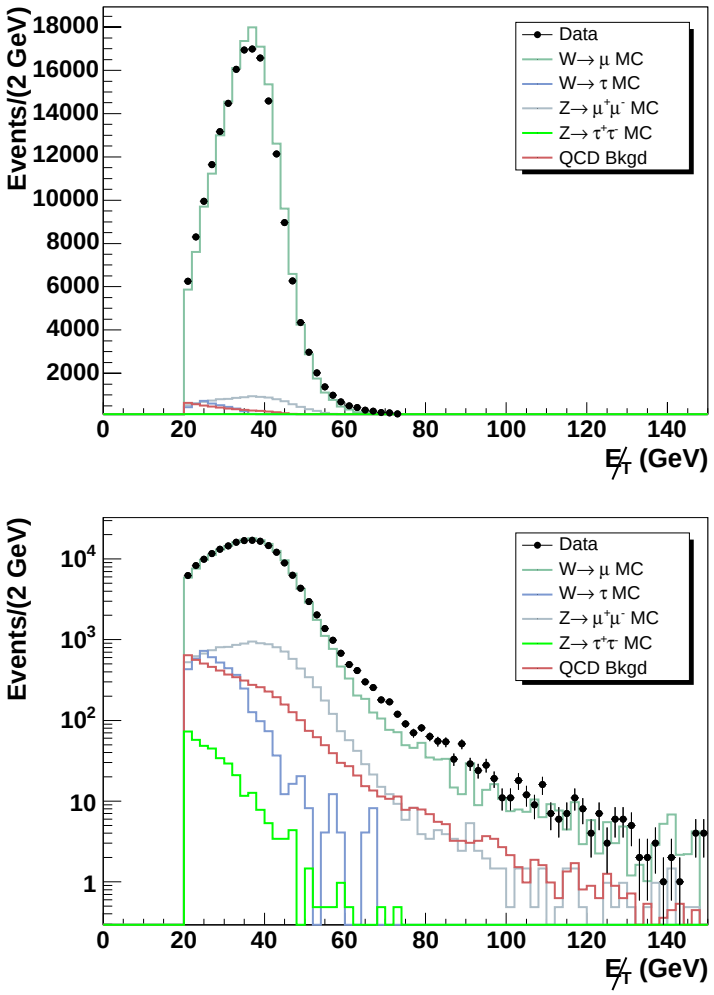

Figure 7.9: The $\not\!\!E_T$ distribution (data and Monte Carlo) in linear scale (upper plot) and in log scale (lower plot) for the "wide" trigger. The $W \to \mu\nu$ MC line is the sum of $W \to \mu\nu$, $W \to \tau\nu$, $Z \to \mu\mu$, $Z \to \tau\tau$ and QCD.

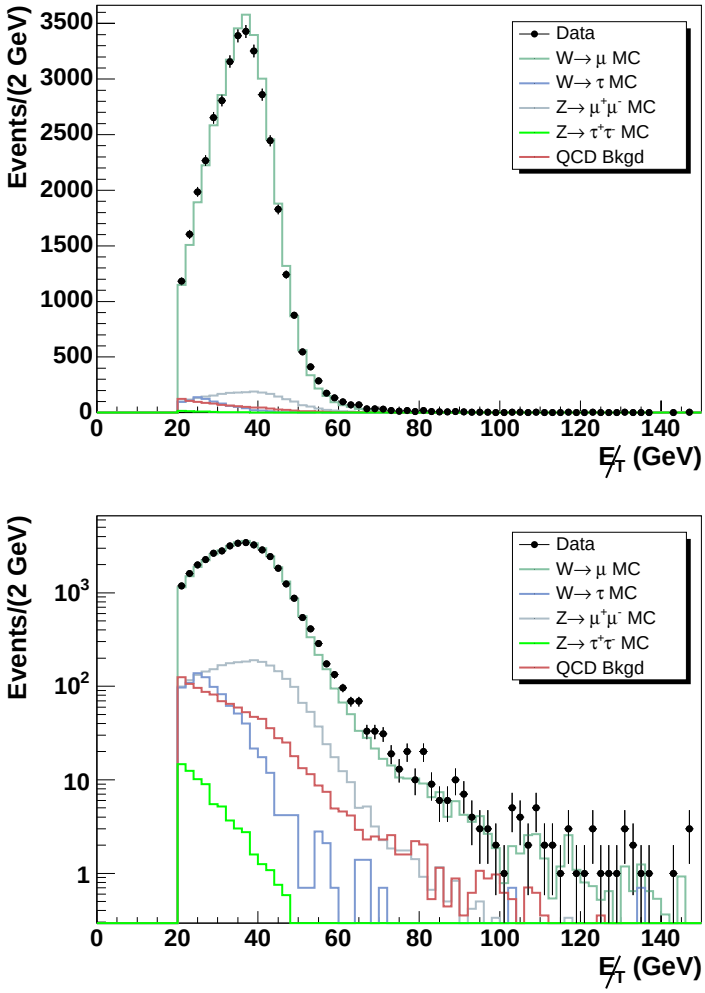

Figure 7.10: The $\not\!\!E_T$ distribution (data and Monte Carlo) in linear scale (upper plot) and in log scale (lower plot) for the "all" trigger. The $W \to \mu\nu$ MC line is the sum of $W \to \mu\nu$, $W \to \tau\nu$, $Z \to \mu\mu$, $Z \to \tau\tau$ and QCD.

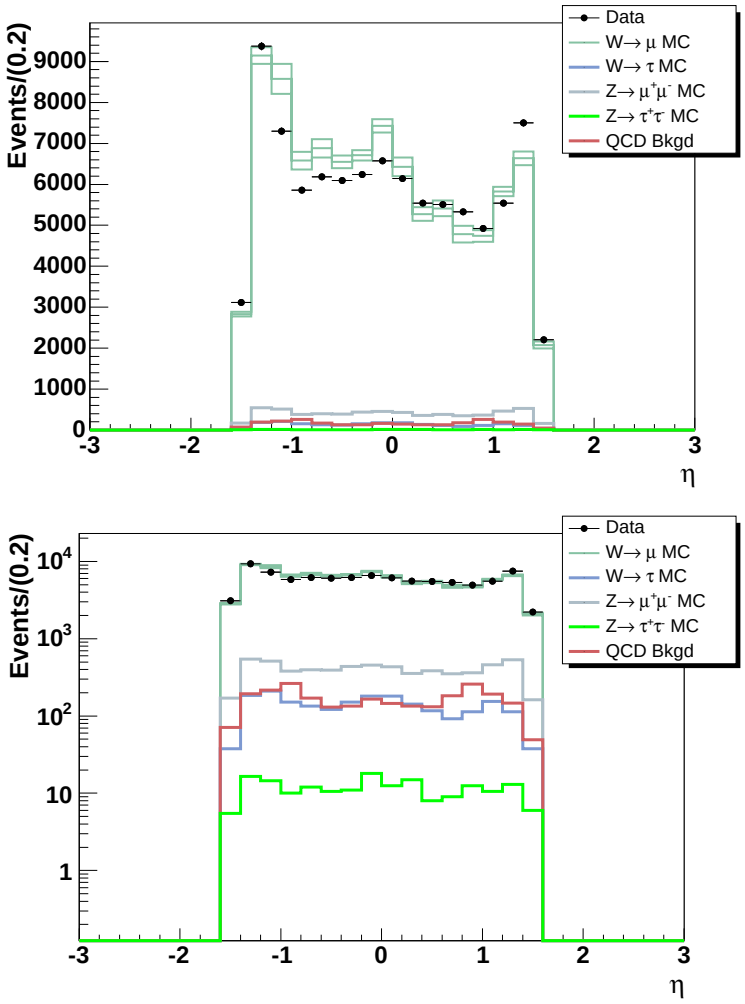

Figure 7.11: The η distribution for negative muons (data and Monte Carlo) in linear scale (upper plot) and in log scale (lower plot) for the "wide" trigger. The $W \to \mu\nu$ MC line is the sum of $W \to \mu\nu$, $W \to \tau\nu$, $Z \to \mu\mu$, $Z \to \tau\tau$ and QCD. Even though the full η distribution for the "wide" trigger is shown, only the events for $|\eta| < 1.4$ are used to evaluate the asymmetry. The error bands shown on the $W \to \mu\nu$ line are the PMCS uncertainties due to the statistics for the Z sample.

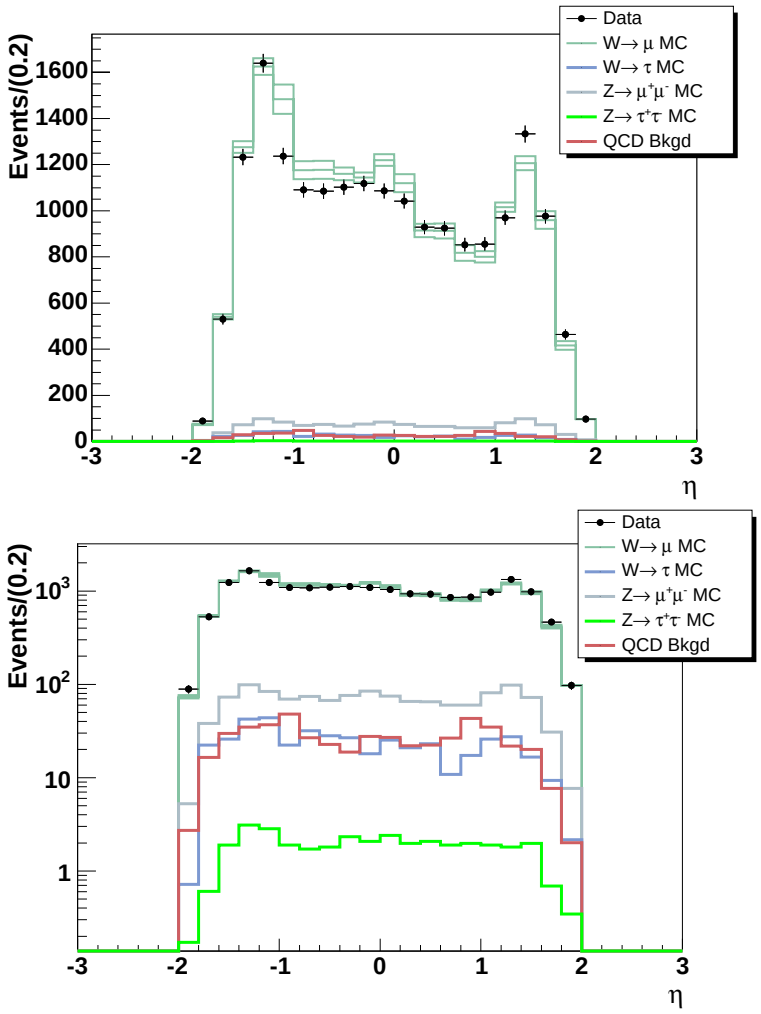

Figure 7.12: The η distribution for negative muons (data and Monte Carlo) in linear scale (upper plot) and in log scale (lower plot) for the "all" trigger. The $W \rightarrow \mu\nu$ MC line is the sum of $W \rightarrow \mu\nu$, $W \rightarrow \tau\nu$, $Z \rightarrow \mu\mu$, $Z \rightarrow \tau\tau$ and QCD. Even though the full η distribution for the "all" trigger is shown, only the events for $|\eta| > 1.4$ are used to evaluate the asymmetry. The error bands shown on the total expected plot are the PMCS uncertainties due to the statistics for the Z sample.

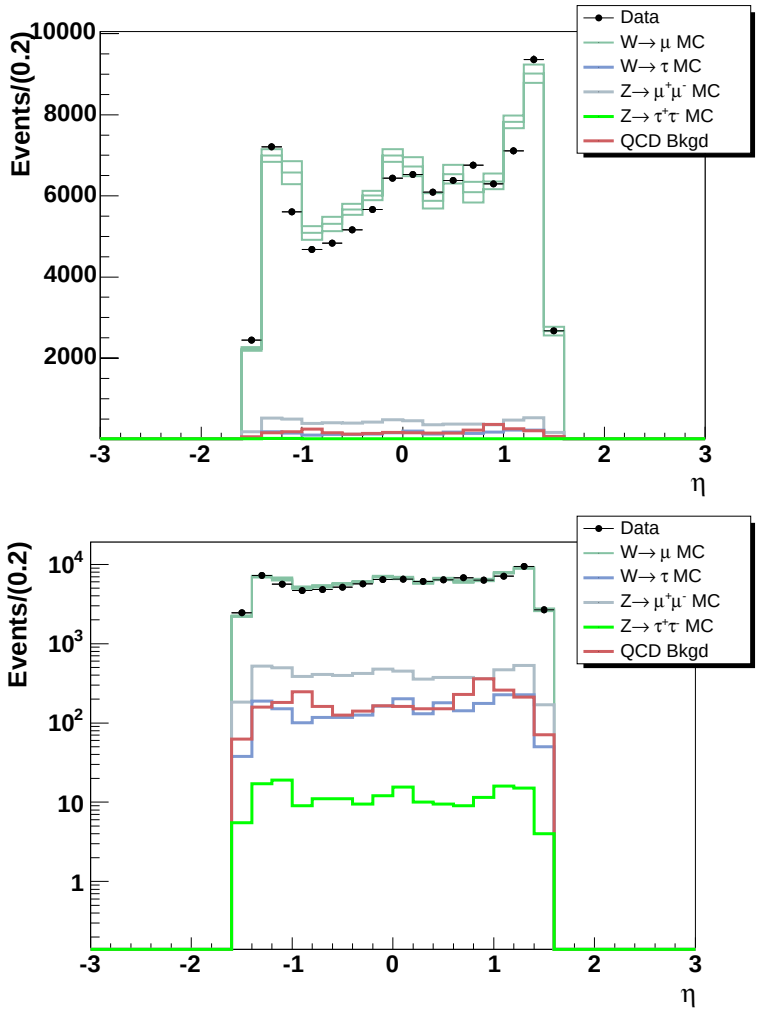

Figure 7.13: The η distribution for positive muons (data and Monte Carlo) in linear scale (upper plot) and in log scale (lower plot) for the "wide" trigger. The $W \rightarrow \mu\nu$ MC line is the sum of $W \rightarrow \mu\nu$, $W \rightarrow \tau\nu$, $Z \rightarrow \mu\mu$, $Z \rightarrow \tau\tau$ and QCD. Even though the full η distribution for the "wide" trigger is shown, only the events for $|\eta| < 1.4$ are used to evaluate the asymmetry. The error bands shown on the total expected plot are the PMCS uncertainties due to the statistics for the Z sample.

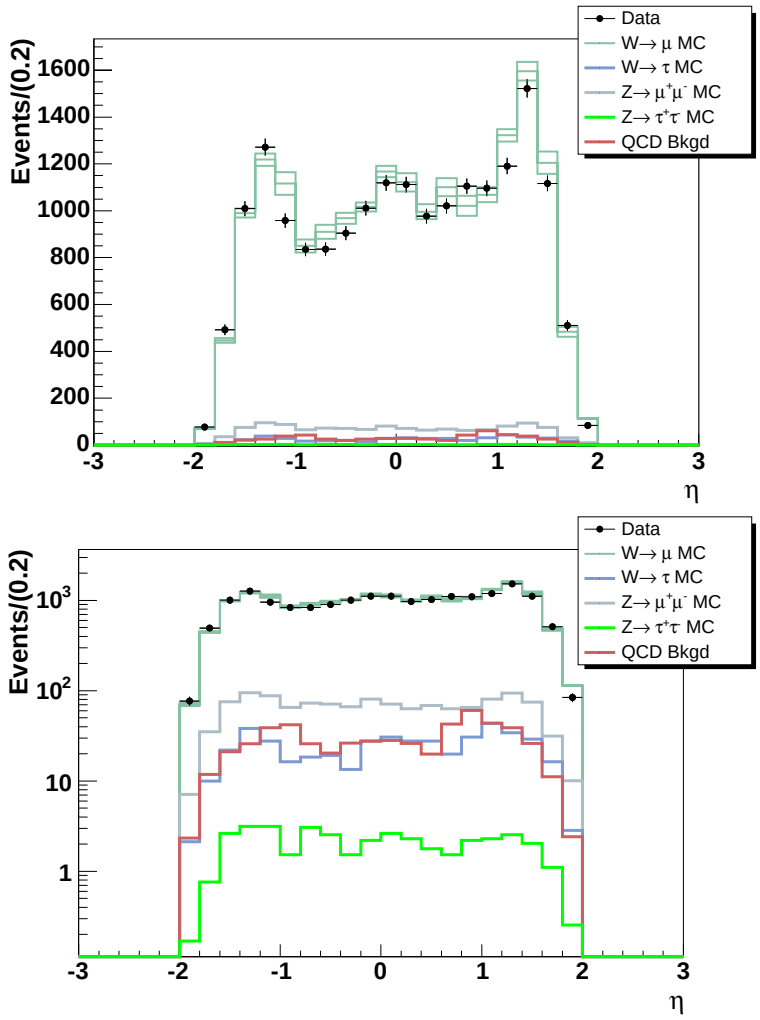

Figure 7.14: The η distribution for positive muons (data and Monte Carlo) in linear scale (upper plot) and in log scale (lower plot) for the "all" trigger. The $W \rightarrow \mu\nu$ MC line is the sum of $W \rightarrow \mu\nu$, $W \rightarrow \tau\nu$, $Z \rightarrow \mu\mu$, $Z \rightarrow \tau\tau$ and QCD. Even though the full η distribution for the "all" trigger is shown, only the events for $|\eta| > 1.4$ are used to evaluate the asymmetry. The error bands shown on the total expected plot are the PMCS uncertainties due to the statistics for the Z sample.

CHAPTER 8

Results and Conclusions

The muon charge asymmetry from the W decay is evaluated as a function of η using Equation 6. The asymmetry has been corrected for background effects on a bin-by-bin basis. Table 8.4 gives a breakdown of the asymmetry in bins of rapidity with the statistical and systematic uncertainties. Table 8.5 gives a breakdown of the different systematic uncertainties in bins of rapidity. Table 8.1 gives the final values for the asymmetry and the total uncertainties on these values.

The final results are shown in Fig. 8.1. The plot on top shows the asymmetry distribution which has been corrected for background effects. The yellow band shows the theoretical prediction for the W charge asymmetry at the parton level. This band was made using the NLO generator RESBOS-A and the CTEQ6.1M PDFs, with the 40 PDF error sets combined according to the recipe provided by the CTEQ collaboration [64]. The curve in red is the central value.

The plot on the bottom shows the folded asymmetry distribution with increased statistics. For this plot, the positive muons in the negative η bins were added to the negative muons in the positive η bins and vice versa. The results are compared to the theoretical predictions from the CTEQ6.1M PDFs (yellow band) and the MRST02 PDFs in blue. We see good agreement between the observed and the predicted asymmetry. These are the first results for the W charge asymmetry from DØ and the first for the muon channel at the Tevatron in Run II.

The charge asymmetry is sensitive to the d/u ratio of the quark momentum distribution in the proton over the range $0.005 < x < 0.3$. In addition to the previous measurements made at hadron colliders, this muon charge asymmetry measurement can help further constrain the PDFs, especially where the value of the calculated asymmetry deviates from the predicted

Table 8.1: Total uncertainties on the folded asymmetry in bins of rapidity.

Rapidity(l)	Rapidity(u)	asymmetry	total error
0.0	0.2	0.019	0.0076
0.2	0.4	0.049	0.0079
0.4	0.6	0.081	0.0080
0.6	0.8	0.126	0.0081
0.8	1.0	0.121	0.0083
1.0	1.2	0.133	0.0078
1.2	1.4	0.124	0.0072
1.4	1.6	0.114	0.0106
1.6	1.8	0.031	0.0213
1.8	2.0	-0.006	0.0484

asymmetry and has errors smaller than the PDF errors. More specifically, this measurement can help reduce the errors on some of the parameters that go into the PDFs and that are the most sensitive to this measurement. In addition, this measurement was made with a p_T cut for the muon lower than the p_T cut used in the electron analysis and hence probes a larger kinematic range..

The systematic uncertainty in the asymmetry due to the uncertainty in the Hadronic Energy Scale α can be reduced by running over larger Monte Carlo samples. This measurement is not yet systematics limited because the statistical uncertainties are greater than the systematic uncertainties in every bin by at least a factor of two. This bodes well for the future of this analysis as more data is collected by the DØ detector.

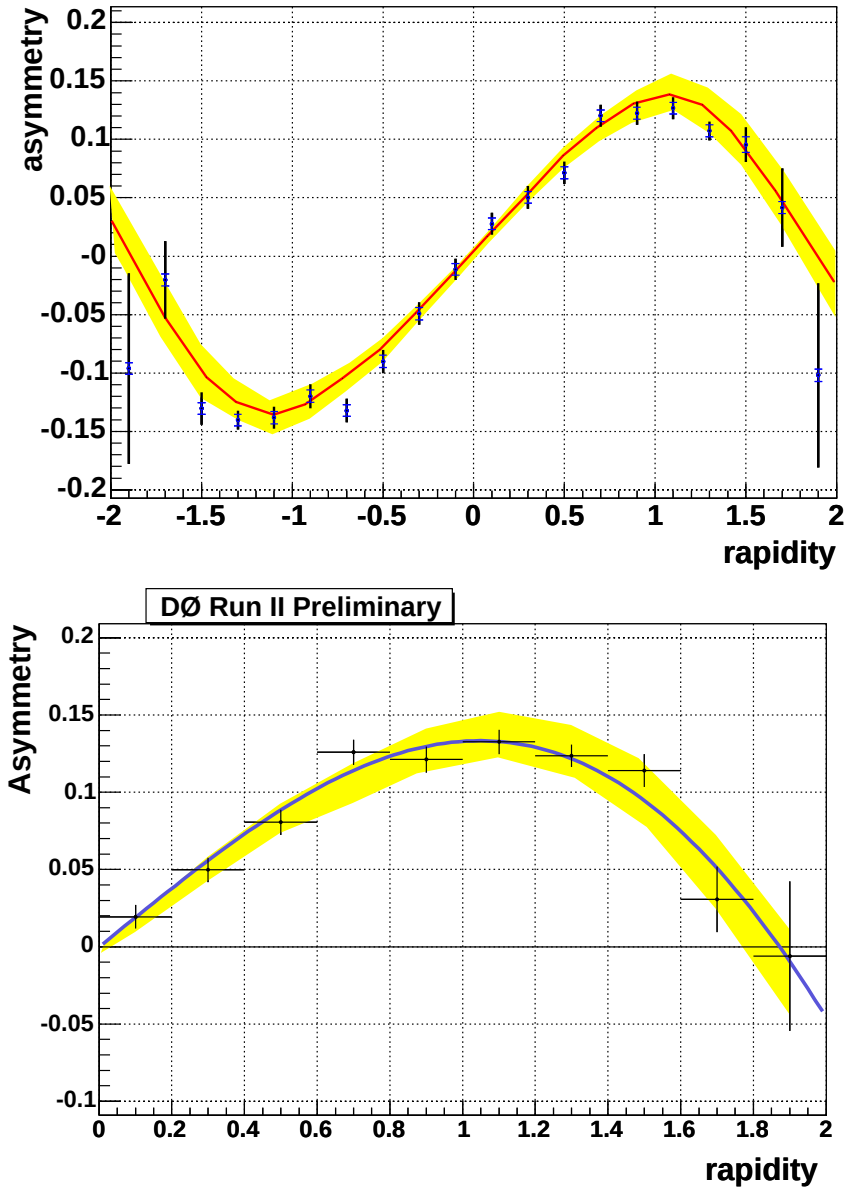

Figure 8.1: The top plot shows the corrected muon charge asymmetry distribution with the statistical errors in black and the systematic errors in blue. The yellow band is the envelope determined using the 40 CTEQ PDF error sets; the red line is the central value. The lower plot shows the corrected folded asymmetry with combined statistical and systematic uncertainties. The yellow band is the envelope determined using the 40 CTEQ PDF error sets while the blue curve is the charge asymmetry using the MRST02 PDFs.

Table 8.2: Data and background for negative muons in bins of rapidity. The errors on each background in each bin are statistical in nature.

Rap(l)	Rap(u)	data	$Z \to \mu\mu$	$W \to \tau\nu$	$Z \to \tau\tau$	QCD
-2.0	-1.8	89	3.84 ± 0.57	0.73 ± 0.73	0.17 ± 0.12	2.72 ± 1.65
-1.8	-1.6	531	26.3 ± 1.52	24.1 ± 4.20	0.69 ± 0.24	16.5 ± 4.06
-1.6	-1.4	1233	47.8 ± 2.04	28.5 ± 4.57	2.01 ± 0.42	29.8 ± 5.46
-1.4	-1.2	9371	364 ± 13.5	190 ± 28.40	13.1 ± 2.57	194 ± 13.9
-1.2	-1.0	7302	329 ± 12.9	224 ± 30.82	14.6 ± 2.72	216 ± 14.7
-1.0	-0.8	5855	257 ± 11.4	156 ± 25.75	9.10 ± 2.14	264 ± 16.2
-0.8	-0.6	6184	270 ± 11.6	139 ± 24.32	10.1 ± 2.26	171 ± 13.1
-0.6	-0.4	6093	250 ± 11.2	127 ± 23.19	7.58 ± 1.95	131 ± 11.4
-0.4	-0.2	6240	274 ± 11.7	161 ± 26.10	9.10 ± 2.14	134 ± 11.5
-0.2	0.0	6576	275 ± 11.7	186 ± 28.08	13.1 ± 2.57	165 ± 12.8
0.0	0.2	6142	263 ± 11.5	182 ± 27.76	10.1 ± 2.26	146 ± 12.1
0.2	0.4	5545	217 ± 10.5	152 ± 25.40	13.6 ± 2.62	134 ± 11.6
0.4	0.6	5506	234 ± 10.8	123 ± 22.80	6.07 ± 1.75	131 ± 11.4
0.6	0.8	5333	236 ± 10.9	97.4 ± 20.31	7.08 ± 1.89	182 ± 13.5
0.8	1.0	4924	238 ± 10.9	114 ± 22.01	11.6 ± 2.42	257 ± 16.0
1.0	1.2	5541	314 ± 12.6	156 ± 25.75	10.6 ± 2.31	192 ± 13.8
1.2	1.4	7503	364 ± 13.5	114 ± 22.01	11.6 ± 2.42	147 ± 12.1
1.4	1.6	976	48.5 ± 2.05	17.5 ± 3.58	2.09 ± 0.42	20.0 ± 4.47
1.6	1.8	464	21.9 ± 1.38	9.51 ± 2.63	0.69 ± 0.24	7.67 ± 2.76
1.8	2.0	97	4.98 ± 0.66	2.19 ± 1.27	0.35 ± 0.17	2.00 ± 1.41

Table 8.3: Data and background for positive muons in bins of rapidity. The errors on each background in each bin are statistical in nature.

Rap.(l)	Rap.(u)	data	$Z \to \mu\mu$	$W \to \tau\nu$	$Z \to \tau\tau$	QCD
-2.0	-1.8	77	5.08 ± 0.66	2.16 ± 1.25	0.17 ± 0.12	2.34 ± 1.53
-1.8	-1.6	492	24.5 ± 1.45	10.1 ± 2.70	0.69 ± 0.24	11.8 ± 3.43
-1.6	-1.4	1009	48.2 ± 2.03	22.3 ± 4.02	2.41 ± 0.45	21.1 ± 4.59
-1.4	-1.2	7211	353 ± 13.4	194 ± 28.69	14.2 ± 2.67	159 ± 12.6
-1.2	-1.0	5605	316 ± 12.6	156 ± 25.73	16.6 ± 2.90	181 ± 13.4
-1.0	-0.8	4678	256 ± 11.4	105 ± 21.15	7.58 ± 1.95	246 ± 15.7
-0.8	-0.6	4837	261 ± 11.5	118 ± 22.39	9.09 ± 2.14	161 ± 12.6
-0.6	-0.4	5160	250 ± 11.2	118 ± 22.39	10.1 ± 2.26	126 ± 11.2
-0.4	-0.2	5661	245 ± 11.1	135 ± 23.94	8.59 ± 2.08	141 ± 11.8
-0.2	0.0	6437	288 ± 12.1	169 ± 26.76	10.6 ± 2.31	165 ± 12.8
0.0	0.2	6524	280 ± 11.8	211 ± 29.92	14.1 ± 2.67	162 ± 12.7
0.2	0.4	6088	232 ± 10.8	135 ± 23.93	9.60 ± 2.20	151 ± 12.3
0.4	0.6	6376	241 ± 11.0	190 ± 28.38	9.60 ± 2.20	151 ± 12.3
0.6	0.8	6754	249 ± 11.2	144 ± 24.67	8.08 ± 2.02	229 ± 15.1
0.8	1.0	6295	237 ± 10.9	182 ± 27.75	11.6 ± 2.42	362 ± 19.0
1.0	1.2	7114	328 ± 12.8	228 ± 31.09	15.6 ± 2.81	260 ± 16.1
1.2	1.4	9364	389 ± 14.0	233 ± 31.38	13.6 ± 2.62	212 ± 14.5
1.4	1.6	1117	49.2 ± 2.06	28.8 ± 4.56	1.81 ± 0.39	26.0 ± 5.10
1.6	1.8	511	21.3 ± 1.35	16.6 ± 3.46	0.95 ± 0.28	11.1 ± 3.33
1.8	2.0	84	7.15 ± 0.78	2.88 ± 1.44	0.26 ± 0.15	2.41 ± 1.55

Table 8.4: Statistical and systematic uncertainties on the asymmetry in bins of rapidity.

Rapidity(l)	Rapidity(u)	asymmetry	statistical uncertainty	systematic uncertainty
−2.0	−1.8	−0.096	0.0816	0.0050
−1.8	−1.6	−0.020	0.0332	0.0052
−1.6	−1.4	−0.130	0.0139	0.0050
−1.4	−1.2	−0.140	0.0081	0.0049
−1.2	−1.0	−0.138	0.0092	0.0052
−1.0	−0.8	−0.120	0.0103	0.0053
−0.8	−0.6	−0.132	0.0099	0.0051
−0.6	−0.4	−0.090	0.0098	0.0053
−0.4	−0.2	−0.049	0.0096	0.0053
−0.2	0.0	−0.011	0.0092	0.0050
0.0	0.2	0.028	0.0093	0.0050
0.2	0.4	0.050	0.0097	0.0050
0.4	0.6	0.071	0.0096	0.0051
0.6	0.8	0.120	0.0095	0.0050
0.8	1.0	0.122	0.0100	0.0050
1.0	1.2	0.127	0.0094	0.0050
1.2	1.4	0.107	0.0080	0.0051
1.4	1.6	0.095	0.0149	0.0067
1.6	1.8	0.041	0.0336	0.0051
1.8	2.0	−0.102	0.0789	0.0053

Table 8.5: Breakdown of the systematic uncertainties by bins of rapidity.

Rap(l)	Rap(u)	Eff ratio k	Isolation eff	'MIP' val p	fake rate	H.E.S. α	charge misid
-2.0	-1.8	0.0050	0.0002	0.0006	0.0001	0.0003	0.0005
-1.8	-1.6	0.0049	0.0003	0.0003	0.0011	0.0011	0.0005
-1.6	-1.4	0.0047	0.0006	0.0006	0.0004	0.0003	0.0005
-1.4	-1.2	0.0048	0.0002	0.0004	0.0002	0.0007	0.0005
-1.2	-1.0	0.0048	0.0016	0.0003	0.0001	0.0001	0.0005
-1.0	-0.8	0.0049	0.0003	0.0002	0.0001	0.0010	0.0001
-0.8	-0.6	0.0049	0.0008	0.0007	0.0008	0.0002	0.0001
-0.6	-0.4	0.0049	0.0005	0.0003	0.0004	0.0012	0.0001
-0.4	-0.2	0.0050	0.0003	0.0001	0.0005	0.0011	0.0001
-0.2	0.0	0.0051	0.0002	0.0004	0.0001	0.0003	0.0001
0.0	0.2	0.0051	0.0007	0.0003	0.0001	0.0005	0.0001
0.2	0.4	0.0050	0.0001	0.0003	0.0001	0.0003	0.0001
0.4	0.6	0.0049	0.0004	0.0002	0.0001	0.0004	0.0001
0.6	0.8	0.0047	0.0006	0.0005	0.0001	0.0015	0.0001
0.8	1.0	0.0049	0.0005	0.0002	0.0007	0.0012	0.0001
1.0	1.2	0.0048	0.0002	0.0002	0.0002	0.0001	0.0005
1.2	1.4	0.0051	0.0005	0.0002	0.0004	0.0005	0.0005
1.4	1.6	0.0050	0.0010	0.0005	0.0005	0.0045	0.0005
1.6	1.8	0.0050	0.0002	0.0001	0.0008	0.0002	0.0005
1.8	2.0	0.0051	0.0011	0.0006	0.0013	0.0003	0.0005

APPENDIX A

Efficiency Error Calculation

The following macro was used to evaluate the errors on efficiencies.

```
// This macro implements functions for calculating Bayesian
// uncertainties on efficiencies, important for efficiencies near 0 or
// 1.  See also CDF-5894 ("Efficiency Uncertainties: A Bayesian
// Prescription") by John Conway for more details.
//
// Jason Nielsen and Lauren Tompkins (LBNL/Berkeley), Jan 9, 2003
//
// How to use this code in ROOT:
// root [0] .L $ROOTSYS/lib/libPhysics.so
// root [1] .L bayesianUncertainties.C
// root [2] error(323,324);

void BayesianError(Double_t n, Double_t N, Double_t& plusSig, Double_t& minusSig)
{
  Double_t central = n/N;
  Double_t div = 0.000001;
  Double_t end1 = 0;
  end1 = central-div;
  Double_t end2 =0;
  end2 =  central+div;
  Double_t sum = 0;
```

```
Double_t sum1 = 0;
Double_t sum2 = 0;
Double_t teps = 0.;
Double_t temp = 0;
Double_t centralsum = 0;
Double_t oldend1 = 0.;
Double_t oldend2 = 0.;
Int_t nn = (Int_t) n;
Int_t NN = (Int_t) N;

centralsum = instvalue(central, N,n) * div;

Double_t totalsum = 0;

if (NN != nn) {
  sum1 = centralsum*pow((end1/central),nn)*pow(((1-end1)/(1-central)),(NN-nn));
  sum2 = centralsum*pow((end2/central),nn)*pow(((1-end2)/(1-central)),(NN-nn));
} else {
  sum1 = centralsum * pow((end1/central),nn);
  sum2 = centralsum * pow((end2/central),nn);
}

while(sum < .6827){
  if (sum1 >= sum2) {
    centralsum += sum1;
    oldend1 = end1;
    end1 = end1 - div;
    if (end1 > 0) {
      sum1 = sum1 * pow((end1/oldend1),nn)*pow(((1-end1)/(1-oldend1)),(NN-nn));
    } else {
      sum1 = 0.;
    }
```

```
    } else if (sum1 < sum2) {
      centralsum += sum2;
      oldend2 = end2;
      end2 = end2 + div;
      if (end2 < 1) {
        sum2 = sum2*pow((end2/oldend2),nn)*pow(((1-end2)/(1-oldend2)),(NN-nn));
      } else {
        sum2 = 0.;
      }
    }
    sum = centralsum;
  }
  std::cout << "Eff is " << central << "(+" << end2-central << ")(-"
void BayesianError(Double_t n, Double_t N, Double_t& plusSig, Double_t& minusSig)
{
  Double_t central = n/N;
  Double_t div = 0.000001;
  Double_t end1 = 0;
  end1 = central-div;
  Double_t end2 =0;
  end2 =  central+div;
  Double_t sum = 0;
  Double_t sum1 = 0;
  Double_t sum2 = 0;
  Double_t teps = 0.;
  Double_t temp = 0;
  Double_t centralsum = 0;
  Double_t oldend1 = 0.;
  Double_t oldend2 = 0.;
  Int_t nn = (Int_t) n;
  Int_t NN = (Int_t) N;
```

```
centralsum = instvalue(central, N,n) * div;

Double_t totalsum = 0;

if (NN != nn) {
  sum1 = centralsum*pow((end1/central),nn)*pow(((1-end1)/(1-central)),(NN-nn));
  sum2 = centralsum*pow((end2/central),nn)*pow(((1-end2)/(1-central)),(NN-nn));
} else {
  sum1 = centralsum * pow((end1/central),nn);
  sum2 = centralsum * pow((end2/central),nn);
}

while(sum < .6827){
  if (sum1 >= sum2) {
    centralsum += sum1;
    oldend1 = end1;
    end1 = end1 - div;
    if (end1 > 0) {
      sum1 = sum1 * pow((end1/oldend1),nn)*pow(((1-end1)/(1-oldend1)),(NN-nn));
    } else {
      sum1 = 0.;
    }
  } else if (sum1 < sum2) {
    centralsum += sum2;
    oldend2 = end2;
    end2 = end2 + div;
    if (end2 < 1) {
      sum2 = sum2*pow((end2/oldend2),nn)*pow(((1-end2)/(1-oldend2)),(NN-nn));
    } else {
      sum2 = 0.;
    }
  }
```

```
    sum = centralsum;
  }
  std::cout << "Eff is " << central << "(+" << end2-central << ")(-"
            << central-end1 << ")." << std::endl;

  plusSig = end2 - central;
  minusSig = central - end1;

  return;
}

Double_t instvalue(Double_t eps,Double_t N,Double_t n)
{
  Double_t coeff = N + 1;
  Double_t a = 1.0;

  if (N-n< n){
    for(int i= 0; i <n; i ++){
      if(i < N-n) a = (1-eps);
      if(i >= N-n) a = 1;
      coeff *= (N-i)/(n-i)*(eps)*(a);
    }
  }
  if (N-n > n){
    for(int i= 0; i <n; i ++){
      coeff *= (N-i)/(n-i)*(eps)*(1-eps);
    }
    for(int j = 0; j <(N-2*n); j++){
      coeff *= (1-eps);
    }
  }
  if (eps > 1. || eps < 0.) {
```

```
    return 0.;
  } else {
    return coeff;
  }
}

void BinoError(Double_t n, Double_t N, Double_t& Sig)
{
  double eff = n/N;
  double var = sqrt(eff*(1.0-eff)/N);

  Sig = var;

  return;
}
```

REFERENCES

[1] D. J. Gross and F. Wilczek, Phys. Rev. Lett. **30**, 1343 (1973).

[2] H. D. Politzer, Phys. Rev. Lett. **30**, 1346 (1973).

[3] S. Weinberg, Phys. Rev. Lett. **19**, 1264 (1967).

[4] S. Glashow, Nucl. Phys. **22**, 579 (1961).

[5] A. Salam, in Elementary Particle Theory, the Nobel Symposium no 8, edited by N. Svartholm (Almqzist and Wiksell, Stockholm, 1968), p.367 (1968).

[6] Particle Data Group, Review of Particle Physics, "Particle Physics B," **592,** 246 (2004).

[7] K. Kodama *et.al.* "Observation of tau neutrino interactions," Phys. Lett. B **504**, 218 (2001).

[8] E. D. Bloom *et al.*, Phys. Rev. Lett. **23**, 930 (1969); J. D. Bjorken and E. A. Paschos, Phys. Rev. **185**, 1975 (1969)

[9] S. Chekanov *et al.* [ZEUS Collaboration], Phys. Rev. D **67**, 012007 (2003); C. Adloff *et al.* [H1 Collaboration], Eur. Phys. J. C **30**, 1 (2003).

[10] Barger and Phillips, "Collider Physics."

[11] G.Sterman *et al.*"Handbook of perturbative QCD"

[12] http://www.phys.psu.edu/c̃teq/

[13] http://durpdg.dur.ac.uk/hepdata/mrs.html

[14] http://durpdg.dur.ac.uk/hepdata/grv.html

[15] J. Pumplin *et al.*, "New Generation of Parton Distributions with Uncertainties from Global QCD Analysis", hep-ph/0201195.

[16] Peskin and Schroeder, "An Introduction to Quantum Field Theory."

[17] Tevatron Electroweak Working Group, "Combination of CDF and DØ Results on the W-Boson Width," hep-ex/0510077.

[18] Benner *et al.*, Phys. Lett. B **122**, 476 (1983)

[19] R. Hamberg *et al.*, Nucl. Phys. B **359**, 343 (1991).

[20] E. L. Berger, F. Halzen, C. S. Kim and S. Willenbrock, Phys. Rev. D **40**, 83 (1989); A. D. Martin, R. G. Roberts and W. J. Stirling, Mod. Phys. Lett. A **4**, 1135 (1989).

[21] L. Whitlow *et al.*, Phys. Lett. B **282**, 475 (1992); M. Arneodo*et al.*, Phys. Lett. B **309**, 222 (1993); M. Virchaux and M. Milsztajn, Phys. Lett. B **274**, 221 (1992).

[22] B. Badelek, Nucl. Phys. B **370**, 278 (1992).

[23] F. Abe *et al.*, Phys. Rev. Lett. **68**, 10 (1992).

[24] F. Abe *et al.*, Phys. Rev. Lett. **68**, 10 (1992).

[25] F. Abe *et al.*, Phys. Rev. Lett. **74**, 850 (1995).

[26] F. Abe *et al.*, Phys. Rev. Lett. **81**, 5754 (1998).

[27] D. Acosta *et al.*, Phys. Rev. D **71**, 051104 (2005).

[28] A. M. Narayanan, "Measurement of the charge asymmetry of muons from W boson decay at the DØ detector," FERMILAB-THESIS-1997-58.

[29] J. Torborg, "The Charge Asymmetry in W bosons produced in $p\bar{p}$ collisions," Ph.D. Thesis, Notre Dame (2005).

[30] Joey Thompson, "Introduction to Colliding Beams at Fermilab," available at "http://www-spires.fnal.gov/spires/find/hep/www?r=fermilab-tm-1909"

[31] Fermilab Beam Division, "Fermilab's Chain of Accelerators," available at "http://www-bd.fnal.gov/public/chain.html"

[32] B. M. Evanger *et al.*, "Concepts Rookie Book," available at "http://beamdocs.fnal.gov/DocDB/0010/001023/001/Concepts%20Rookie%20Book%20v3.pdf"

[33] B. W. Worthel, "Booster Rookie Book," available at "http://beamdocs.fnal.gov/DocDB/0010/001022/001/Booster%20V3_0.pdf"

[34] J. P. Morgan *et al.*, "Pbar Rookie Book," available at "http://beamdocs.fnal.gov/DocDB/0010/001021/001/Pbar%20Rookie%20Book.pdf"

[35] V. Abazov *et al.*, DØ Collaboration, "The Upgraded DØ Detector," submitted to Nucl. Instr. Methods.

[36] DØ Collaboration, "DØ Silicon Tracker Technical Design Report," DØ Note 2169, (1994).

[37] D. Adams *et al.*, "Central Fiber Tracker Technical Design Report," DØ Note 4164, (1999).

[38] M. Adams *et al.*, "Design Report of the Central Preshower Detector for the DØ Upgrade," DØ Note 3014, (1996).

[39] DØ Collaboration, "The DØ Upgrade: Forward Preshower, Muon System and Level 2 Trigger," DØ Note 2894, (1996).

[40] J. Kotcher, "Design, Performance, and Upgrade of the DØ Calorimeter," Fermilab Conf-95/007-E, (1995).

[41] K. De *et al.*, "Technical Design Report for the Upgrade of the ICD for DØ Run II," DØ Note 2686, (1997).

[42] H. T. Diehl *et al.*, "Technical Design of the Central Muon System," DØ Note 3365, (1997).

[43] G. Alexeev *et al.*, "Technical Design Report of the DØ Forward Muon Tracking Detector Based on Mini-drift Tubes," DØ Note 3366, (1997).

[44] A. Lo, C. Miao, and R. Partridge, "Luminosity Monitor Technical Design Report," DØ Note 3320, (1997).

[45] H. Evans *et al.*, "A Silicon Track Trigger for the DØ Experiment in Run II - Technical Design Report." Technical Report, Fermilab, (1998).

[46] G. Borrisov, "Ordering a Chaos or ...Technical Details of AA Tracking." http://www-d0.fnal.gov/atwork/adm/d0_private/2003-02-28/adm_talk.ps

[47] A. Schwartzman and M. Narain, "Primary Vertex Selection," DØ Note 3906 (2001).

[48] A. Garcia-Bellido *et al.*, "Primary Vertex certification in p14," DØ Note 4320 (2004).

[49] A. Schwartzman and M. Narain, "Probabilistic Primary Vertex Reconstruction," DØ Note 4025 (2004).

[50] O.Peters, "Muon Segment Reconstruction: A linked List Algorithm," DØ Note 3901 (2001).

[51] C. Luo, "Muon Reconstruction and B Physics Studies at the Tevatron Collider Experiment DØ," Ph.D. Thesis, Indiana University (2003).

[52] L. Chevalier *et al.*, Track Parameter Error Matrix Propagation in Matter and Magnetic Fields, Error Matrices Combination, (2001). available at http:///www-d0.fnal.gov/ tuchming/myprop.ps

[53] The DØ Collaboration, "Beam Tests of the DØ Uranium Liquid Argon End Cap Calorimeters," Nucl. Instr. and Methods, A324, 53 (1993).

[54] E. Varnes, "Measurement of the Top Quark Mass at DØ Experiment," Ph.D. Thesis, U.C. Berkeley (1997).

[55] J. Kozminski *et al.*, "Electron Likelihood in p14," DØ note 4449, 5 April 2004.

[56] http://www-d0.fnal.gov/d0dist/dist/packages/wz_analyze/devel/doc/Readme.txt.

[57] http://www-d0.fnal.gov/Run2Physics/cs/index.html.

[58] http://www-d0.fnal.gov/phys_id/muon_id/d0_private/certif/p14.

[59] C. Clement *et al.*, DØ Note 4350, "MuonID Certification for p14."

[60] L. Chevalier *et al.*, "Track Parameter Error Matrix Propagation in Matter and Magnetic Field, Error Matrices Combination."

[61] F. Deliot *et al.*, DØ Note 4749,
"Measurement of $\sigma(p\bar{p} \rightarrow\ WX)\ \times\ Br(W \rightarrow \mu\nu)$ at $\sqrt{s} = 1.96$ TeV."

[62] G. Borrisov provided the file of beam spot position.

[63] Emily Nurse and Paul Telford, DØ Note 4573, "Measurement of the Cross Section for Inclusive Z Production in the Di-muon Final States at $\sqrt{s} = 1.96$ TeV."

[64] http://www-d0.fnal.gov/Run2Physics/d0_private/eb/Run2EB_021/Analysis03/note_v03.pdf.

[65] J. Conway, CDF-5894, "Efficiency Uncertainties: A Bayesian Prescription."

[66] T. Sjöstrand *et al.*, Comp. Phys. Commun. 135, p238(2001), "Pythia v6.2 Physics Manual."

[67] J. Pumplin, D. R. Stump, J. Huston, H. L. Lai, P. Nadolsky and W. K. Tung, JHEP **0207**, 012 (2002).

[68] P Telford*et al*, DØ Note 4297, "Retuning of pmcs_chprt to P13 and P14 data."

[69] D. Chapin *et al*, DØ Note 4403, "Measurement of $Z \rightarrow ee$ and $W \rightarrow e\nu$ Production Cross sections with $|\eta| < 2.3$."

[70] S. Frixione and B. R. Webber, JHEP **0206**, 029 (2002);
JHEP **0308**, 007 (2003).

BIOGRAPHICAL SKETCH

SINJINI SENGUPTA

Education

- Ph.D., Physics, Florida State University (May 2006).
- M.S., Physics, Florida State University (2001).
- M.Sc., Physics, Jadavpur University, India (1997).
- B.Sc., Physics (honors), Jadavpur University, India (1995).

Professional Experience

Research

- Ph.D. thesis: Measurement of the W boson charge asymmetry in the muon channel. This is the first competitive measurement of the W charge asymmetry from DØ and the first in the muon channel from the Tevatron in Run II. The analysis involves the extraction of the event sample after testing and implementing various selection cuts, estimating efficiencies and the charge mis-identification rate, checking for all possible sources of bias in the sample, calculating various backgrounds using data and Monte Carlo, and evaluating systematic uncertainties for the measurement.

- Developed and implemented the Silicon Track Trigger (STT) Examine for the DØ detector and maintained it for most of 2004. The Examine is a real-time, online monitoring tool used in the DØ control room and was especially useful during commissioning of the STT in diagnosing problems with the hardware and the electronics. The STT is a Level 2 trigger used for triggering on displaced vertices.

- Acted as one of the on-call STT experts. Participated in the commissioning of the STT in order to integrate it with the rest of the DØ detector and to ensure smooth running. Participated in the testing and debugging of the firmware for the STT.

- Participated, in Summer 2000, in the quality control and testing of silicon chips and sensors to be used in the 'F' disks of the Silicon Microstrip Tracker (SMT) for the DØ detector. Included burn-in of F wedge chips with stand alone sequencers and testing for noise levels in the silicon strips. The SMT was completed in November 2000.

- Performed tests on the power supplies of Analog Front End (AFE) Boards in August 2001. The AFE boards are used for converting analog to digital signals in the Central Fiber Tracker.

- Masters thesis from Jadavpur University, conducted at the Variable Energy Cyclotron Center (VECC) in Calcutta, India(1996–97): "Detecting cosmic ray muons using a scintillator detector". Built a detector using PMMA scintillator pads and photomultiplier tubes and set up the readout electronics to observe muons from cosmic rays.

- Studied "Thin film deposition using RF sputtering techniques" in 1997–98 at the Nuclear Science Center, New Delhi, India.

Teaching/Work

- Teaching Assistant: Taught undergraduate laboratory in Astronomy for two semesters at Florida State University, 1999–2000.

- Worked at the Department of Physics, Indian Institute of Technology (IIT), New Delhi, India, in 1999 developing a C++ based framework for physics analysis.

Talks

- "Measurement of the W charge asymmetry in the muon channel," APS April Meeting, Tampa, FL, 2005.
- "A precision measurement of the W charge asymmetry using the DØ detector," HEP Seminar, U.Minnesota at Minneapolis, Feb. 2006.

Awards

- FSU University Fellowship, 2001–2002.
- FSU College Teaching Fellowship, 1999–2000.
- Ranked first in the state of Bihar at the 1991-1992 Indian National Mathematical Olympiad (a talent search exam in Mathematics).

Publications

Primary Authorship

1. "The DØ Run II Impact Parameter Trigger," T. Adams *et al.* , to be submitted to Nucl. Instr. and Methods.

Internal notes and documents

1. DØ note 5061, S. Sengupta, "A measurement of the $W \to \mu\nu$ Charge Asymmetry with the DØ detector at $\sqrt{s} = 1.96$ TeV." This is a conference note.
2. DØ note 4855, S. Sengupta, "The W Boson Production Charge Asymmetry in the Muon Channel at $\sqrt{s} = 1.96$ TeV." This analysis is conference approved and on the track towards publication.
3. DØ note 4992, S. Sengupta *et al.* , "STT Examine." The note contains a list and description of the histograms in this Examine.

Computer Skills

- Programming Languages: C++, ROOT, Fortran, BASIC.
- Word Processing: LaTeX, Microsoft Word, EMACS, PICO.
- Platforms: Linux, Unix, Windows.

Outreach and Other Activities

- Elected to the Fermilab graduate student association (GSA) for 2004–2005. Activities undertaken while in this office include
  - trip to Washington DC to meet with members of the House and Senate, stressing the importance of and asking for continued support and funding for the basic sciences and HEP in particular;
  - organizing the 2005 New Perspectives conference aimed at graduate students and young post-docs;
  - organizing socials and a triathlon aimed at graduate students.
- led several guided tours of the accelerator complex and the DØ detector.
- volunteered to help measure the tilt of the magnets in the Tevatron tunnel during the Summer 2004 shutdown.

Language Skills

- Fluent in English, Hindi and Bengali.
- Beginner in German.